Investigation of fungal growth and its influence on the permeability of the oceanic crust

Method Development using *Penicillium Rubens*

Master's thesis in the M.Sc. program Earth Sciences

University of Bergen
Department of Earth Science
Centre for Deep Sea Research

Submitted by
Jule Melina Sophie Krohn
Student ID: 315665

Supervisor: Steffen Leth Jørgensen
Co-Supervisor: Magnus Ivarsson

Bergen, June 2024

Investigation of fungal growth and its influence on the permeability of the oceanic crust

Method Development using *Penicillium Rubens*

Abstract

The deep biosphere within the oceanic crust is a tantalizing frontier of the geomicrobiology field with many unanswered questions owing to great challenges that need to be overcome when investigating this habitat.

Fungi have been proven to be part of this intricate ecosystem on multiple occasions. And even though fungal communities make up the majority of the found body fossils in the deep biosphere, there is still a lack of studies investigating fungi in this habitat. With their many abilities the fungi exert great influence on their environment in various ways, not least of which is that they may also have a significant influence on the alteration and the permeability of the crust.

Using a strain of *Penicillium rubens* a novel experimental method using a custom-build Parr flow-through autoclave was developed to investigate the potential influence of the growth of fungi on the permeability of the crust. The results of the experiments indicate a strong influence of microbial growth on the reduction of the permeability. A potential inversed trend between the extent of permeability reduction and pressure was noted. However, in some experiments contamination with bacteria was observed, which could also account for the more pronounced decrease.

To establish the parameters for the permeability experiments, syringe pump experiments were conducted to assess the growth within a certain timeframe and under certain conditions. To estimate the growth and evaluate the connection between biomass quantity and permeability decrease, two methods for biomass estimations were explored: Loss on ignition and PLS regression models based on the autofluorescence of ergosterol. Both estimation methods have proven to be inadequate to estimate the biomass amount for these experiments. A likely reason for this is that these methods are not robust enough for the low amounts of biomass obtained in these experiments.

Acknowledgements

First and foremost, I want to express my gratitude to my supervisor, Steffen Leth Jørgensen (University of Bergen), for the guidance and motivation over the last 2 years. The constant nudges into the right direction helped me complete this thesis and surpass myself.

I also want to thank my co-supervisor Magnus Ivarsson (Swedish Museum of National History) for his insight into the fascinating world of fungi and the quick replies to my mails.

Throughout the past years my path crossed with many kind people without whom the completion of this thesis would have been much more challenging. I am especially thankful for Hanna Rose Babel (University of Bergen), who dedicated many hours to get me started in the lab and was always there when I needed support.

I want to thank Ingvild Aarrestad (University of Bergen) and Andreas Beinlich (Freie Universität Berlin) for their helping hands in taming the flow-through autoclave. Andreas Beinlich also provided guidance in the processing and analysis of the permeability data.

Special thanks go to Anita-Elin Fedøy (University of Bergen) and Hasan Arsin (University of Bergen) for their help with the fluorescence measurements.

I also want to acknowledge Bjarte Hannisdal (University of Bergen) for his feedback on the statistical part of this thesis.

I would also like to recognize Mauro Passarella (University of Bergen), Roald Langøen (University of Bergen), Sven Le Moine-Bauer (University of Bergen) Yuval Ronen (University of Bergen), Irene Heggstad (University of Bergen) and Lubna Sami Jawad Al-Saadi (University of Bergen) for their support and assistance throughout the course of my thesis in one or the other way.

Thank you all so much for your support and your kind words.

Last but not least I need to thank my boyfriend who has proven to have the patience of an angel, especially over the last two months.

Table of Contents

List of Figures

List of Tables

List of Abbreviations

Abbreviation	Meaning	Page of first use
ODP	Ocean Drilling Program	1
LOI	Loss on ignition	3
DI	Deionized	17
LB	Lennox broth	20
ASW	Artificial seawater	20
PG	Potato glucose	22
SEM	Scanning electron microscopy	25
EEM	Excitation emission matrix	27
PLS	Partial least squares	27
PCA	Principal component analysis	30
ExEmPair	Excitation-Emission Wavelength Pair	30
RMSECV	Root mean square error of cross validation	31
RMSEP	Root mean square error of prediction	31
R^2CV	Coefficient of determination for the calibration set	31
R^2P	Coefficient of determination for the validation set	31
RPDCV	The ratio of prediction deviation of the calibration set	31
RPDP	The ratio of prediction deviation of the validation set	31
VIP	Variable importance in projection	31
PC	Principle Component	38

1 Introduction

The biosphere hosted deep within the dark, oligotrophic marine crust is a tantalizing frontier of the field of geomicrobiology. The crustal ecosystem is part of the so-called 'deep biosphere' and is notoriously difficult to sample and as a result little is known about it. The term encompasses numerous different environments within the continental and the oceanic setting beneath the bioturbated zone or the rhizosphere (IVARSSON et al., 2020b), of which the most important ones are shown in Figure 1.1. While they all share a number of similar characteristics this thesis focuses on the oceanic deep biosphere habitats, especially on the oceanic crust.

The oceanic crust is suggested to be the largest aquifer on Earth with an estimated rock volume of 2.3×10^{18} m^3 and a fluid volume of about 2 % of the total ocean (ORCUTT et al., 2011b). Thus, it is a very spacious environment that is not only highly stable but also exceedingly heterogeneous and characterized by diverse chemical and physical gradients (IVARSSON et al., 2018). Taken its vastness and that life can persist within its pores, cracks and crevices throughout the entire lifespan of the igneous oceanic crust of up to a few hundred million years (CRAMERI et al., 2019), it is hypothesized that this aquifer hosts an immense amount of biomass and as a result complex and versatile water-rock-microbe interactions. Hence, the deep biosphere has the potential to play a crucial role in global biogeochemical cycles throughout Earth's history (IVARSSON et al., 2020b). However, the feedback mechanisms, chemical exchange and linkages between the deep crust and the surface are yet poorly understood (SCHRENK et al., 2010). This is partly due to the novelty of this field of research.

With the expedition of the HMS *Challenger* (1872 – 1876) the scientific investigation of the oceans depth started. However, it took another century until the investigation of the realm below the rock-water boundary picked up.

In sediment samples from the Deep Sea Drilling Project sulphate reduction as well as carbon dioxide and methane production were observed and evidenced an active microbial community up to a depth of 167 m below sea floor (WHELAN et al., 1986). Further investigations of the subterranean microbiology were conducted in connection to energy development and nuclear waste repositories (PEDERSEN, 1993).

The first in-situ observations of endolithic microorganisms were during a scanning electron microscopy study of Icelandic glass, in which the involvement of microbes in the weathering process was observed (THORSETH et al., 1992). A few years later similar structures were found within the glass rims of pillow lavas from 237 m below sea floor from Ocean Drilling Project (ODP) leg 148 at ODP Hole 896A at the Costa Rica Rift (THORSETH et al., 1995). DNA specific stains as well as in-situ fluorescence hybridization of the 16S-rRNA of bacteria and archaea (TORSVIK et al., 1998) were used to confirm the presence of DNA within these samples.

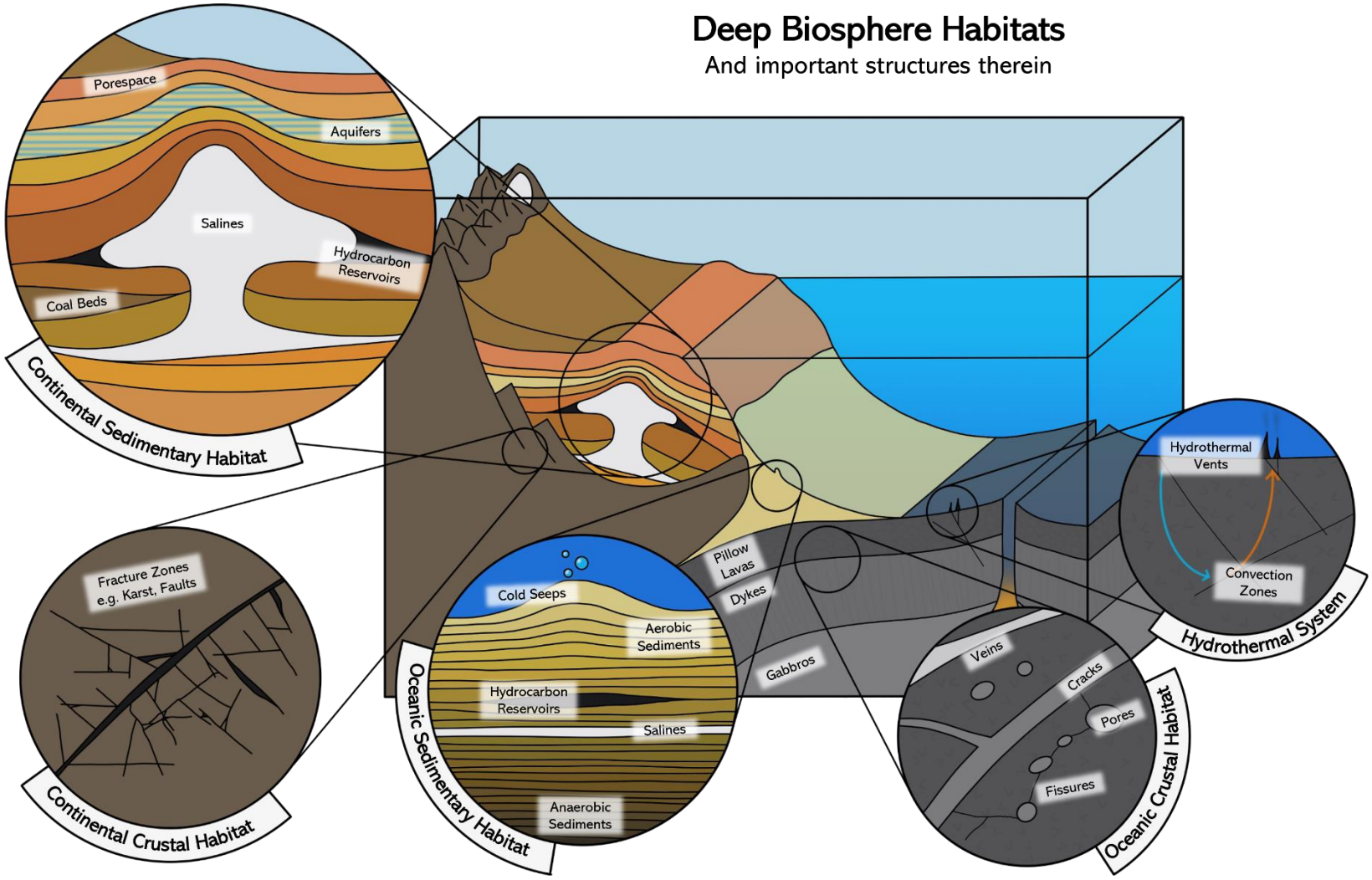

Figure 1.1: Deep biosphere habitats. The important structures highlighted within the habitats are examples of environments in which deep roaming organisms can be found.

The first successful amplification and sequencing of 16S-rRNA genes from subsurface samples were conducted on basalt wash cores from the Australian Antarctic Discordance taken during the ODP leg 187 (LYSNES et al., 2004). This study found that the *Gammaproteobacteria* was the dominating phylogenetic group.

In the same year SCHUMANN et al. (2004) reported for the first time the observation of filamentous fossil structures that were interpreted as fungal remains. The fossils were found in carbonate-filled vesicles within basalts from of ODP Leg 200 site 1224. In fact, based on various morphological traits such as repetitive septa, anastomosis and a central strand, the bulk of fossilized microorganisms found in the deep biosphere are interpreted as remains of fungal communities (e. g. BENGTSON et al. 2014, DRAKE et al., 2021, IVARSSON et al., 2012, IVARSSON et al., 2015b). This makes the igneous crust potentially the largest fungal habitat on Earth (IVARSSON et al., 2016a). And yet, the majority of studies, which are still limited in numbers, focus on the prokaryotic community, leaving the eucaryotes that roam the deep igneous crust underexplored (IVARSSON et al., 2018).

Fungi are present in almost all habitats found on Earth and in most cases exert a big influence on their environment. This is due to their many abilities that also allow them to withstand extreme stressors like temperature, pressure, solar radiation, limited water availability, as well as oligotrophy, as it is the case in the crust. This raises the question of whether the fungi and their interactions with their environment causes them to have an influence on the permeability of the rock and in particular of the igneous crust, i. e. under elevated pressure. This could have profound consequences for the deep community as well as the chemical exchange between the crust and the surface. In this regard it is also important to understand how much biomass the fungi can develop under different circumstances and to what extend the amount of biomass has an influence on the permeability.

To answer these questions and to pave the way to gain a better understanding of the circulation of microorganisms and chemical species and their exchange with the surface, a novel method was developed and tested to expose the fungi to conditions simulating the igneous, oceanic crust and measure the change of permeability that their growth causes. A custom-build Parr flow-through autoclave was used, which is designed for petrological and geochemical investigations of rocks and minerals under high pressures and high temperatures. The flow-through autoclave measures the pressures in front and behind the reaction chamber every minute, allowing the calculation of the permeability and to follow its development over time. In this instrument the fungi were grown for two to three weeks within basalt grains under low and elevated pressures and at room temperature.

Additionally, to evaluate the connection between biomass amount and permeability change, two methods of fungal biomass estimation were tested. One of which is the well-established loss on ignition (LOI) method, which works by burning the samples and calculating the difference in weight before and after combustion. The other is the recently suggested method by MANSOLDO et al. (2020) that uses the autofluorescence of the fungi-typical membrane component ergosterol to calculate the fungal biomass.

2 Status of Knowledge

2.1 The deep subseafloor environment

In 1992, Thomas Gold first coined the term ‘deep biosphere’ in a paper in which he speculates about the widespread existence of microbes within the crust (GOLD, 1992). Since then, the knowledge about the deep biosphere has grown and various definitions have been proposed. Yet, the concept remains diffuse.

The oceanic deep biosphere habitat was initially defined as marine sediments below 10 cm (WHITMAN et al., 1998). However, this definition does not account for bare rocks exposed to the seawater. TESKE & SØRENSEN (2008) defined the upper boundary of the deep subsurface biosphere as the transition zone within the subsurface from water column typical microbial communities to sediment typical communities. This acknowledges the local variability of the onset of the deep biosphere. Another common description of the upper boundary of the deep biosphere in marine settings is beneath the bioturbated zone (IVARSSON et al., 2020b). This is the definition applied in this study.

This definition of the deep biosphere in the marine context comprises pores, cracks, fissures and the pore water of sediments, sedimentary rocks, igneous rocks, sea mounts and hydrothermal vents. However, it should be noted that the deep biosphere is not limited to oceanic environments. In continental settings, the deep biosphere commences underneath the rhizosphere (IVARSSON et al., 2020b) and encompasses the terrestrial bedrock, sediments and sedimentary rocks (see Figure 1.1).

The limits of life are set by different physical and chemical parameters like temperature, pressure, nutrient availability, pore space and liquid water. As long as these criteria are met, life can persist even in environments considered ‘extreme’ like the oligotrophic igneous crust, which is characterized by high hydrostatic pressures (1 bar/10 m), low temperatures (2-4°C) or very high temperatures (>400°C), absence of light and little space (VARGAS-GASTÉLUM & RIQUELME, 2020 and references therein). The conditions can change greatly over small distances, whereas the temporal variations are small (REITNER et al., 2006, IVARSSON et al., 2016c).

2.1.1 The igneous crust

The origin of the igneous crust is at the mid-ocean ridges with the emplacement of the rocks (SCHRENK et al., 2010). There the crust lies exposed on the sea floor, in some cases for hundreds of kilometres before eventually being overlain by marine sediments.

Generally, the crust can be described as built up by three layers (SCHRENK et al., 2010, IVARSSON et al., 2016b). The bottom layer is made up of gabbros. Massive, crystalline igneous rocks that are a result of the slow cooling of vast magma reservoirs. The gabbros are overlain by a dyke

complex, where the magma transport to the surface of the seafloor created crystallized conduits that reach down to about 1.5 km.

The uppermost layer is approximately 500 m thick and mainly consists of basalts in the form of pillow lavas. The interconnected pores and vesicles by microfractures, originating from tension release and quick cooling as well as pressure release and the subsequent degassing of the magma, characterise this layer and allow the seawater to circulate through it (IVARSSON et al., 2016b, IVARSSON et al., 2018). The intensity and duration of the circulation of the fluids is mainly controlled by an enigmatic property called permeability (FISHER, 1998). Permeability describes the intrinsic ability and efficiency of a porous material to allow fluid to flow through this material under standard conditions. Permeability is controlled by the cross-sectional area, the length of the investigated section, the pressure gradient, the fluid viscosity and the flow rate are. The most common unit is m^2, which relates to the area per cross-section that faces the flow direction, through which the fluid can traverse.

FISHER (1998) compiled various studies on the permeability of the oceanic crust in which many different methods were used, both in-situ measurements as well as experiments in the laboratory. He came to the conclusion that the permeability of the crust is heterogeneous and anisotropic, both varying with depth and lithology. A permeability range of 10^{-18} – 10^{-13} m^2 has been found by in-situ borehole measurements and the highest permeabilities are within the upper few hundred metres of the crust. Additionally, it has been found that the permeability decreases with the age of the crust (FISHER & BECKER, 2000, BECKER & DAVIS, 2003). This change in permeability is argued to be induced by mechanical stress changes, sedimentation, filtration, diagenesis, swelling or shrinking, biomass growth or decay and mineral precipitation or dissolution (HOMMEL et al., 2018). These mechanisms can lead to an increase of the permeability but also to a decrease of it and with it to a thwart and eventual extinction of the fluid flow (IVARSSON et al., 2020b), which has an important effect on the transport of solutes and heat as well as the distribution of microbial communities (FISHER, 1998).

In summary, the permeability of the oceanic crust is of great importance as it dictates the degree to which fluids can interact with the host rock. It is essential for the flow paths and residence times of the fluids and consequentially, the permeability ultimately determines the flux of geochemical species as well as microbes through the crust and chemically connects deeper environments to more shallow ones. With that, it is also the controlling factor of the chemical and microbial exchange between the deep biosphere and the ocean, playing a substantial role in global geochemical cycles.

2.1.2 The circulating fluids

The fluids that transport the solutes and microbes, enter the crust where the igneous rocks are exposed to the ocean with no cover of sediments, i. e. mid-ocean ridges, subduction zones and seamounts

(IVARSSON et al., 2016b), as shown in Figure 2.1. They enter the rocks oxygenated and equilibrated with atmospheric CO_2 (TEMPLETON & CARO, 2023). During the circulation of the water through the rocks it becomes increasingly more reducing as well as warmer, depending on various factors like the lithology of the surrounding rocks as well as the geothermal gradient. The geothermal gradient is typically between 30 °C and 50 °C per km in the oceanic basement, which sets the limit for life at a depth of ca. 2-4 km below the seafloor (JØRGENSEN & BOETIUS, 2007). Other important factors for the chemical changes of the fluids are the residence times and the extent of the water-rock interactions (TEMPLETON & CARO, 2023).

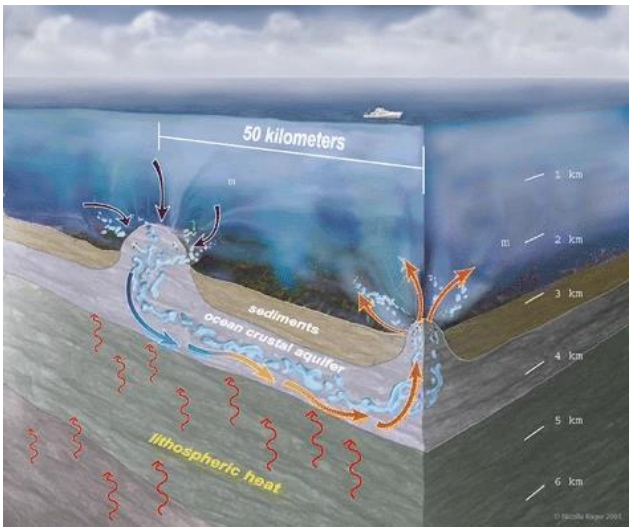

Figure 2.1: Fluid circulation within the oceanic crust. The figure shows fluid recharge at a seamount, its flow and its concurrent heating within the crust and its discharge at another seamount. Original artwork by Nicolle Rager and modified by FISHER (2005).

One example of these water-rock interactions is a process called serpentinization in which the Fe(II) within minerals like olivine or pyroxene oxidizes upon reaction with the water, forming minerals like e. g. magnetite containing Fe(III). During this process H_2 is released, one of the most universal energy sources for life (TEMPLETON & CARO, 2023, IVARSSON et al., 2016c). This and other fluid-rock interaction can alter the conditions in the environment by changing the pH of the fluid as well as mobilizing important nutrients and energy sources like CO_2, sulphate and phosphate (TEMPLETON & CARO, 2023).

COWEN et al. (2003) conducted an investigation of fluids sampled from 3.5-million-year-old crust of the Juan de Fuca ridge in the northeast Pacific Ocean. They found that the fluids were enriched in NH^{4+}, Si, Ca^{2+} and Sr^{2+} while being depleted in SO_4^{2-}, K^+, and Mg^{2+}, which they interpreted to be results from fluid-rock interactions. MEYER et al. (2016) on the other hand, found that the crustal fluids are very similar to the local bottom seawater with only minor differences of certain elements. The occurrence of oxygen in the igneous crust is very heterogeneous and studies found a correlation between oxygenation of the fluid and the mineralogy of the surrounding rocks (IVARSSON et al., 2016c).

Furthermore, the seepage of the seawater into the crust also transports organic matter like complex hydrocarbons into the crust (IVARSSON et al., 2016b). Additional organic molecules are produced abiotically by Fischer-Tropsch-type reactions from H_2 and CO/CO_2. The result of such reactions are simple hydrocarbons like CH_4 as well as more complex ones like fatty acids. Such molecules are needed to sustain a deep biosphere.

2.1.3 The deep biosphere

Certainly, the igneous crust environment contains everything necessary for a lithoautotrophic ecosystem, i. e. hosting a community based on primary productivity fuelled by redox reactions with inorganic compounds (TEMPLETON & CARO, 2023). Examples of inorganic compounds available within the crustal habitat include Fe(II) as an electron donor within minerals like olivine, pyroxene and biotite and Fe(III) as electron acceptor within diverse iron oxides like magnetite or hematite.

These lithoautotrophic communities are thought to be the base of the subseafloor biosphere (IVARSSON et al., 2016b, IVARSSON et al., 2018). And even though bacteria dominate in abundance, the other two domains of life can be found in the oceanic crust as well (ORSI et al., 2013). The presence of microorganisms in the crust has important implications to the ongoing chemical cycles and elemental exchange between the bio-, geo- and hydrosphere because the biotic alteration of rocks is different to abiotic alterations with different geochemical fluxes involved (STAUDIGEL et al., 2008). These interactions between the different spheres were even suggested to have been a major driving force of the oxidation of the reduced oceanic crust which ultimately led to the establishment of micro-continents (GROSCH & HAZEN, 2015). And until the Devonian, with the onset of plants growing in terrestrial habitats, the deep subsurface biosphere might have hosted the majority of the Earths biomass (MCMAHON & PARNELL, 2018).

The investigation of the subsurface deep biosphere faces several challenges: First, this habitat is hard to reach and it is difficult to ensure no contamination while sampling. But another problem is the very slow in-situ growth of the organisms, which makes it difficult to cultivate them (JØRGENSEN & BOETIUS, 2007). While a study about the turnover rates within the oceanic crust has yet to be conducted, the turnover rates in the subsurface sediments from different sampling sites were determined to be a year and up to a few decades (BRAUN et al., 2017).

MEYER et al. (2016) as well as TULLY et al. (2018) investigated the microbial community of fluids extracted from the crust from the North Pond. The North Pond is an isolated sediment basin at ca. 4484 m water depth west of the Mid-Atlantic ridge on 7-8 million years old crust (TULLY et al., 2018). They found that the community structures are distinct from the ones of the respective bottom seawater (MEYER et al., 2016, TULLY et al., 2018). Additionally, the microbial community within the crust has temporal and local variation (TULLY et al., 2018).

The microorganisms native to the crust are either passively transported by circulating fluids or actively migrate through the fractures where the pore space and the fluid flow permits (IVARSSON et al., 2016a, IVARSSON et al., 2018, IVARSSON et al., 2020b). This likely leads to the enrichment of the microbial communities at localities where the permeability of the rock is high (ORCUTT et al., 2011a) and a difference of up to 10 orders of magnitude in cell counts (TEMPLETON & CARO, 2023).

TULLY et al. (2018) found a range of 5 - 20 x 10^3 cells/ml, whereas MEYER et al. (2016) counted a cell density of almost a magnitude higher with 1.4 - 2.2 x 10^4 cells/ml. JØRGENSEN & ZHAO (2016)

estimated the cell densities within samples of pulverized basaltic rocks from bore holes from North Pond based on the copy numbers of the 16S rRNA gene of bacteria and archaea to be in the range of 0.1 - 2 x 10^4 cells/g of sample material. SANTELLI et al. (2008) investigated basaltic sea floor lavas from the East Pacific Rise and using quantitative polymerase chain reaction they got cell counts between 3 x 10^6 - 1 x 10^9 cells/g rock of the glassy rinds of the lava flows.

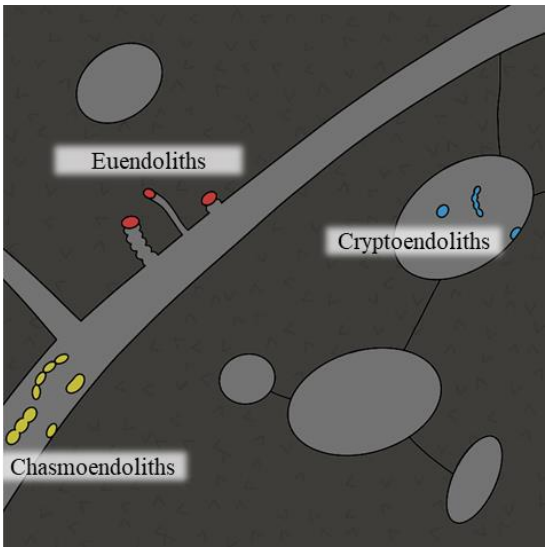

Figure 2.2: The subdivision of endoliths depending on their habitat. Chasmoendoliths roam in existing cracks, euendoliths create cavities and cryptoendliths reside in existing cavities within the rock.

All four studies (SANTELLI et al., 2008, MEYER et al., 2016, JØRGENSEN & ZHAO, 2016, TULLY et al., 2018) as well as LYSNES et al. (2004) found that the *Proteobacteria* were dominating in the crustal samples with either *Gammaproteobacteria* or *Alphaproteobacteria* being the dominating class.

Endoliths, organisms that inhabit rocks, are classified into three categories depending on their specific locations within the rock, as illustrated in Figure 2.2. Chasmoendoliths invade fissures and cracks that already existed, cryptoendoliths roam in structural cavities of the rock and euendoliths actively penetrate the rocks, creating cavities themselves (IVARSSON et al., 2016b). These cavities are suggested to be created by the ability of microbes to change the pH of their surroundings with their metabolic products causing pitch marks most commonly found on basaltic glasses (STAUDIGEL et al., 2008). This creates ichnofossils (a record of biological activity without the preserved remains themselves) in the form of etch marks that run perpendicular to the surface and inwards into the glass as well as micron-sized, near spherical voids on the surfaces (IVARSSON et al., 2016b). These forms of glass bioalteration have been documented globally (STAUDIGEL et al., 2008), which potentially makes microorganism an important factor of the global alteration of the crust.

The cells of the microorganisms living inside the crust do not only have the potential to dissolve the minerals around them, but they also act as nucleation sites for secondary minerals, thus immobilizing certain chemical species. The precipitation of these secondary minerals has been argued to eventually clog up the system until the fluid flow is halted (KRUBER et al., 2008, STAUDIGEL et al., 2008, IVARSSON et al., 2020b). Moreover, precipitation leads to the encrustation of the organisms which ultimately leads to fossils that help reconstruct the microbial community within the subseafloor environment. The majority of these body fossils found in the deep biosphere are interpreted as fungal remains and yet the fungi within the contemporary oceanic crust are underexplored.

2.2 Fungi

2.2.1 Taxonomy

Fungi are one of the five kingdoms of life next to plants, animals, protists, bacteria and archaea (RICHARDS et al., 2017), with their closest evolutionary relatives being the animals (GADD et al., 2017). The kingdom comprises 8 phyla, 12 subphyla and 46 classes (SPATAFORA et al., 2017). The Ascomycota and the Basidiomycota are monophyletic and collectively form the subkingdom Dikarya (SPATAFORA et al., 2017). The Ascomycota currently represents the largest fraction of the fungi with 64 % of the described fungal species (BINDSCHEDLER et al., 2016). A simplified phylogenetic tree of the kingdom fungi can be found in Figure 2.3.

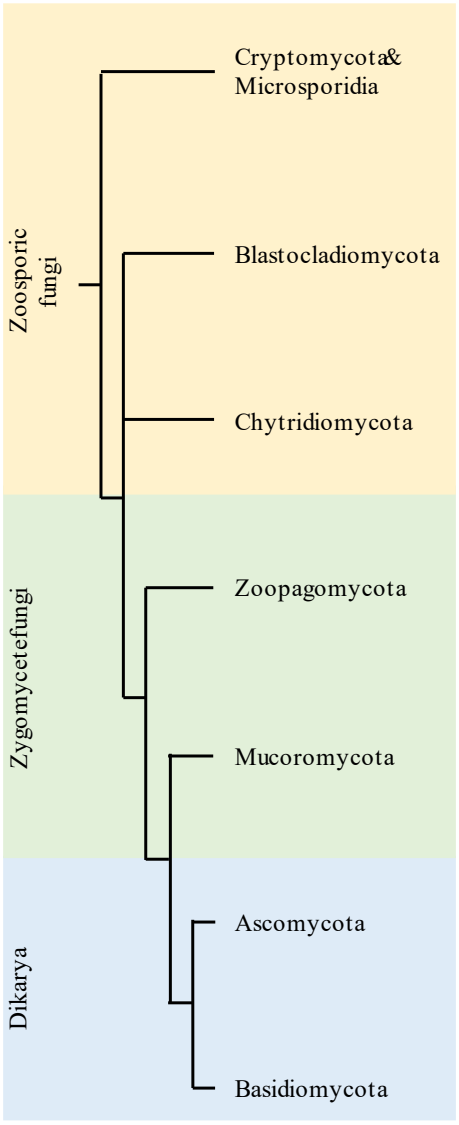

Figure 2.3: Simplified phylogenetic tree of the kingdom fungi. Based on SPATAFORA et al., 2017)

2.2.2 Physiology

Most fungi are multicellular and grow in the shape of filamentous hypha that can grow into complex networks called mycelia (BINDSCHEDLER et al., 2016). Another form of growth of fungi are unicellular yeasts. Some fungi are dimorphic and can change between yeast-like or filamentous growth depending on stresses and stimuli like temperature (RAPPLEYE & GOLDMAN, 2006, BINDSCHEDLER et al., 2016). It has been suggested that dimorphic fungi are also part of the deep biosphere because of the selective advantage that each of the lifestyles provide (DRAKE et al., 2021).

The main function of the hyphae is the uptake of nutrients. Hyphae secrete enzymes across the cell wall to break down complex organic material into simpler molecules that can osmotically be transported into the cell (IVARSSON et al., 2020a). This is promoted by the surface increase provided by the formation of complex, three-dimensional mycelia that doubles the surface area compared to a biofilm. This high surface to mass ration in combination with their osmotrophic feeding mechanism allow them to grow, process metabolites and sense nutrients simultaneously (LANDEWEERT et al., 2001, RICHARDS et al., 2017). Moreover, the hyphae branch at unpredictable intervals, enabling the

fungi to encapsule substrates and gain a competitive advantage by efficiently exploiting nutrients (RICHARDS et al., 2017, IVARSSON et al., 2020a).

This ability of fungi is enhanced further by anastomosis. Anastomosis is the occurrence of fusing of two hyphae. The increase of the interconnectedness of the mycelia by anastomosis enhances the reallocation of nutrients to locations where they are needed, enabling fungi to grow through a nutrient impoverished zone (LINDAHL et al., 1999, RITZ, 2006).

In addition, the apical growth of hyphae at their tips can allow fungi to grow at an extraordinarily high rate under certain circumstances, thus not only accumulating a large biomass but also exploring a habitat rapidly (FEOFILOVA, 2010). This also allows fungi to combine nutrient sensing, nutrient uptake and growth (RICHARDS et al., 2017).

Thus, fungi can thrive on even minimal nutrient levels (GADD, 2017), they not only play a crucial role in nutrient-rich soils but also on barren, hard-rock environments. Fungi have been found to be ubiquitous and even dominating inhabitants on rock outcrops (GADD, 2017) of siliceous types, sandstone, granite, limestone, marble and gypsum (BURFORD et al., 2003), where the fungal community is influenced by the chemical elements of the minerals of the rocks (GLEESON et al., 2005). This flourishing of fungi on bare rock outcrops has led to the speculation that they may have belonged to the first terrestrial pioneering organisms (SPATAFORA et al., 2017).

2.2.3 Subsurface Mycology

The above-described characteristics of the hyphae allow fungi to also assert themselves in the deep biosphere. In fact, the adaptations of the hyphae are so suitable for the existence in the crust, that IVARSSON et al. (2020a) suggested that the evolution of the hyphae took place inside the crust, rather than in terrestrial habitats. It would be conceivable that in multiple occasions fungi could have been introduced to the subseafloor environment and even the oceanic crust, where the development of morphological characteristics favourable for this endolithic lifestyle could have taken place.

This hypothesis is underlined by the discovery of fossils inside the 2.4 Ga old Ongeluk formation in South Africa that were interpreted as fungal-like colonies (BENGTSON et al., 2017). Filaments extending from a basal film attached to rock surfaces exhibit branching and even anastomosis. These colonies were formed long before the colonization of the continents.

2.2.3.1 Subsurface Fungal Community

Over the past two decades fungi have gained more attention as members of the deep biosphere and more investigations have taken place. As an advantageous stress response, the growth of fungi in extreme environments is very slow (GOSTINČAR et al., 2022). This makes it difficult to investigate the fungal community with culturing experiments. Molecular investigations can be biased as well, since some of the primers used to identify fungal DNA tend to amplify Dikarya more than basal fungi, as it was the case in VARGAS-GASTÉLUM et al. (2019). However, a couple of studies have

been conducted successfully with either one or both strategies. While the fungal inventory of the oceanic crust remains yet to be investigated, several studies investigated sediments from the deep sea and provide an overview of fungal species that can be expected to be found in the deep subsurface habitat.

VARGAS-GASTÉLUM et al. (2019) conducted an investigation of deep-sea sediments of the Mexican exclusive economic zone of the Gulf of Mexico. They took samples from 1000 and >3500 m depth and obtained 4421 operational taxonomic units by targeted ITS1 sequencing, confirming that the fungal diversity is high even in the deep subsurface. The majority of the fungi were identified as Ascomycota and the second largest group were unidentified fungi, demonstrating that there is still much to discover. Especially the genera *Penicillium* and *Rhodotorula* were often identified. Whereas DAMARE et al., (2006) found that *Aspergillus* was the most common species in sediments from circa 5000 m depth of the central Indian basin. However, in this study the results are based on isolates instead of molecular analysis. *Penicillium*, *Rhodotorula* as well as *Aspergillus* are very common fungi found in various different habitats (WIRTH & GOLDANI, 2012, PRASONGSUK et al., 2018, CAMPOS et al., 2022).

During investigations of basaltic outcrops (ETIENNE & DUPONT, 2002) as well as sediment samples of diverse marine provinces (including ridge flanks, continental margins and abyssal plains) (ORSI et al., 2013) fungi have been found to follow the old tenet "Everything is everywhere but the environment selects" (BAAS BECKING, 1934), in the sense that the fungal communities are linked to microenvironmental characteristics rather than to climatic zones (ETIENNE & DUPONT, 2002). In marine environments they especially show a significant correlation with total organic matter, nitrate, sulphide and dissolved organic carbon (ORSI et al., 2013).

This is further accentuated by the detection of terrestrial fungi in the deep sea by isolation experiments from sediments of the Central Indian Basin (SINGH et al., 2010), which underlines the resilience of the fungi that are able to survive under such profoundly different conditions like the increased pressure in the deep sea.

In fact, pressure as a challenging or even limiting factor has not satisfactorily been explored yet, however, the cell wall of fungi is very resilient due to a 'skeleton' composed of chitin-glucan complexes that can be found in all fungi except for zygomycetes (FEOFILOVA, 2010). The stability is further increased by compounds like polysaccharides, lipids and pigments embedded in this 'skeleton'. This results in a cell wall that is mechanically stronger than that of e. g. bacteria (SASAKI et al., 2006).

2.2.3.2 Colonization

The colonization of pore space by filamentous fungi begins by the initiation of a biofilm along the pore walls (Figure 2.4 A) from which eventually filaments will protrude perpendicularly into the pore space (Figure 2.4 B) (IVARSSON et al., 2018). The hyphae can develop into a mycelium that

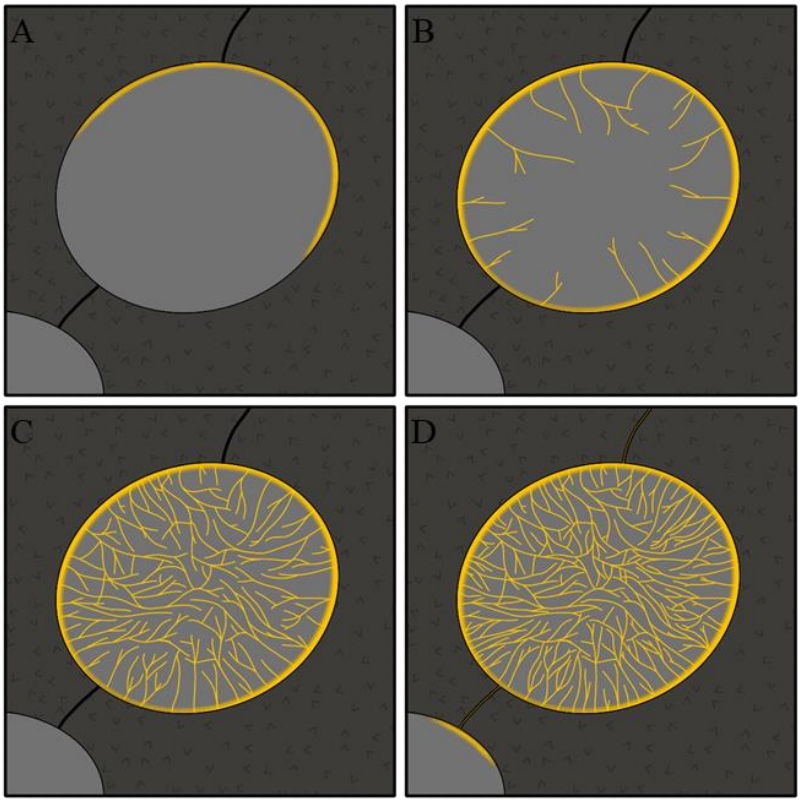

Figure 2.4: Schematic of the colonization of a pore within a basalt by fungi. A: Development of a biofilm. B: First protruding hyphae. C: Formation of a complex, pore space filling mycelium. D: Expansion of the mycelium through microcracks to other pores.

eventually fills out the entire pore space and sporophores can develop, that grow, like the hyphae, perpendicular to the biofilm (Figure 2.4 C). To colonize a vaster region and with that to increase their chances to thrive in this habitat, they follow cracks and fissures connecting the pore spaces (Figure 2.4 D as well as Figure 2.5 A) (SCHMID-BEURMANN et al., 2023). The reconstruction of this colonization process was facilitated by the bulk of fossils of fungi found from the deep biosphere (IVARSSON et al., 2020b, SCHMID-BEURMANN et al., 2023).

2.2.3.3 Fossils

Fungal fossils were found encrusted in clay minerals of various compositions, iron oxides, manganese oxides, calcites and in association with zeolites (PECKMANN et al., 2008, IVARSSON et al., 2012, IVARSSON et al., 2015b, IVARSSON et al., 2020b). And while taxonomical affinity is difficult to assess on fossilized communities, IVARSSON et al. (2012) interpreted the majority of Eocene, filamentous fossils from the Emperor Seamounts, Pacific Ocean, to be Dikarya (compare Figure 2.3) based on morphological traits and the presence of chitin. Moreover, IVARSSON et al. (2015b) identified a fossilized reproduction cycle of Zygomycetes in rocks from the Vesteris Seamount, located in the Greenland Sea, proving their ability to prosper in this endolithic environment and showing that they are an integrated part of the deep biosphere.

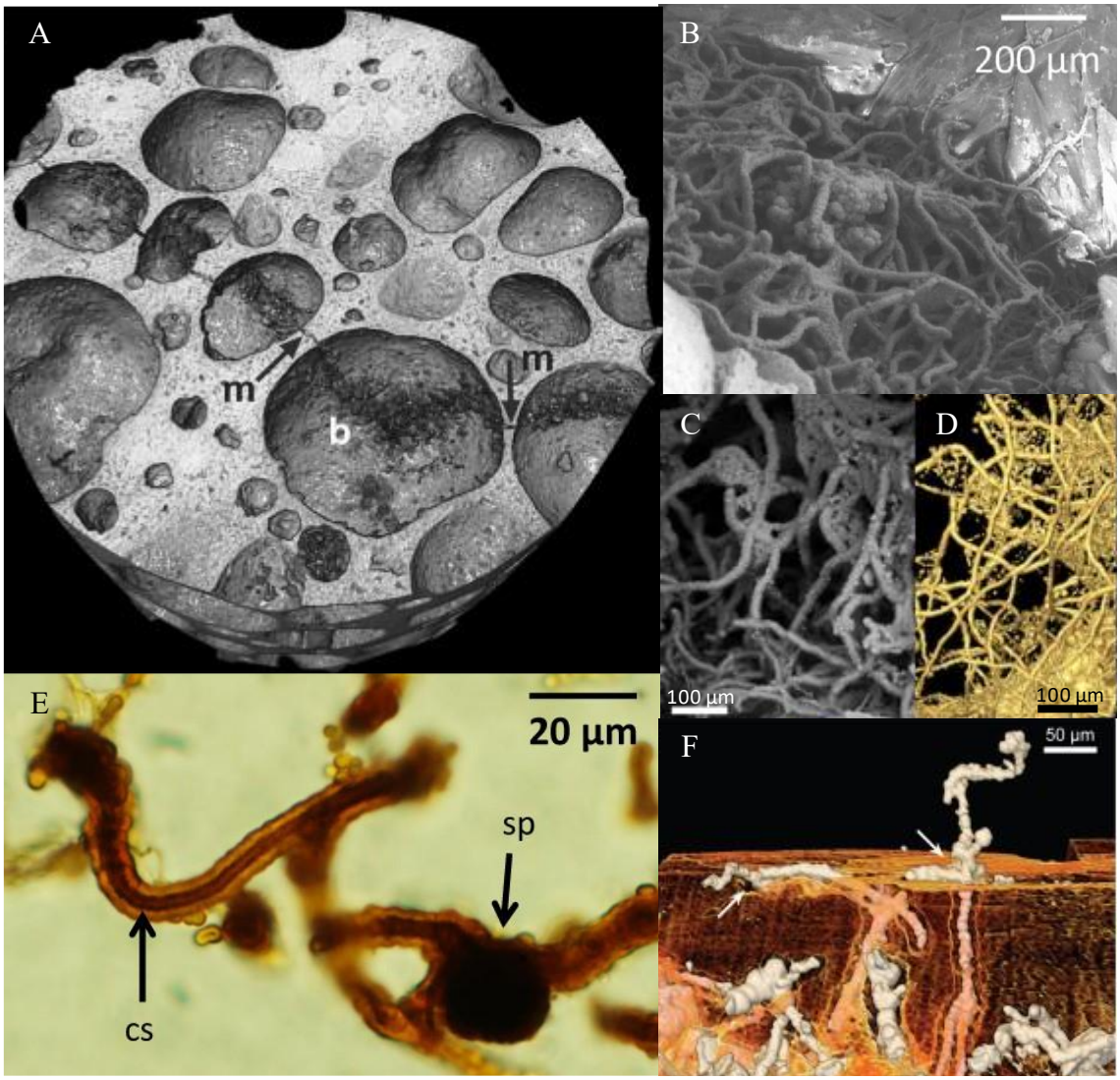

Figure 2.5: Images of fungal fossils of the deep oceanic crustal biosphere. A: A 3D X-ray microscopy volume reconstruction visualizing the growth and distribution of filamentous fungi along microcracks connecting pores of a dredged basalt from Vesteris Seamount, Greenland Sea. b = fungal-microbial bulges, m = microcracks. B: Environmental scanning electron microscope image of a fossilized fungal mycelium within an open pore in a basalt of Koko Seamount, Pacific Ocean. C: Environmental scanning electron microscope image of a fungal-prokaryotic consortium within pores of basalts of the Koko Seamount, Pacific Ocean. D: Synchrotron radiation X-ray tomographic microscopy isosurface rendering showing the same region as in C, highlighting the ferruginous central strand encased in the montmorillonite crust visible in C. E: Microphotograph showing a fungal hypha with a central strand and a spherical spore structure within basalts from the Vesteris Seamount, Greenland Sea. cs = central strand, sp = sporophore/spore F: Tomographic rendering of boring fungal hyphae advancing through a zeolite. Arrow highlights branching of the hypha at the point of exit of the mineral. Samples are from a basalt from the Koko Seamount, Pacific Ocean. Modified after A: SCHMID-BEURMANN et al. (2023), B: IVARSSON et al. (2020b), C & D: BENGTSON et al. (2014), E: IVARSSON et al. (2015b), F: IVARSSON et al. (2015a)

Yellowish filaments were found in dredged rocks from the Vesteris Seamount (Greenland Sea) (IVARSSON et al., 2015b). They were several hundred µm long, 10-20 µm wide and occurred either single or in complicated networks. The filaments were composed of clay minerals that encrusted a central strand made from iron oxides. This is a typical fossilization pattern for fungi with the clay minerals usually of the smectite or montmorillonite type (IVARSSON et al., 2020b). And a central strand has also been found in other fungal fossils, e. g. in fossils from the Emperor Seamount in the Pacific Ocean (IVARSSON et al., 2012). Examples of this fossilization pattern can be seen in Figure 2.5 (see B-E). Further, have IVARSSON et al. (2015b) found that the fungal spore formation is involved in manganese oxidation, which leads to the preservation of the spores as manganese oxides (IVARSSON et al., 2020b).

However, fossils are not only preserved in open pore space, but the organisms can also be preserved in vein-filling minerals like carbonates and zeolites (IVARSSON et al., 2016b). One example of this can be seen in Figure 2.5 F, which shows a fungal hypha protruding through a zeolite. found Another example are filaments consisting of clay minerals that were interpreted to be biogenic in origin. These clay filaments were enclosed in carbonate cement in middle Devonian pillow basalts of the Rhenish Massif in Germany (PECKMANN et al., 2008).

The fossilized fungi have often been observed in association with fossilized prokaryotic communities that suggests a symbiotic relationship (IVARSSON et al., 2015a, BENGTSON et al., 2014). For example, IVARSSON et al. (2015a) suggested that the fungal community close to microstromatolites, scavenged the stromatolite for organic matter and Fe(II). In the basalt of the Emperor Seamount, BENGTSON et al. (2014) found microstromatolites that they interpreted as the iron-oxidizing *Frutexites* as well as cobweb-like structures that grew suspended on the fungal mycelia inside the pore space. A prokaryotic-fungal consortium from the Koko Seamount, Pacific Ocean is shown in Figure 2.5 C and D. BENGTSON et al. (2014) suggested that deep below the seafloor a symbiosis with chemoautotrophic prokaryotes is necessary to establish a thriving eukaryotic colony. While the fungi benefit from the organic matter that the prokaryotes produce, it has been proposed that hydrogen-consuming chemoautotrophs in anoxic environments take advantage of anaerobic fungi as a biological source for H_2 (IVARSSON et al., 2016c, DRAKE et al., 2021).

Considering the published articles as well as the upper examples it stands out that fossilized fungal hyphae and mycelia are found more often than fossilized yeast cells (IVARSSON et al., 2020a). This could either mean that this form of growth provides advantages to the fungi in the subsurface or this could simply be a preservation effect as the yeast cells might not get as easily preserved as the mycelia.

2.2.3.4 Abilities

Next to the body fossils also ichnofossils might get preserved in the form of up to 100 µm long tunnels produced by fungi in basaltic glass (STAUDIGEL et al., 2008). This is possible because of the

ability of the fungi to synthesize organic acids like citric or oxalic acid (ADEYEMI & GADD, 2005, AMIRI et al., 2011). Observations of fungi encrusted in secondary minerals reveal their ability to continue growth until reaching the surface of the mineral, confirming their capacity to dissolve minerals (IVARSSON et al., 2020a). This also has important implications for the nutrient availability in the fluids, since acids have been found to mobilize e. g. PO_4^{3-}, SO_4^{2-}, Ca^{2+}, Fe^{3+}, Mn^{2+}, Si, Al^{3+}, Mg^{2+} (GADD, 1999, EHRLICH, 2006, SUYAMUD et al., 2020, IVARSSON et al., 2020b). This form of dissolution of minerals is not limited to the hyphal tip but rather takes place along the entire hyphal surface (SMITS, 2006). Considering that minerals are a rich source of nutrients (MARTINO & PEROTTO, 2010, IVARSSON et al., 2015a) this is an advantageous skill to possess in the crustal habitat. Their ability to leach rare earth elements was proven to be active and effective even under Mars-like conditions (low oxygen and low gravity) (COCKELL et al., 2020).

The fungal hyphae have been observed to serve as nuclei for mineral growth, for example for zeolites but also for clay minerals, through the exudation of organic acids and extracellular polymeric substances (ETIENNE & DUPONT, 2002, FINLAY et al., 2006, IVARSSON et al., 2015a, BINDSCHEDLER et al., 2016 IVARSSON et al., 2018). With the precipitation of the secondary minerals dissolved elements like Si, Al, Mg, Mn, Na, K and Fe are immobilized (IVARSSON et al., 2020b). FOMINA et al. (2010) conducted an experiment at ambient conditions in which they grew acid-producing fungi on limestone and concluded that the fungi have the potential to precipitate a crust of secondary minerals within the host rock that effectively cements it. If transferable to the deep biosphere, this process could have a considerable influence on the permeability of the crust as well.

All these abilities of fungi named above have been found in the deep biosphere with definitive or circumstantial evidence. However, in environments easier to study than the oceanic crust fungi were found to possess the ability to exert mechanical pressure to penetrate different materials for nutrient gain. When a hypha encounters a solid material it either reacts by changing its growth direction or it develops an appressorium, an adhesion organ (DEISING et al., 2000, MONEY, 2004). Tens of atmospheres of hydrostatic pressure can be exerted with the osmotically generated turgor pressure within the hypha and by cell wall loosening at the growing apex (MONEY, 2004). The fungus *Phallus impudicus* was found to grow through the asphalt of a street, demonstrating the ability of producing a force of about 1.33 kN/m^2, which would mean that just three of these mushrooms would be able to lift roughly 400 kg, equally to a gorilla, a small grand piano or a large bear (NIKSIC et al., 2004).

Breaking-up the material will increase the surface of the attacked objects, which leads to an increase in the chemical reactivity, making it more vulnerable to the organic acids and the enzymes that the fungi release. In laboratory experiments fungi have been found to take advantage of this causality by growing into existing cracks and dissolution pits and mechanically enlarge them (TANG et al., 2013, KIRTZEL et al., 2020).

With all the above-mentioned interactions of fungi with their environment, fungi are assumed to play an important role in the deep biosphere. Yet, little is known about the level of impact the fungi have not only on the local ecosystem but also on a global scale. The chemical exchange between the crust and the ocean above is not yet fully understood but suspected to be eminent.

2.2.4 Effects on Permeability

With the abilities of fungi, they have the potential to influence the permeability and with that the flow path inside the crust as well as the fluid exchange between the crust and the ocean. This could have great implications for global cycles of geochemical species. Yet, little is known about the influence of fungi on the permeability of porous materials. On the one hand, the growth and development of biomass as well as the precipitation of secondary minerals and production of hydrogen gas, the fungi could decrease the permeability and facilitate the clogging of the system, however, with their ability to solubilize minerals and cracking of even hard materials like rocks, the opposite might be true.

So far fungi found little attention in bioclogging experiments. SEKI et al. (2002) have found that the clogging induced by fungi is substantial and even though the clogging by bacteria is more rapid, the clogging by fungi in a mixed fungal and bacterial community is predominant (SEKI et al., 1998). The initial decrease within the first 2 to 12 days is pronounced in bioclogging experiments with bacteria (ZHONG et al., 2013, ZHONG & WU, 2013) but also for mixed and solely fungal communities (SEKI et al., 1998, SEKI et al., 2002). After this initial strong decrease the permeability stabilizes with a common tendency to decrease slightly (SEKI et al., 1998, SEKI et al., 2002, ZHONG et al., 2013, ZHONG & WU, 2013). However, the establishment of preferential flow patterns of the fluid by bioclogging (THULLNER, 2010, ZHONG & WU, 2013) can lead to a reduced or even halted flow and consequently reduced delivery of nutrients and solvents, which can ultimately result in the inhibition of the growth (HOMMEL et al., 2018). Furthermore, flux shear forces are increased which can limit the bioclogging by removing parts of the biomass (THULLNER et al., 2010, DUPIN & MCCARTY, 2000). This suggests that microorganisms with a strong attachment to the surface of the porous material as well as on each other reduce the permeability more efficiently (DUPIN & MCCARTY, 2000).

3 Materials and Methods

3.1 Experimental Design

Two different experiments were conducted in this study to explore several aspects: Firstly, how fungal biomass can be estimated in experimental settings, secondly, if fungal biomass growth can influence the permeability of porous materials, potentially including the crust, and lastly, the relationship between permeability development and biomass production.

3.1.1 Syringe Pump Experiments

Multiple syringe pump experiments were undertaken to test the biomass estimation methods and to develop an idea of how much fungal biomass can develop under certain circumstances in a specific amount of time. The proceeding of the syringe pump experiments is shown in Figure 3.2.

A Chemyx Fusion 200 two-channel syringe pump with a 10-syringe push and pull rack as well as a Chemyx Fusion 200x infusion and withdrawal pump with an 11-syringe push and pull rack were used. Dunites from the Leka Ophiolite Complex (see section 3.2.3.1) were crushed in a disk mill and sieved to attain fractions of big (2-4 mm), medium (1-2 mm) and small (0.85-1 mm) or mixed (1-4 mm) grain sizes.

To prepare the experiments, the dunite grains were added to 7 ml opaque glass vials together with sufficient seawater (see section 3.2.2.2) to fill up the vials. These were closed with a rubber stopper and autoclaved for 20 min at 121 C. After autoclaving, the vials were incubated by piercing the rubber stopper with a needle and transferring a small piece of fungal mycelium (see section 3.2.1) into the middle of the vial. For blank samples this step was skipped.

Syringes attached to the inlet needles were filled with 10 ml of fluid of different compositions (see Table 3.1) and mounted into the syringe pumps. Then, both, the outlet and the inlet needles, were inserted into the vials through the rubber stopper. The outlet needles were submerged into narrow neck reagent bottles filled with deionized (DI) water to ensure a continuous flow of the outlet fluid and prevent clogging by crystallization of salts. The set-up of the syringe pump experiments is shown in Figure 3.1.

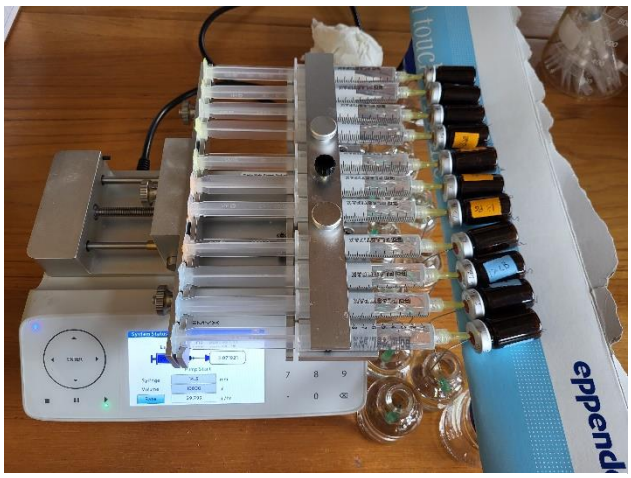

Figure 3.1: Set-up of the syringe pump experiments. In the picture is the Chemyx Fusion 200x with 11 syringes pumping into glass vials with outlet needles leading into narrow neck reagent bottles.

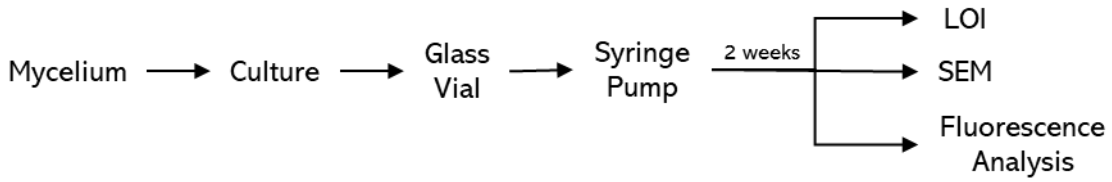

Figure 3.2: Flow chart of the syringe pump experiments. LOI = Loss on ignition, SEM = Scanning Electron Microscopy

Multiple syringe pump experiments have been conducted, for an overview of grain sizes, flow rate, fluid composition and analysis methods see Table 3.1. After the first syringe pump experiment it was determined that there was a lot of dust within the samples, that is why the crushed dunites were subsequently first washed with tab water and then rinsed with DI water after sieving. Additionally, the grains for syringe pump experiment 2 were burned at 550 °C for 1 h to burn off any potential organic carbon on the grains.

The reason for the two durations of syringe pump experiment 2 is that one of the two syringe pumps stopped before it was manually stopped. The pump that stopped contained the entirety of the samples with the big grain size, as well as all blank samples of the medium grain size. The same happened to the syringe pump of experiment 4.

Table 3.1: Executed syringe pump experiments. (Abbreviations: I = Inoculated with *Penicillium rubens*, B = Blank, MC = Medium of the culture used for inoculation, 10 % PG = 10 % potato glucose in seawater, 50 % PG = 50 % potato glucose in seawater, 1 % PG = 1 % potato glucose in seawater, 1 % LB = 1 % Lennox broth in seawater, LOI = loss on ignition, FM = fluorescence measurements, SEM = scanning electron microscopy)

No.	**Quantity**		**MC**	**Flow rate**	**Duration**		**Grain size**	**Fluid composition**	**Analysis method**
	I	**B**		**(µl/h)**	**(h)**	**(d)**	**(mm)**		
1	3 3 3	2 - -	1 % PG	29.799	331.56	13.83	1-4	10 % PG 1% PG 1 % LB	LOI
2	4 4 4	3 3 3	50 % PG	29.799	331.24 331.24/ 318.54 318.54	13.8 13.8/ 13.29 13.29	0.85-1 1-2 2-4	1 % LB 1 % LB 1 % LB	LOI
3	6	4	100 % LB	29.799	333.57	13.9	2-4	10 % LB	FM
4	7	4	100 % LB	29.899	316.32	13.19	1-2	10 % LB	FM/SEM

3.1.2 Permeability Experiments

The permeability experiments were done to investigate the influence of fungal biomass growth on the permeability of porous materials over time. The process of these experiments is shown in Figure 3.4.

These experiments were conducted in a custom-build Parr flow-through autoclave in a stainless-steel reaction chamber. The pump used in the system is a VP-6K dual-piston high-pressure metering pump from Vindum. Pressure is measured and recorded every minute in front and behind the reaction chamber with Ashcroft G2 Pressure Transducers. The pressure within the system is regulated with a TESCOM 26-1762-24-360 backpressure regulator behind the outlet pressure transducer. In this study the outlet fluid was connected to the fluid reservoir so that the fluid circulates through the system during the experiment. New fluids were used for every experiment. The schematic of the set-up of the experiment is shown in Figure 3.3.

In total four experiments were conducted: 3 at 2 bar of which 2 were inoculated and one was blank. These experiments lasted 3 weeks each. The first experiment was an inoculated experiment at 70 bar, which was terminated after 2 weeks.

Teflon sleeves were made to simplify the insertion and extraction of samples from the reaction chamber. Since not the entire length of the chamber was needed, two kinds of Teflon sleeves were made. Some were 'dummy' sleeves, made to reduce the amount of fluid needed to fill out the unused space within the reaction chamber as well as holding the experiment sleeves in place. These tubes had an inner diameter of 1 mm. The 'experimental' sleeves were 5 cm long with a diameter of 1.5 mm. At the top and at the bottom were

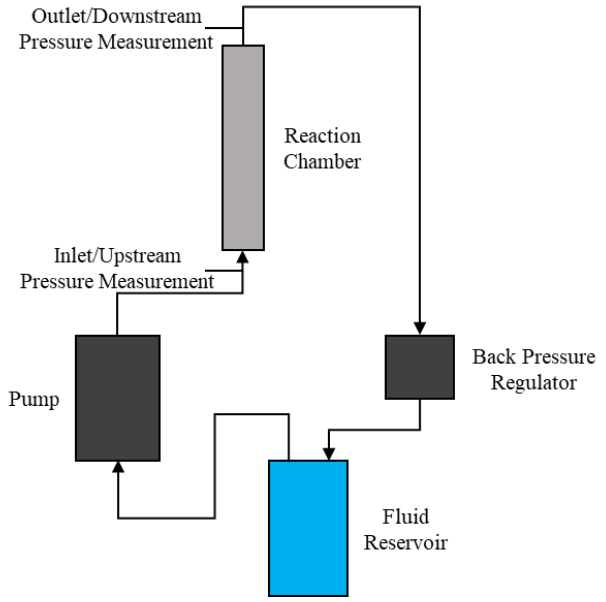

Figure 3.3: Schematic of the permeability experiments set-up.

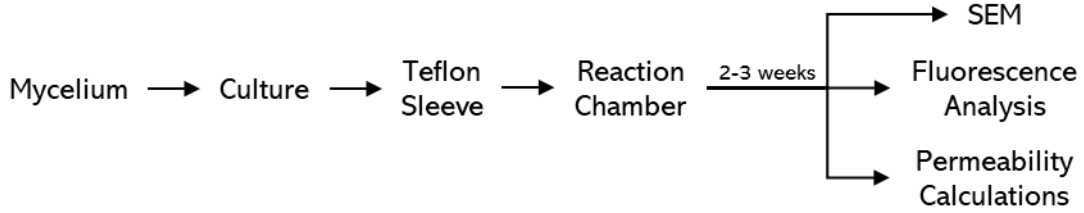

Figure 3.4: Flow chart of the permeability experiments. SEM = Scanning electron microscopy

small indentations for titanium filters. The filters that were used are 20 mm in diameter, 3 mm high and have a filtering capacity of 5 µm.

The assembly of the Teflon sleeves within the reaction chamber began with a dummy Teflon sleeve which was followed by three experimental Teflon sleeves. These were filled up with the grains of Icelandic basalt (see section 3.2.3.2). Fungi (see section 3.2.1) were introduced into the middle of the experimental Teflon sleeves by inserting a small piece of mycelium using a syringe with a needle (for the blank experiment this step was skipped). Each of these experimental sleeves were equipped with a Ti-filter at both the top and bottom ends, thereby ensuring a controlled environment for the experiment. Finally, after the experimental sleeves, another dummy Teflon sleeve was inserted into the reaction chamber. To ensure the integrity of the system and that the water flows through the sleeves and not around, each Teflon sleeve was encircled by O-rings, positioned at both the top and bottom ends. Because of the snug fit of the Teflon sleeves, a car jack was used to push the Teflon sleeves into the reaction chamber. A cross section of the reaction chamber is shown in Figure 3.5 to visualize the experiment set-up.

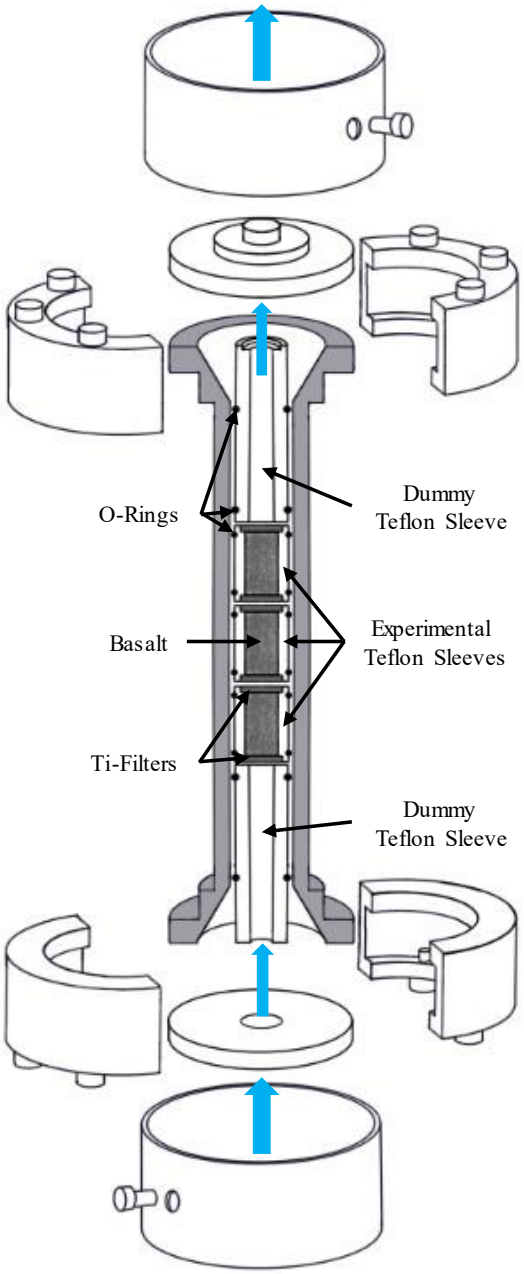

Figure 3.5: Configuration of the reaction chamber. Blue arrows indicate fluid flow direction.

Subsequently, the reaction chamber was closed and mounted into the flow-through autoclave. The system was slowly filled with the fluid used for the experiment (10 % Lennox broth (LB) in artificial seawater (ASW) for inoculated experiments and ASW for the blank experiment (see section 3.2.2)) with 3 ml/min. After the system was filled, the air bubbles were exhausted by pressurizing the system to 3-4 bar and then opening the bleeding valve. This was repeated until no further air bubbles were observed leaving the system.

Then, a pressure test was performed. This was done by increasing the pressure to 80 bar for the experiment at 70 bar and 5 bar for the experiments at 2 bar for 30-60 minutes. For this the flow rate was decreased to 0.1 ml/min, which was also the flow rate used during the experiments. The only exception to this was the blank experiment at 2 bar, because the pressure could not be maintained

with this flow rate. That is why the flow rate during the blank experiment was 0.15 ml/min. The pressure test was done to ensure that the system is tight enough for the experiment procedure. If no leaks are found the pressure was decreased to the experiment pressure and the experiment was started.

With the data recorded during the experiments, the permeability was calculated with Darcy's law (DARCY, 1856):

$$Q = \frac{k * A}{\mu * L} * (p_u - p_d)$$

Equation 1

With:

Q = Volumetric flow rate (m^3/sec)

k = Permeability (m^2)

A = Cross-section area (m^2)

L = Length (m)

μ = Dynamic viscosity of the fluid (Pa*sec)

p_u = Upstream pressure (inlet pressure)

p_d = Downstream pressure (outlet pressure)

If Equation 1 is rearranged for permeability, it results in:

$$k = \frac{Q * L * \mu}{(p_u - p_d) * A}$$

Equation 2

Equation 2 was used to calculate the permeability for the experimental Teflon sleeves, which makes the L = (3*(5 cm-2*0.3 cm) / 100, because three 5 cm long Teflon sleeves were used with each having 3 mm indentations on each side. This results in L = 0.132 m. The diameter of the experimental Teflon sleeves was 1.5 cm, resulting in A = (π * (1/2 * 1.5 cm)²)/ 10000 = 0.000177 m². The dynamic viscosity of the fluid is 0.00099958 Pa*s at 20 °C and 70 bar and 0.0010016 Pa*s at 20 °C and 2 bar (NATIONAL INSTITUTE OF STANDARDS AND TECHNOLOGY (2023), following HUBER et al., 2009).

Subsequent to the permeability experiments a test was executed to determine the uncertainty of the permeability measurements at the upstream and downstream measurement points. This was done by closing the system with an empty reaction chamber (i. e. no Teflon sleeves, filters and basalt grains). This way the upstream and downstream pressure should be the same as no obstacle can change the pressure. To recreate the experiment conditions water was run through the system at the same pressure and flow rate as during the executed experiments for ca.20 h. The deviation of the upstream and downstream pressures to each other is the uncertainty under the experimental conditions.

3.2 Materials

3.2.1 *Penicillium Rubens*

In this study *Penicillium rubens* was used for the experiments. The fungus was isolated by Dr. Oona Snoeyenbos-West (University of Arizona) and Dr. Magnus Ivarsson (Swedish Museum of Natural History) from dredged rocks from 756 m below sea level. The rocks were collected at the western slope of the intraplate volcano Vesteris Seamount in the Greenland basin (73.54047 °N, 9.15829 °E). The rocks were obtained during the cruise MSM86 by RV Maria S. Merian in August/September 2019 (more information about the cruise can be found in BACH et al., 2019). The culture was isolated and incubated at ambient conditions at 25 °C. The allocation of the fungal culture to *Penicillium rubens* followed ITS sequencing performed by Dr. Oona Snoeyenbos-West (University of Arizona) (M. Ivarsson, personal communication, 23rd May 2022). First, the culture was kept on potato glucose agar (PDA) manufactured by Sigma-Aldrich (4 g/l potato extract, 20 g/l dextrose, 15 g/l agar and 0.05 g/l chloramphenicol) and after it was handed over to Hannah Babel (University of Bergen) it was kept on Lennox broth (see 3.2.2.1).

Penicillium rubens belongs to the Ascomycota and is the first species in which penicillin was found (FLEMING, 1929). It belongs to one of the most common genera of fungi (CAMPOS et al., 2022).

The cultures were kept in the dark in closed, 25 ml, sterile falcon tubes. To ensure the purity of the cultures and to ensure the availability of the fungus for further experiments, clones have repeatedly been prepared by opening a culture and transferring small pieces of mycelium into new falcon tubes with prepared medium. As soon as a culture was opened and pieces transferred for culturing or experimental causes the respective culture was not used further. The antibacterial agent chloramphenicol was added to the cultures to a final concentration (fitted to the amount of medium used) of 0.05 g/l and refreshed once a month.

3.2.2 Fluids

3.2.2.1 Culture Media

During the course of this study two different culture media were used. One media used is Lennox broth following the protocol of BERTANI (1951), which was modified by LENNOX (1955) and sucrose was added following PATHAK (2020). This medium was chosen because of the fast growth of *P. rubens* it promotes. The other medium used is potato glucose (PG) (BLACK, 2020). PG was used because of its few constituents and its consequently closer resemblance of the fluids within the crust that are expected to be low in nutrients and carbon sources. The media were prepared with DI water and the constituents and concentrations can be found in Table 3.2.

Table 3.2: Constituents and concentrations of Lennox broth and potato glucose.

Lennox Broth		**Potato Glucose**	
Constituents	**Concentration**	**Constituents**	**Concentration**
Tryptone	10 g/l	Potato Starch	4 g/l
Yeast Extract	5 g/l	Glucose	20 g/l
NaCl	5 g/l		
Sucrose	20 g/l		

After preparing the media they were autoclaved at 121 °C for 20 min. Subsequently, chloramphenicol was added to a final concentration of 0.05 g/l. The chloramphenicol was refreshed once a month.

The cultures were grown on either the pure media (100 % PG/100 % LB) or in dilutions of the media. In those cases, the media was diluted in seawater (see section 3.2.2.2) and marked as e. g. 10 % LB or 10 % PG. Other diluents were used if specified. The dilutions were made to resemble the in-situ conditions of seawater but still promote fungal growth.

3.2.2.2 Seawater

The seawater used in this study was collected on the 25th of May 2022 in the Greenland Sea (79.419983 °N, 3.2728 °E) and subsequently stored protected from light at 4 °C. It was obtained at 2786.73 m depth, about 10 m above sea floor.

Before the seawater was used it was filtered over a 0.2 µm filter and autoclaved at 121 °C for 20 min.

3.2.2.3 Artificial Seawater

Table 3.3: Composition of the artificial seawater (following EMERSON & FLOYD (2005)).

Component	**Amount (g/l)**
NaCl	27.5
$MgCl_2 \cdot 6\ H_2O$	5.38
$MgSO_4 \cdot 7\ H_2O$	6.78
KCl	0.72
$NaHCO_3$	0.2
$CaCl_2 \cdot 2\ H_2O$	1.4
NH_4Cl	1
K_2HPO_4	0.05

The seawater was not sufficient in amount for the permeability experiments. Therefore, artificial seawater (ASW) was created following the recipe of EMERSON & FLOYD (2005). The recipe for artificial seawater is shown in Table 3.3 and was prepared with DI water.

For the inoculated permeability experiments (see 3.1.2) 111.11 ml of freshly mixed LB was added to each litre of ASW to create a 10 % LB in ASW. Subsequently the ASW or 10 % LB in ASW was autoclaved for 20 minutes at 121 °C.

3.2.3 Rocks

3.2.3.1 Leka Ophiolites

The syringe pump experiments (see 3.1.1) were undertaken using dunites collected by Hannah Babel on the island Leka from the Leka Ophiolite Complex in Norway. The rocks were collected at 65.102400 °N, 11.605200 °E. The island Leka is about 3.5 km off the coast of Trøndelag, central Norway. With U-Pb zircon ages the complex was estimated to be 497 ± 2 Ma old (DUNNING & PEDERSEN, 1988) and is built up of a block of the depleted upper mantle mainly in form of harzburgite, a block of crustal ultramafic cumulates, layered gabbros, basaltic dykes and pillow lavas (FURNES et al., 1988). The composition of the major elements of the dunites from the Leka ophiolite can be seen in Table 3.4 in weight percent.

Table 3.4: Whole-rock major element compositions of the Leka dunites and the Icelandic basalts in weight percent.

	Leka Dunites (IYER et al., 2008)	**Icelandic Basalts (OELKERS & GISLASON, 2001)**
SiO_2	34.34 – 37.02	48.12
Al_2O_3	0.02 – 0.40	14.62
Fe_2O_3	7.92 – 10.20	1.11
FeO	*N/A*	9.82
MgO	40.95 – 45.12	9.08
CaO	0.00 – 0.91	11.84
Na_2O	0.00 – 0.02	1.97
K_2O	0.00 – 0.03	0.29
TiO_2	0.00 – 0.01	1.56
MnO	0.00 – 0.01	0.19
P_2O_5	0.00 – 0.01	0.20
LOI	6.90 – 11.80	*N/A*

3.2.3.2 Icelandic Basalts

For the permeability experiments crushed basalts from the Stapafell Mountain, Iceland, were used. The basalt grains were provided by Andreas Beinlich (Freie Universität Berlin). Sieve analysis revealed that the majority of the grains are between 850 and 250 µm with a few grains slightly larger than 850 µm and a few grains between 250 and 125 µm.

Stapafell Mountain is located on the Reykjanes Peninsula on the south side of Snæfellsjökull, southwestern Iceland. Reykjanes Peninsular was covered by an ice sheet between 70 and 14 ka ago (MACLENNAN, 2008). Stapafell Mountain is a result of an eruption underneath the ice sheet, not long before its retreat, and is predominantly made up of pillow lavas (GEE et al., 1998, MACLENNAN, 2008). The basalt is tholeiitic and aphyric (GEE et al., 1998). The composition is similar to that of mid-ocean ridge basalts (GERM, 2000, OELKERS & GISLASON, 2001, GUDBRANDSSON et al., 2011). The major elements of the basalts are shown in weight percent in Table 3.4.

3.3 Analytical Methods

To evaluate the extent of the fungal impact on permeability, it is important to be able to estimate the biomass that the fungi can accumulate over a certain time and under certain conditions. To achieve this, two different methods were explored during this study for the estimation of fungal biomass in controlled, experimental settings. These methods are LOI and autofluorescence analysis. These methods work as explained below. Additionally, to get an impression of the growth architecture of the fungi, scanning electron microscopy (SEM) was used.

3.3.1 Loss on Ignition

Loss on ignition was used to analyse the samples of the first and second syringe pump experiments. For this the samples were first dried and then burned. The dry sample is weighed before and after the combustion in the furnace. The difference between the two weights is the amount of biomass lost during the combustion and hence the amount of biomass that was produced during the experiments.

The entire sample of the second syringe pump experiment (see Table 3.1) was transferred into a 50 ml centrifuge vial and covered with DI water. Subsequently, the samples were centrifuged for 20 min at 7600 x g. The supernatant was pipetted off and DI water was added to the sample to clean off the medium residue. The sample was centrifuged and the supernatant pipetted off again. This cleaning process was repeated three times to remove the entire medium residue before the samples were transferred into previously weighed ceramic crucibles.

Figure 3.6: Flow chart of the loss on ignition (LOI) biomass analysis method.

Of the samples from the first syringe pump experiment a subsample of ca. 4 g was directly transferred into the crucibles.

The wet samples were left to dry overnight at 105 °C. Subsequently the samples were weighed again before burning at 550 °C for 1 h following an internal protocol. After that the samples were weighed again. This process is shown in Figure 3.6. The LOI (g/kg) was calculated based on the weight loss during the burning process following Equation 3.

$$\frac{\text{Dried sample (g)} - \text{Burned sample (g)}}{\text{Dried sample (g)}} * 1000 = \text{LOI(g/kg)}$$

Equation 3

To test the accuracy of the LOI method, a validation experiment was executed by preparing a set of fungi from cultures and transferring them into crucibles. Additionally, samples of the Leka ophiolites (3.2.3.1) with a grain size from 1 - 4 mm were transferred into separate crucibles. The fungi and dunite grains were left to dry overnight at 105 °C. Then, they were weighed and to half of the dried fungal samples the dried grains were added and weighed once more before burning the samples at 550 °C for 1 and weighing them again. The LOI was then calculated with Equation 3.

3.3.2 Autofluorescence Analysis

Another method of estimating fungal biomass, next to LOI, is the autofluorescence analysis. For this the procedure introduced by MANSOLDO et al. (2020) was followed and slightly modified.

3.3.2.1 Theoretical Background

The autofluorescence analysis is using a component of the fungal cell membrane called ergosterol to assess the concentration of filamentous fungal biomass (MANSOLDO et al., 2020). Ergosterol is a sterol, a triterpenoid with a tetracyclic ring structure made up of three six-membered rings and one five-membered ring. The molecule has a hydroxyl group at the 3-beta position of the A-ring and a side chain at C-17 (see Figure 3.7). As a member of the cell membrane ergosterol is important for the fluidity, permeability and integrity of the cell membrane (LV et al., 2016) and it has been shown that fungi with a high ergosterol content can withstand environmental stress more effectively (FEDOSEEVA et al, 2021). Ergosterol is synthesized especially in later diverging fungi like species belonging to Dikarya, where it commonly is the major sterol (WEETE et al., 2010).

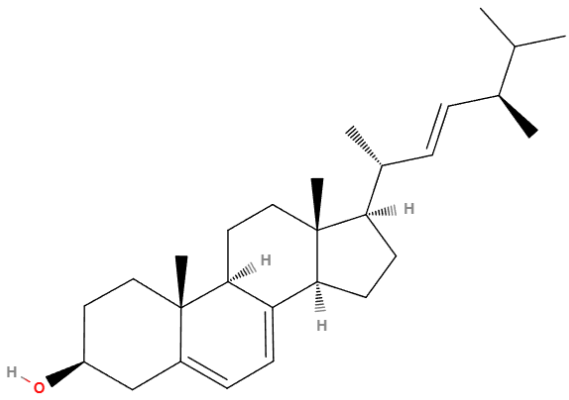

Figure 3.7: Structural formula of ergosterol.

The most widespread method of quantifying ergosterol in samples is high performance liquid chromatography, which is an expensive and labour-intensive technique (MANSOLDO et al., 2020). MANSOLDO et al. (2020), however, found another possibility of evaluating the amount of fungal biomass using the autofluorescence of ergosterol. This method is supposed to work even with interfering substances in the samples. MANSOLDO et al. (2020) used dried mycelium of *Schizophyllum commune* grown on culture medium (containing 30 g/l glucose, 1 g/l yeast extract, 0.5 g/l $MgSO_4 \cdot 7\ H_2O$, 1 g/l KH_2PO_4) to create the model. They mixed the mycelium with starchy solid residue to simulate the interfering substance.

Autofluorescence is a property of fluorophores and occurs when the fluorophore absorbs energy in the form of light, which transfers the molecule into an electronically excited state (KAROUI & BLECKER, 2011). The emission of light is a result of the molecule returning from the excited state back to the original electronically lower state and the wavelength of the emitted light corresponds to the difference in energy between both states. The wavelength of the emitted light is higher than the absorbed light.

The profiles are measured in an excitation emission matrix (EEM), which is also called a fluorescent fingerprint. The autofluorescence has already been used for quality assessment of various food products (KAROUI & BLECKER, 2011), for example the contamination of nutmeg by aflatoxin (AIYAMA et al., 2018), the prediction of the heating temperature of soymilk products (KOKAWA et al., 2017), the purity of buckwheat flour (SHIBATA et al., 2011) or the freshness of intact frozen fish (ELMASRY et al., 2015). But it has other applications as well, like the detection of deoxynivalenol, a toxin produced by certain fungi (FUJITA et al., 2010) as well as characterization of chromophoric dissolved organic matter from the Baltic Sea (KOWALCZUK et al., 2005).

The autofluorescence of a compound can be used to identify the concentration of that compound because the intensity of the fluorescence increases with increasing concentration (MANSOLDO et al., 2020) and in turn it can be used to estimate the fungal biomass by building a partial least squares regression (PLS) model. These models are useful when a prediction is required based on a large number of variables and a small number of observations (ABDI, 2003).

3.3.2.2 Building the Model

A total of seven models have been created following the procedure below wich was adapted from MANSOLDO et al. (2020). The created models were made for different media (100 % PG, 10 % PG, 1 % PG, 10 % LB, 1 % LB and 10 % LB in ASW). This was done to estimate the influence of the medium on the ergosterol content and with that on the model, as it has been found before that the medium can have a significant influence on ergosterol content of e. g. aquatic hyphomycetes (CHARCOSSET & CHAUVE., 2001) or salt-marsh fungi (NEWELL et al., 1987).

3.3.2.2.1 Extracting the Lipids

First, the fungal biomass was transferred from the media into a previously weighed 1.5 ml Eppendorf tube. Some fungal cultures exhibited mold-like growth at the fluid-air interface. Since there would not be an air-liquid interface in the experiments, this growth was removed and only the mycelial form suspended in the medium was transferred using a syringe and a needle. This was done to minimize the potential influence of this variable on the fungi because it was shown before that the fluorescence patterns of fungal samples submerged in fluids differed from surface-associated cultures (FEDOSEEVA et al., 2022).

Figure 3.8: Flow chart of the model data acquisition procedure.

Following, the medium residue was cleaned-off. To achieve this the samples were centrifuged. However, the centrifuge procedure followed in 3.3.1 led to the loss of fungal biomass. As a result, the procedure in MBARECHE et al. (2019) was followed by centrifuging the tubes at 14,000 x g for 10 min. The supernatant was pipetted off before adding 800 µl of DI water. Subsequently, the tube was shaken, centrifuged and the supernatant removed again. This cleaning process was executed a total of four times to remove the entire medium residue. Then, the sample was left to dry overnight at 40 °C. The Eppendorf tubes with the dried fungi were weighed and the fungal biomass calculated. An overview of the weights of the fungi used to create the models are listed in Table 3.5.

Afterwards, 1 ml of pure ethanol was added to the samples, which were then sonicated at 20 kHz for 1 h. This extraction method was chosen after HELENO et al. (2016), who tested different methods to extract ergosterol. The samples were then filtered over a 0.2 µm filter (either cellulose acetate membrane or polycarbonate) into a new Eppendorf tube. The old Eppendorf tube as well as the filter were flushed 4 times with a few drops of ethanol to ensure all lipids were transferred. The samples were left to evaporate at 30 °C over night. The lower temperature was chosen because of the lower evaporation point of ethanol compared to water.

For the first model created for 100 % PG, 1.3 ml ethanol per 200 µg fungal biomass was added to the dry samples. This was changed for the samples used to build the other models to ensure the robustness of the model and the applicability of the models to the experimental samples with unknown biomass amounts. To those samples 1.5 ml ethanol was added, independently of the biomass amount.

Table 3.5: Mass in µg of the fungi used to create the models. (PG = Potato glucose, LB = Lennox broth, ASW = Artificial seawater. Percentages of the media in seawater unless stated otherwise)

Sample No.	100 % PG	10 % PG	1 % PG	10 % LB	1 % LB	10 % LB in ASW
1	230	790	840	420	910	780
2	260	820	1200	490	660	480
3	220	390	540	640	1370	300
4	200	1020	520	350	1960	450
5	N/A	1050	740	590	480	450

For each model 5 fungal cultures were used, the only exception is the model created for 100 % PG, for which 4 samples were used. However, to create a stable model a large number of samples is needed. Because of this, a dilution series was created for each sample using the undiluted solution (D0) and adding ethanol. The dilution series were used to simulate samples of a smaller biomass amount to create a robust model. The dilution series is shown in Table 3.6.

The only exception from Table 3.6 is the model created for 100 % PG. For this model an additional dilution was created for each sample by mixing 62.5 µl D0 with 437.5 µl ethanol, creating a 1:8 or 12.5 % dilution.

Table 3.6: Dilution series created to build the model for the fluorescence measurements.

Dilution	Dilution factor/%	Amount of D0 (µl)	Amount of ethanol (µl)
D0	1:1 / 100 %		
D1	3:4 / 75 %	375	125
D2	1:2 / 50 %	250	250
D3	1:4 / 25 %	125	375
D4	1:5 / 20 %	100	400
D5	1:10 / 10 %	50	450

3.3.2.2.2 Fluorescence Measurements

A 96-well plate was used for the measurements and following an internal protocol each well was filled with 100 µl of the sample. Of each sample triplicates were measured. After filling the plate, optical adhesive foil was used to cover it to prevent evaporation during the analysis.

Subsequently the samples were measured in a PerkinElmer EnSpire 2300 Multilabel Reader at 25 °C with a 2 °C warmer condensation prevention. The measurement range for the excitation

wavelengths were 360-370 nm and for the emission wavelengths 400-600 nm with 2 nm wavelength increments each.

3.3.2.2.3 Preprocessing the Data

The processing and analysis of the data obtained by the autofluorescence analysis was conducted in the R environment (R CORE TEAM, 2022) and the steps are shown in Figure 3.9.

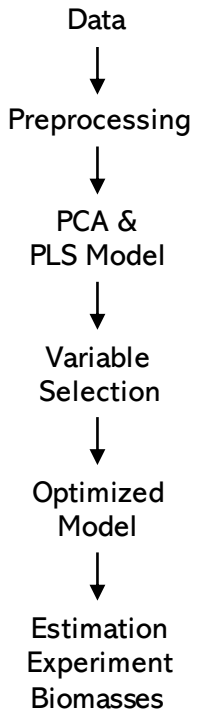

Figure 3.9: Flow chart of the model building procedure from the fluorescence data. PCA = Principal component analysis, PLS = Partial least squares regression.

The preprocessing and the visualization of the EEM data was performed using the EEM package (v1.1.1.9) (TRIVITTAYASIL et al., 2016). To do so the data was first brought into a shape accepted by the EEM package with the samples as rows and the excitation-emission wavelength pairs (ExEmPair) as columns.

After sorting the data, the delScattering2 function was used to remove excitation and emission ranges that can negatively affect the data analysis (TRIVITTAYASIL et al., 2016, AIYAMA et al., 2018), which are:

1. Regions where the emission wavelength is shorter than the excitation wavelength (EM ≤ EX)
2. Scattering rays and their second order light
3. Regions above second-order scattering (EM ≥ 2x EX)

These regions are removed because they usually are much stronger and unrelated to the fluorescence, resulting in a distortion of the results of the analysis (FUJITA et al., 2010, SHIBATA et al, 2011, AIYAMA et al., 2018).

Finally, the data was normalized by dividing each sample by the sum of the absolute value of all variables in the data set (TRIVITTAYASIL et al., 2016, TRIVITTAYASIL et al., 2017, AIYAMA et al., 2018). Then, to alleviate micro-multicollinearity, the data was mean-centered by subtracting the mean of all observations of one variable from all observations of that variable, resulting in a new mean of zero (IACOBUCCI et al., 2015).

An exemplary code chunk of the processing of the data can be found in Appendix 1.

3.3.2.2.4 Principal Component Analysis

A principal component analysis (PCA) is a method to compress multidimensional data into a few principal components that explain the variance of the data set by identifying variables that are not informative (FUJITA et al., 2010). A PCA was carried out using the stats package (R CORE TEAM, 2022) and was used to map the autofluorescence profile of *P. rubens* and find the important emission and excitation wavelength regions (MANSOLDO et al., 2020). It was also used to visualize the relationship between the samples.

3.3.2.2.5 Partial Least Squares Regression Model

By weighing the biomass of the fungi (see section 3.3.2.2.1) a Y matrix in which the dependent variables (the biomass) describe the observations (each sample) is created. Additionally, the fluorescence measurements result in a X matrix in which the observations each have multiple predictors (the intensity of the fluorescence for each ExEmPair). The goal of the partial least squares regression (PLS) model is to predict the Y matrix from the X matrix (ABDI, 2003).

To perform the PLS regression the samples were split randomly into a calibration (80 %) and validation (20 %) data set (MANSOLDO et al., 2020). Then the model was created using the pls package for R (LILAND et al., 2023) with a ten-fold cross-validation (MANSOLDO et al., 2020). The amount of components needed was tested with a validation plot and accordingly modified because small components often have collinearity (GELADI & KOWALSKI, 1986). In Appendix 2 is an exemplary code chunk to create the calibration and validation data frames as well as the PLS model.

The model was then tested against the validation set and evaluated using:

1. Root mean square error of cross validation (RMSECV)
2. Root mean square error of prediction (RMSEP)
3. Coefficient of determination for the calibration set (R^2CV)
4. Coefficient of determination for the validation set (R^2P)
5. The ratio of prediction deviation of the calibration set (RPDCV)
6. The ratio of prediction deviation of the validation set (RPDP).

However, the EEMs are composed of 1111 variables, which is a big amount of data. Not all of these variables are of necessity to build the model and could rather have a negative effect on it resulting from noise, redundancy and collinearity (MANSOLDO et al., 2020). As suggested by CHONG & JUN (2005), the variable importance in projection (VIP) values were used to select the variables for the optimized model. The higher the VIP value, the more important is that variable in the model. Consequently, only the variables with high VIP values are used for the optimized model. The VIP values were extracted from the PLS model using the R package chillR (LUEDELING et al., 2023). The VIP values were then plotted using the ggplot2 package (WICKHAM, 2016).

To determine the optimal ‘cut-off’ value for the VIP, a systematic loop was implemented, iterating through the VIP-value-range in increments of 0.01. First, the variables were filtered for the ones with a higher VIP value than the respective value of the iteration. Then, the ideal number of components were determined by first selecting the lowest number between the number of selected variables, the number of observations minus one, and the number of cross-validation folds. This was the maximum number of components possible for the model. With this amount of components, a model was created. The ‘selectNcomp’ function from the ‘pls’ package (LILAND et al., 2023) was then used to identify the optimal number of components based on the standard error of the

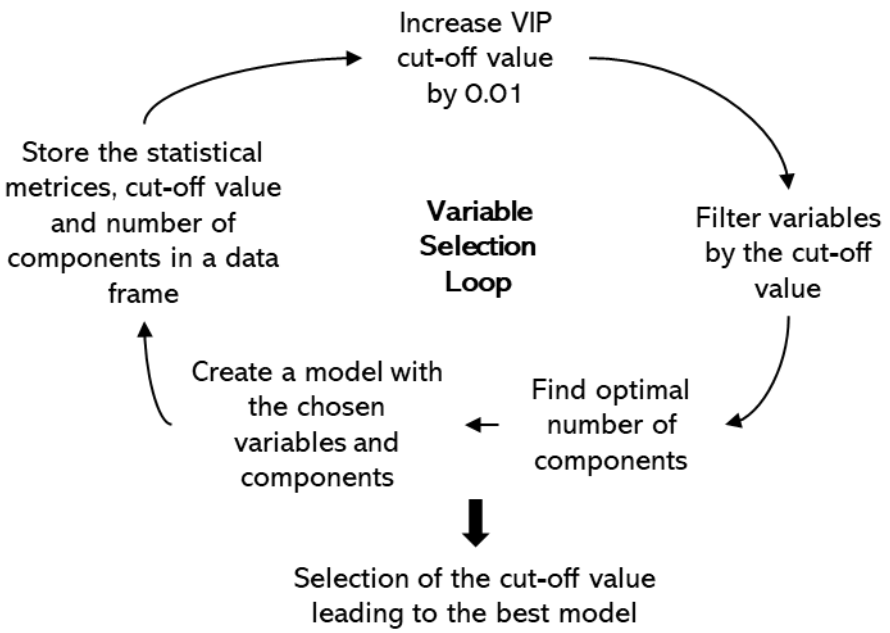

Figure 3.10: Outline of the selection process for the optimal VIP (Variable importance in projection) cut-off value to obtain the variables for the optimized model.

cross-validation residuals. This selected number of components was utilized to create an optimized model. Subsequently, the above listed statistical metrics were calculated and stored in a data frame.

To identify the best-performing model, a weighted sum approach was used, assigning equal weights to each statistical metric. An optimized model was then created using the variables with a VIP value higher than the determined 'cut-off' value corresponding to the model with the highest weighted sum.

The above-described procedure of selection for the variables to create the optimized model is shown in Figure 3.10 and as a code chunk in Appendix 3.

3.3.2.3 Analysis of Experimental Samples

To analyse the biomass of the syringe pump experiments as well as the permeability experiments the sample material was transferred into a 50 ml flacon tube. The glass vial or Teflon sleeves were flushed with DI water to make sure the entire content was transferred.

Then, the samples were centrifuged at 14.000 x g for 10 minutes. Carefully the supernatant was pipetted off and 5 to 10 ml DI water was added. The sample was shaken and centrifuged again. This cleaning procedure was executed a total of 4 times to ensure that the entire medium residue was cleaned off.

Subsequently, the samples were dried at 40 °C before adding 5 ml of ethanol and sonicating for 1 h at 20 kHz. The samples were then filtered over a 0.2 µm filter into a new 15 ml flacon tube. 3 ml of ethanol were added to the remaining sample material and filtered over the filter to make sure that the entirety of components was transferred. This was repeated 4 times. Because of the higher amount

of fluid and the resulting increased evaporation time, these samples were dried at 40 °C, unlike the model samples that were dried at 30 °C after extraction.

1.5 ml of ethanol was added to the dry samples to take up the constituents into solution again. The measurements were undertaken as described in 3.3.2.2.2.

The data was then preprocessed as described in section 3.3.2.2.3 with one difference in the mean centering. If the experimental samples would be mean centered to each other, the models would not work for absolute numbers since the biomass estimation would depend on which samples are processed together and with that mean centered to each other. To avoid this, the mean which was used to mean-centre the model samples was saved and applied at this point to the samples whose biomass estimates were wanted.

3.3.2.4 Validation Experiments

Two validation experiments were executed to evaluate the performance of the biomass estimation models. One experiment tested the variances between different runs and the other experiment tested the influence of the rock grains on the biomass estimations. One experiment was conducted using the 10 % LB model and the other using the 10 % LB in ASW model. These models were chosen because these media were used during the experiments.

The influence of the grains was tested using the 10 % LB model. For this experiment the fungal biomass of four fungal cultures were collected in precedingly weighed Eppendorf tubes and the medium residue cleaned off. After these samples were dried and weighed again, they were covered in medium sized Leka dunite grains (1-2 mm) (see section 3.2.3.1). Following, they were treated the same as the experimental samples (see section 3.3.2.3). The biomass was then estimated using the 10 % LB model.

The run variability was tested for the 10 % LB in ASW model. Two fungal cultures were prepared the same way as the samples used to build the model (described in sections 3.3.2.2.1 to 3.3.2.2.3). The 10 % LB in ASW model was then used to estimate the fungal biomass.

Because the biomass of the samples in both test experiments is known, R^2P, RMSEP and RPDP can be used to evaluate the models and the estimated biomasses can be compared to the measured ones.

3.3.3 Scanning Electron Microscopy

One sample of the fourth syringe pump experiment (sample ID: I – Med-4) and one sample from the 70 bar and one sample from each of the two 2 bar inoculated permeability experiments were prepared for scanning electron microscopy (SEM). For both samples of the 2 bar inoculated permeability experiments the supernatant was pipetted off. Subsequently the basalt grains of the 2 bar inoculated permeability experiments as well as the entire samples of the fourth syringe-pump experiment and the 70 bar permeability experiment were each covered in 2.5 % glutaraldehyde in phosphate buffered

saline in order to fixate the cells in a living state. The samples were then left in the fridge at 4 °C for at least 48 h.

The samples were dehydrated using a dehydration series of ethanol. Ethanol was mixed with DI water to create a series of 10 %, 30 %, 50 %, 70 % and 90 % ethanol. The last step was pure ethanol which has a concentration of about 96 %.

The glutaraldehyde was pipetted off from underneath the samples using a thin, long needle. The dehydration solutions were added carefully to the samples that were subsequently moved around to spread the solution over the entire sample.

The dehydration series was successively pipetted on the samples in an amount sufficient to cover the entire sample. The dehydration solution was left on the sample for 10 min before it was pipetted off in the same manner as the glutaraldehyde before the next step of the dehydration series was pipetted on. The last step of pure ethanol was repeated twice. For the sample material of the 2 bar permeability experiments only the 50 %, 70 % ethanol solutions were used, followed by two rounds of pure ethanol.

Finally, the samples were left to dry overnight in the fume hood and then stored at room temperature.

The samples were then mounted on an aluminium stub using two-sided carbon tape. A Polaron SC502 sputter coater was used to coat the samples with a gold (40 %) palladium (60 %) coating. Subsequently, the samples were analysed using a Zeiss Supra 55 VP scanning electron microscope. Imaging was conducted using the SE2 detector.

4 Results

4.1 Biomass Measurement Methods

4.1.1 Loss on Ignition

The initial biomass analysis was conducted using the LOI method. Overall, are the differences between the samples from the same experiment relatively small (first syringe pump experiment: range of 22 g/kg, second syringe pump experiment: range of 19.7 g/kg), especially compared to the difference between the two experiments, that have collectively a range of 70.3 g/kg (see Figure 4.1).

In the first syringe pump experiment, the samples in which 1 % LB was used, show the most LOI, while the ones grown on 1 % PG show the least LOI. In the second syringe pump experiment the samples in which the medium sized grains were used show the most and the samples with the largest grain size the least LOI, irrespective of the samples being inoculated or blank. Generally, are the differences between the inoculated samples and their respective blank samples negligible as they are mostly within the range of standard deviation (compare Figure 4.1). It is evident that the LOI is significantly less in the second syringe pump experiment compared to the first one.

The LOI of the samples was further investigated by plotting the LOI in g/kg against the position of the sample inside the oven, which can be seen in Figure 4.2. In these plots the samples are arranged

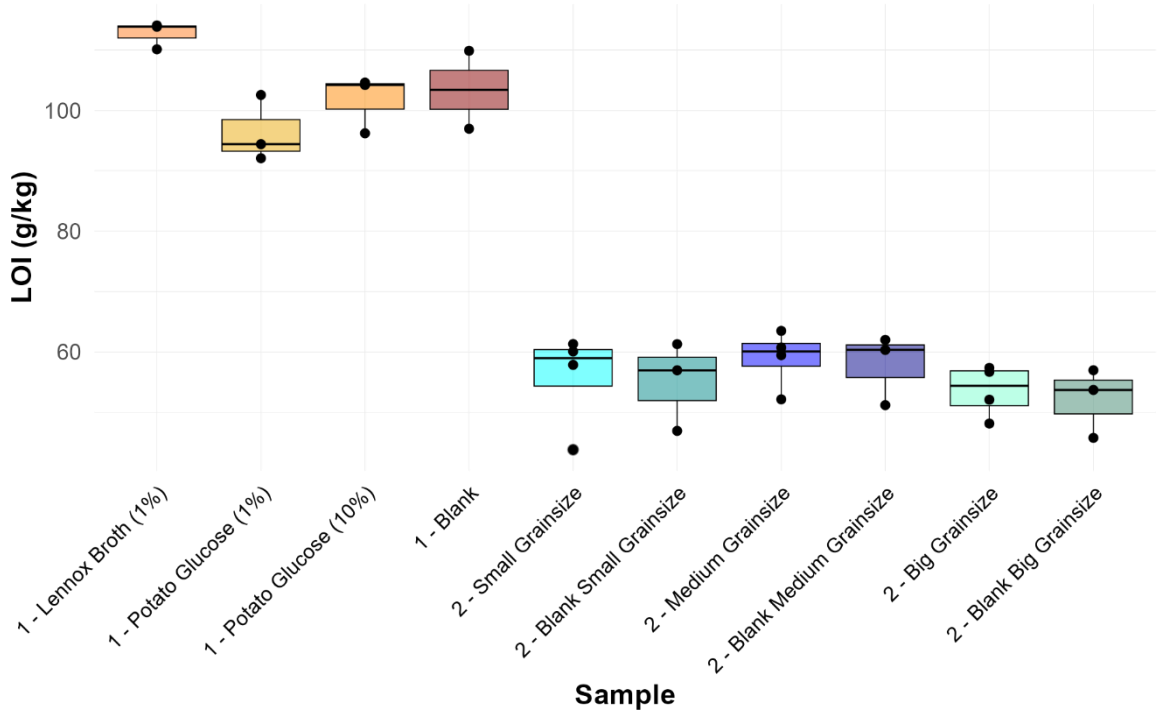

Figure 4.1: Box plot of the loss on ignition (LOI) (g/kg) measurements of the first two syringe pump experiments (marked with 1 and 2 respectively). The black dots represent each measurement individually. Percentages are the medium percentages in seawater.

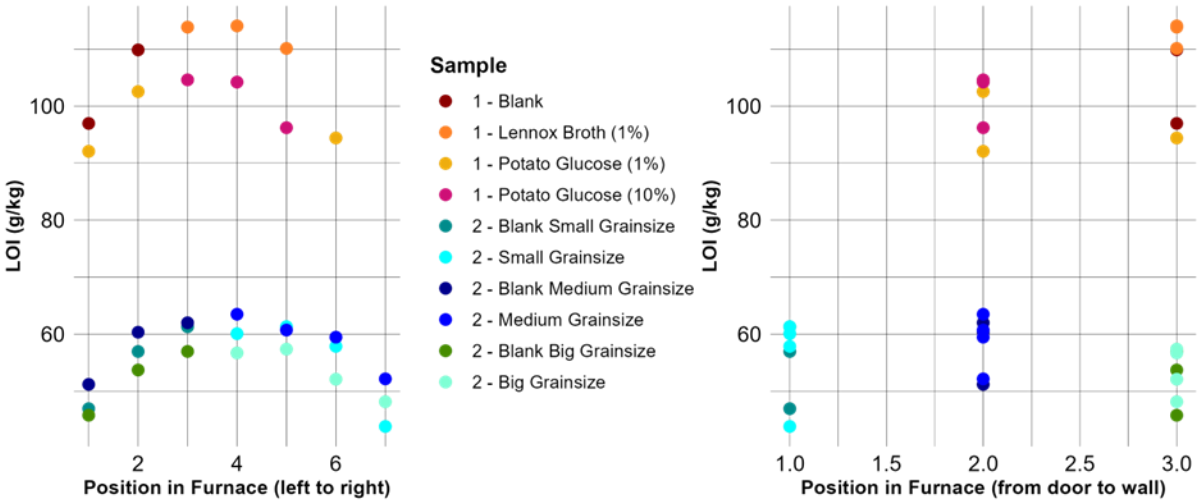

Figure 4.2: Position of the samples of the first two syringe pump experiments (marked with 1 and 2 respectively) in the furnace. The left shows the position from left (= 1) to right (= 7) and the right plot shows the position from close to the door (= 1) to close to the back wall (= 3). LOI = Loss on ignition. Percentages are the medium percentages in seawater.

in a sequential manner on the x axis where the lowest number denotes the leftmost sample or the one closest to the door and the largest number the rightmost sample or the one closest to the backwall. This was done because HOOGSTEEN et al. (2015) describe a near-door effect, wherein samples closer to the door exhibit less LOI than those that are further inside the oven. In the plot showing the position of the samples relative to the sidewalls, the samples are arranged and a bow shape (see Figure 4.2). This visualizes the trend that the closer the samples were to one of the walls, the less LOI took place. On the right plot in Figure 4.2, the position of the samples in the furnace is depicted from close to the door (1 on the x-axis) to the back wall of the furnace (4 on the x-axis). In this case no pattern in the sample arrangement is visible.

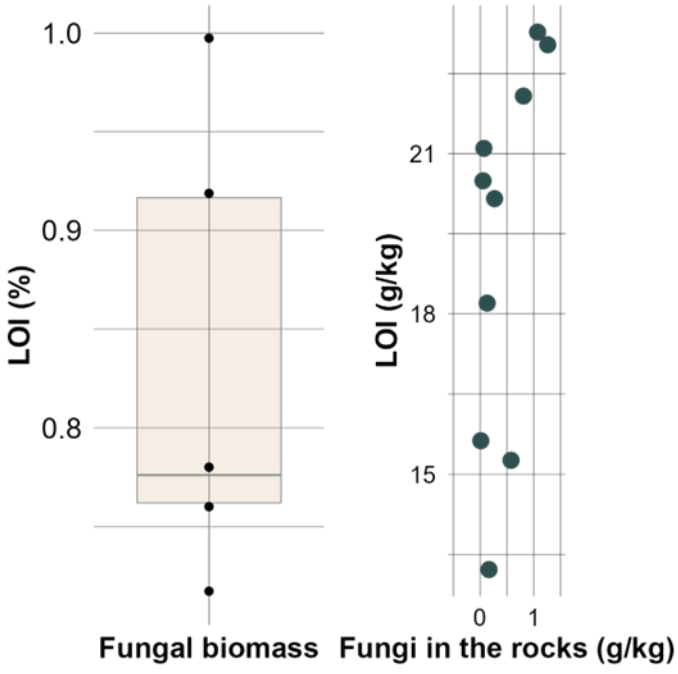

Figure 4.3: Plots for the validation test of the loss on ignition (LOI) method. To the left is the box plot showing the LOI of the fungi alone with black dots marking individual samples and on the right is the comparison between the fungi covered with rocks in g/kg and the LOI of the same samples in g/kg.

Following to these results a validation experiment was conducted to assess the accuracy and precision of the LOI method relating to the fungal biomass. To do this it was tested how effectively fungal biomass is burned and how accurate the LOI represents

the fungal biomass when it is burned in association with dunite grains. The results of these test experiments can be seen in Figure 4.3. High percentages (70-100 %) of the fungal biomass were combusted in the oven in the validation experiment without the dunite grains. However, five samples were excluded from these results because these samples had either a negative weight after the drying process or no weight, i. e. the crucibles weighed the same or were lighter than before the fungal biomass was added and dried.

The right plot in Figure 4.3 shows the LOI in g/kg plotted against the weight of fungal biomass covered by the grains in g/kg of the same samples to allow a direct comparison. The LOI of all samples is significantly higher (13.2 g/kg-23.3 g/kg) than the fungal biomass that was added to the dunite grains (0.01 g/kg-1.3 g/kg).

4.1.2 Autofluorescence PLS models

4.1.2.1 Model Building

A total of 6 PLS models were created for *P. rubens* grown on different media-diluent compositions that are 1 % LB, 10 % LB, 10 % LB in ASW, 1 % PG, 10 % PG and 100 % PG (with the diluent being seawater unless stated otherwise). This was done to compare the influence of the media on the model.

The fluorescence measurements resulted in 1111 ExEmPairs with varying intensities. One clear pattern was observable: Across all samples the measured EEMs showed two stripes of increased intensity at the emission wavelengths 400-420 nm and 430-450 nm and spread across the entire excitation range. However, depending on the dilution the areas of highest intensities are clearly defined or vague. For example, in Figure 4.4 4 exemplary EEM plots of samples measured for the 10 % LB in ASW model are shown. The upper two plots show the EEMs of an undiluted sample, to the left before the processing procedure described in section 3.3.2.2.3 and to the right after the processing. Underneath are the respective EEMs of a blank sample. In the undiluted sample there are two clearly defined zones of pronounced intensity in the excitation wavelength area of 360-361 nm. In the blank sample the zones of higher intensity are on the lower end of excitation wavelengths as well, however, they are more spread out.

It should also be noted that the intensity of the fluorescence varied depending on the dilution. For example, the unprocessed sample shown in Figure 4.4 has an intensity of up to roughly 1200 while the maximum intensity in the blank sample is about 800.

Another difference between the undiluted samples and those of less biomass amount is an area of raised intensity at emission wavelengths of 450-550 nm and a peak at emission wavelength 361 nm (see Figure 4.4). This area of raised intensity is not visible in the blank samples.

The trends between the processed EEMs of high and low biomass amounts are inversed as a result of the mean-centering. This means at wavelengths where the samples with a high biomass

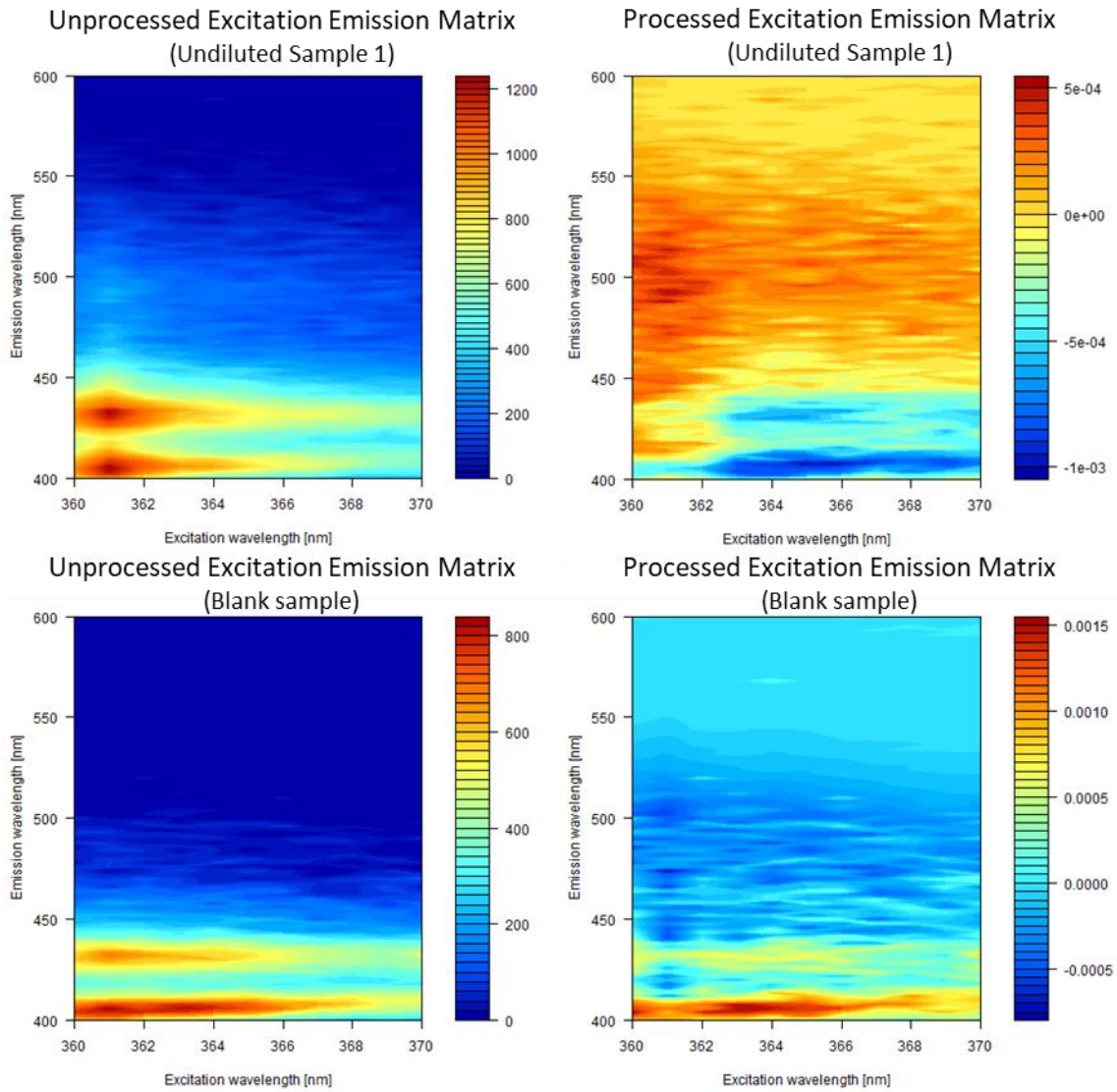

Figure 4.4: Comparison of unprocessed and processed Excitation and Emission Matrices (EEM) of an undiluted and a blank sample of the 10 % Lennox brother in artificial seawater model. Note that the colour scales have different ranges.

amount have positive peaks, the samples of low or no biomass amount have negative ones and vice versa (compare Figure 4.4). The patterns are more diffuse in the processed EEMs than in the unprocessed EEMs. However, the above-mentioned bands of high intensity in the unprocessed samples are also visible as negative (samples with high biomass amount) or positive (samples with low biomass amount) bands. But, in this case the peaks are more in the medium to higher range of the excitation wavelengths compared to the unprocessed EEMs (see Figure 4.4).

After processing the data, a PCA was conducted on the EEMs. This allows a comparison between the different growth media as well as the seawater against the ASW. Standing out are two areas of high loadings in the principal component (PC) 1 that are located at the excitation wavelengths of 360-370 µm. One is at the emission wavelength of ca. 430-440 µm and the other one, which is the higher and more pronounced one in all models, at the emission wavelength of 400-425 µm. Within

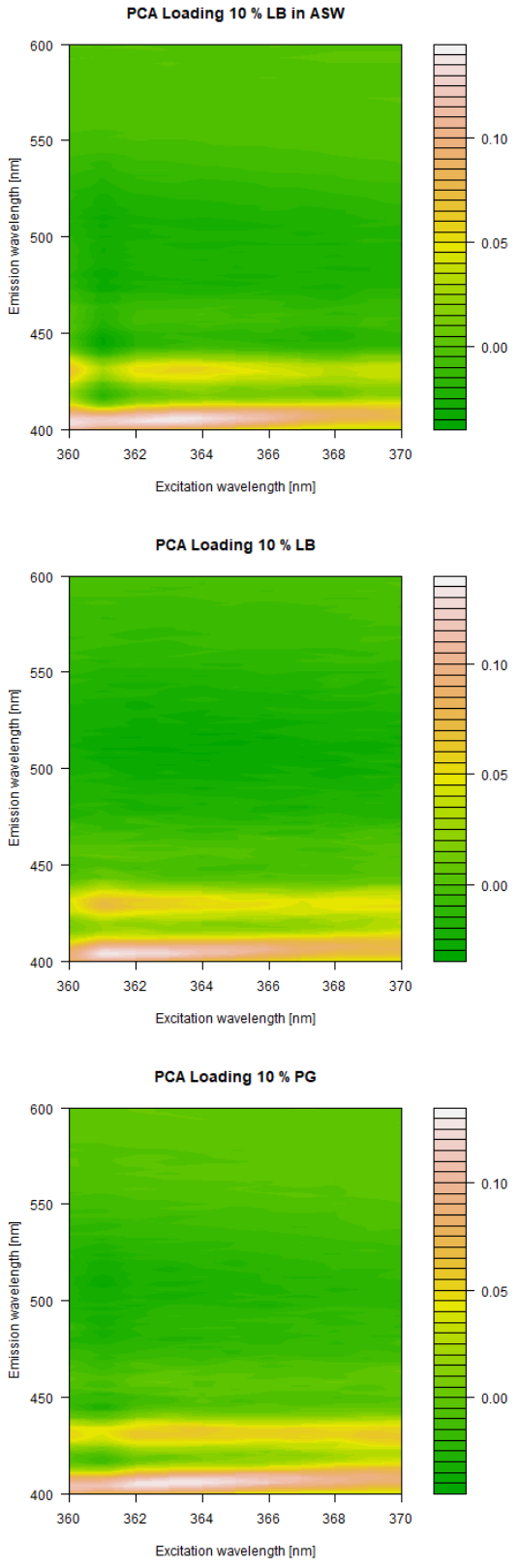

Figure 4.5: Loading plots of the principle component 1 of the principle component analysis (PCA) of the models based on 10 % lennox broth (LB) in artificial seawater (ASW), 10 % LB in seawater and 10 % potato glucose (PG) in seawater.

these bands the intensities of the loadings over the excitation wavelength range varies slightly in each model as well as between the models. The highest intensities are between the excitation wavelengths of 360-366 nm. Exemplary loading plots of the ExEmPairs of PC 1 for the 10 % LB in ASW model, the 10 % LB model and the 10 % PG model are shown in Figure 4.5.

In comparison to the unprocessed EEMs (compare Figure 4.4 on the left) it is striking that the areas of high loading corresponds roughly to the areas of high intensity of the fluorescence.

The first partial least squares regression model for each growth medium was based on this processed data. As described in section 3.3.2.2.5 the models were subsequently improved by filtering the variables using the VIP values of the initial models. The pattern established in the EEM plots as well as the loadings plots is continued in the VIP values as there are two pronounced areas of high values between the emission wavelengths of 400-420 nm and 425-440 nm. Especially the lower emission wavelength range has high values at the excitation wavelengths of 362-366 nm. Another area of increased values is at emission wavelengths 475-550 nm and excitation wavelengths of 361-362 nm. This area was also visible in the unprocessed EEM of the undiluted sample (Figure 4.4). An example of the VIP values for each ExEmPair is shown in Figure 4.6 based on the VIP values of PC 1 of the 10 % LB in ASW model

Based on the VIP values with the procedure described in section 3.3.2.2.5 the ExEmPairs used for the optimized model were chosen. Only variables with a VIP value higher than the designated ‘cut-off’ value were used. This

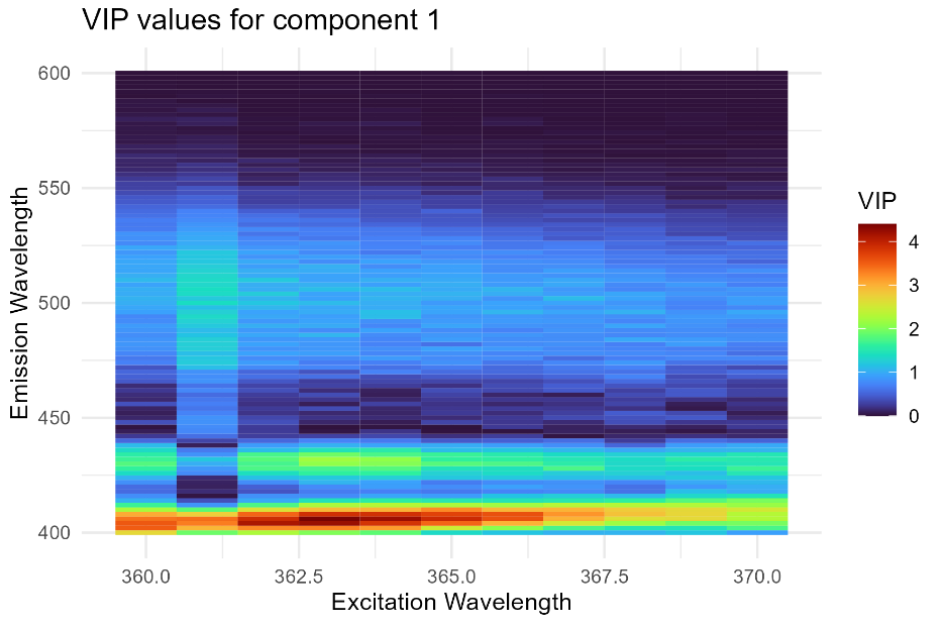

Figure 4.6: Heat map of the variable importance in projection (VIP) values of component 1 of the excitation and emission wavelength pairs for the model based on 10 % lennox broth in artificial seawater. Wavelengths are given in nm.

procedure not only led to varying cut-off values but also to different numbers of variables used in the optimized models. Generally, the same pattern as in the VIP values shown in Figure 4.6 is visible in the usage of the variables as well. The two pronounced bands at the lower end of the emission wavelengths, that were defined before, are visible in the use of the ExEmPairs too as bands of high usage. However, within these bands the area of highest numbers of usage in the optimized models is not at the lower end but at the higher end of the excitation wavelengths. Additionally, the ExEmPairs at emission wavelengths of 475-550 nm along the entire range of excitation wavelengths have an increased usage as well. A heat map illustrating the frequency of usage of specific ExEmPairs in the optimized models is shown in Appendix 4.

Table 4.1: The variable importance in projection (VIP) cut-off values and the resulting number of variables used for each biomass estimation model. (PG = Potato glucose, LB = Lennox broth, ASW = Artificial seawater. Percentages of the media in seawater unless stated otherwise)

Model	**VIP cut-off value**	**Number of variables used**
1 % PG	0.991	187
10 % PG	0.181	825
100 % PG	1.671	114
1 % LB	0.03	1080
10 % LB	0.123	972
10 % LB in ASW	0.42	621

In Table 4.1 the cut-off value of each model is shown together with the resulting number of variables used in the optimised models. It is noticeable that the range of numbers used in the optimized models is broad: The lowest number of variables used is 114 in the model based on the fungi grown on 100 % PG. The highest number is 1080 for the model based on 1 % LB. This is a great proportion of the variables, considering that the total number of variables is 1111. This model also has the lowest VIP cut-off value with 0.03. The highest VIP cut-off value has the 100 % PG model with 1.7.

This optimization method resulted in a dissimilar magnitude of improvement between the models. For example, in Table 4.2 the change of the in section 3.3.2.2.5 listed statistical metrices are shown for the model based on fungi grown in 10 % LB in ASW as an example for noticeable improvement and for the 10 % LB model as an example for negligible differences. Especially pronounced improvements in the 10 % LB in ASW model was made in R^2CV and RMSECV, which evaluate the biomass estimations of the calibration data (more on that in section 5.1.1). This means that the biomass estimations of the calibration data are closer to the measured biomasses after the optimization step. This is visualized in Appendix 5 as plots of the model and the optimized model of the 10 % LB in ASW.

Table 4.2: Comparison of the changes in the statistical metrices between the model and the optimized model of 10 % lennox broth (LB) in artificial seawater (ASW) as an example for improvement and 10 % LB in seawater as example for minimal change. R^2CV = Coefficient of determination for the calibration set, RMSECV = Root mean square error of cross validation, RPDCV= The ratio of prediction deviation of the calibration set, R^2P = Coefficient of determination for the validation set, RMSEP = Root mean square error of prediction, RPDP = The ratio of prediction deviation of the validation set

	10 % LB in ASW Model		**10 % LB Model**	
	Model	**Optimized Model**	**Model**	**Optimized Model**
R^2CV	0.7530	0.9889	0.8466	0.8466
RMSECV	9.3242	4.2933	8.2962	8.2966
RPDCV	1.8022	2.4670	2.5532	2.5529
R^2P	0.7564	0.7262	0.8763	0.8764
RMSEP	10.3515	10.6587	7.7417	7.7412
RPDP	2.2829	3.1250	2.5274	2.5271

Additionally, as visible in Table 4.2, also the RPDCV and the RPDP values of the 10 % LB in ASW model improved with the optimization step. This means that the accuracy of the model improved with the optimization step for both the calibration as well as the validation data set.

With the weighted sums technique introduced in section 3.3.2.2.5 to find the best VIP cut-off value, the statistics of all optimized models created in this study were evaluated. It was estimated that the optimized 1 % PG model is altogether the best model. The statistical metrices for all optimized models created in this study are shown in Table 4.3 and for comparison, the statistics of the model created in MANSOLDO et al. (2020) were added in Table 4.3 as well. That model has overall better values than the models created in this study. This is especially pronounced for RMSECV and RMSEP. Generally, are the values evaluating the cross-validation of the calibration data set better than the values of the validation data set.

Table 4.3: Statistical metrics of the optimised models. For comparison the results of the model created by MANSOLDO et al., (2020) were added as well. R^2CV = Coefficient of determination for the calibration set, RMSECV = Root mean square error of cross validation, RPDCV= The ratio of prediction deviation of the calibration set, R^2P = Coefficient of determination for the validation set, RMSEP = Root mean square error of prediction, RPDP = The ratio of prediction deviation of the validation set, PG = Potato glucose, LB = Lennox broth, ASW = Artificial seawater. Percentages of the media in seawater unless stated otherwise

	R^2CV	**RMSECV**	**RPDCV**	**R^2P**	**RMSEP**	**RPDP**
1 % PG	0.9537	7.9129	3.3795	0.8981	9.3816	3.2689
10 % PG	0.8562	10.7833	2.6374	0.7116	12.1405	2.4091
100 % PG	0.8081	5.7502	1.3978	0.4133	7.2454	1.2989
1 % LB	0.8491	13.7591	2.1488	0.7358	12.8820	1.4529
10 % LB	0.8466	8.2966	2.5529	0.8764	7.7412	2.5271
10 % LB in ASW	0.9889	4.2933	2.4670	0.7262	10.6587	3.1250
MANSOLDO et al. (2020)	0.939	0.0731	4.07	0.936	0.0797	4.06

4.1.2.2 Model Testing

To validate the fluorescence measurements as a biomass estimation method two test experiments were performed. The first one was conducted on the 10 % LB model. In this case biomass from a fungal culture was collected and weighed and then covered in grains from the Leka dunites (section 3.2.3.1) that were also used in the syringe pump experiments. This experiment was done to evaluate the influence of the grains on the model performance.

Table 4.4: Validation results of the 10 % lennox broth model

Sample No.	Measured Biomass (µg)	Estimated Biomass (µg)	Standard Deviation of Estimation
1	160	421.86	17.54
2	1060	376.51	6.63
3	1010	391.88	16.98
4	820	491.33	11.16
Ethanol	0	-541.04	14.89
Ethanol	0	-550.62	10.50

After the fungal biomass was covered with the dunite grains, the samples were treated like the samples from the syringe pump experiments (see section 3.3.2.3). The measured biomasses with the means and standard deviations of the estimated biomasses of the triplicate measurements are shown in Table 4.4. The estimated biomasses of the validation experiment deviate from the measured biomasses significantly with 260 to up to almost 700 µg differences, which is far outside the standard deviation range (6.6-17.5 µg). With one exception the biomasses were underestimated. The pure ethanol samples have biomass estimations in the negative range.

Table 4.5: Validation results of the 10 % lennox broth in artificial seawater model

Sample No.	Measured Biomass (µg)	Estimated Biomass (µg)	Standard Deviation of Estimation
1 D0	750	647.62	15.32
1 D1	562.5	544.24	14.85
1 D2	375	469.99	20.15
1 D3	187.5	358.55	24.75
1 D4	150	347.98	27.50
1 D5	75	304.70	45.34
2 D0	870	642.64	3.20
2 D1	652.5	572.62	18.78
2 D2	435	516.14	17.17
2 D3	217.5	392.31	35.93
2 D4	174	390.51	12.75
2 D5	87	292.25	27.44
Ethanol	0	281.21	16.54
Ethanol	0	280.40	10.75

The validation test conducted for the 10 % LB in ASW model was done to evaluate the differences between separate measurement runs and test the performance of the model on a separate data set. This test experiment resulted in estimated biomass ranges that are not as substantially different from the measured biomasses at it is the case in the validation experiment for the 10 % LB model. The samples for this experiment were prepared the same way as the samples that were used to build the models. The differences between the estimated and the measured biomasses are in the range of 18.3-281.2 µg, which is partially in the standard deviation range of 3.2 to 27.5 µg. The results of this test experiment are shown in Table 4.5 and while the blank samples are overestimated the samples with the highest biomass amounts are underestimated. The calibration and validation samples used to build the model and the samples of the test experiments are plotted in Figure 4.7 to visualize the differences of the estimated to the measured biomasses as well as the differences between the models,. The slope of the regression line of the test experiment for the 10 % LB model is parallel to the slopes of the regression lines of the model data, but it is shifted downwards. The regression line of the validation experiment for the 10 % LB in ASW model intersects the regression lines of the model data. However, in this case the slope is not as steep as the ones of the model data.

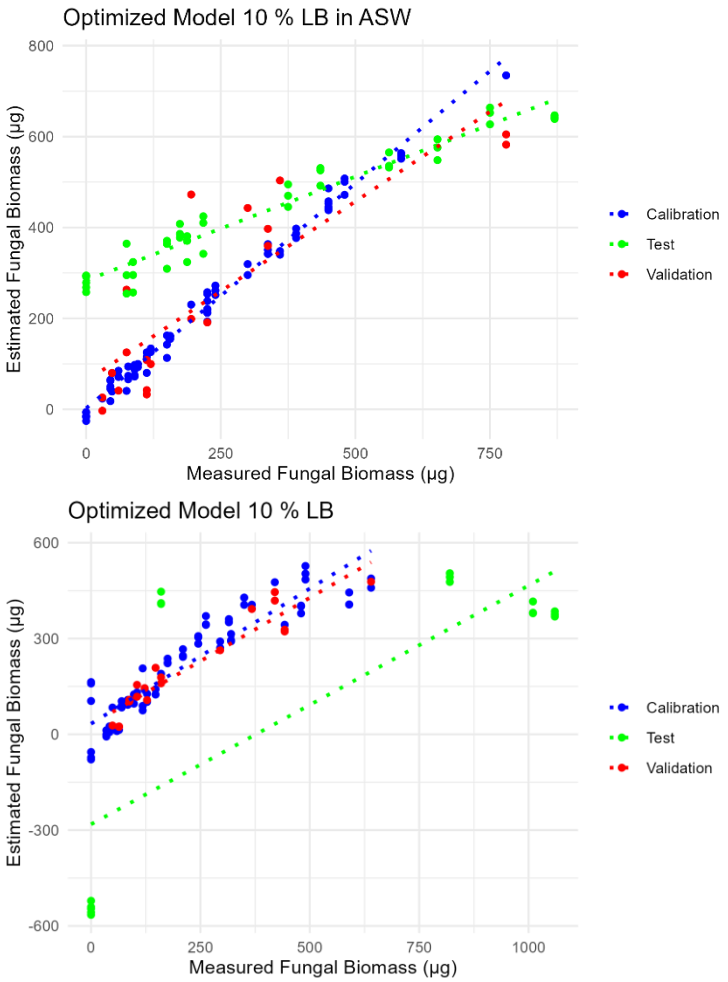

Figure 4.7: Plots of the results of the validation (test) experiment for the optimized 10 % lennox broth (LB) in artificial seawater (ASW) and the 10 % LB models

To compare the performance of the models on the validation experiment data with their performance on the training data, R^2P, RMSEP, RPDP were calculated for the test data. The results are shown in Table 4.6. The RPDP values fall within the range of those for the trainings data, while the RMSEP values are slightly below average (compare Table 4.3). The R^2P results deviate the most and indicate the poorest performance compared to the trainings data.

Table 4.6: Statistical metrices of the validation tests. LB = lennox broth, ASW = artificial seawater (if not specified then medium is in seawater), R^2P = Coefficient of determination for the validation set, RMSEP = Root mean square error of prediction, RPDP = The ratio of prediction deviation of the validation set

	10 % LB	**10 % LB in ASW**
R^2P	-0.26	0.54
RMSEP	22.81	13.68
RPDP	2.53	3.13

To evaluate and compare the models further, six blank, i. e. pure ethanol measurements were done. The biomasses for these measurements were estimated using the 10 % LB model and the 10 % LB in ASW model. The results are shown in Table 4.7. They show a striking difference between estimated biomasses between each other as well as the true biomass. Neither of the estimations resulted in a biomass of 0 or close to 0. The 10 % LB model was the furthest off with estimations around -545 µg while the 10 % LB in ASW model resulted in estimated biomasses of around 132 µg. This is an estimation range of ca. 750 µg between the highest and the lowest biomass estimation of both models. This is significantly higher than the standard deviation of 13.7 µg (10 % LB) or 7.6 (10 % LB in ASW).

For a more thorough comparison, a table of all blank samples measured during the course of this study and their respective estimated biomasses by the 10 % LB and 10 % LB in ASW model, is provided in Appendix 6.

Table 4.7: Comparison of blank (pure ethanol) measurements and the estimated biomass in µg within these measurements received from the 10 % lennox broth (LB) model and the 10 % LB in artificial seawater (ASW) model in µg. (Stdv = standard deviation)

Measurement Number	**10 % LB Model**	**10 % LB in ASW Model**
1	-557.45	185.41
2	-521.41	154.67
3	-544.28	167.62
4	-546.06	116.25
5	-540.68	78.31
6	-565.14	89.28
Stdv	13.74	39.98

4.2 Syringe Pump Experiments

The syringe pump experiments were conducted to get an impression of the biomass the fungi can accumulate under a certain amount of time and under certain conditions to test the influence of variables like grain size and culture medium on the biomass development.

The syringe pump experiments ran for two weeks each but at two separate occasions (experiment 2 and experiment 4) a syringe pump stopped before it was manually halted. During the transfer of the samples of experiment 4 into the falcon tubes it was noted that fungal mycelia had grown into the needles of the inlet-syringes. This biomass could have obstructed the fluid flow of the inlet needles and increased the pressure the pump needed to exert on the syringes, which ultimately lead to the automatic shutdown of the pump observed in this experiment (see section 3.1.1). This can happen if too much pressure needs to be exerted to pump the fluids. It can be assumed that this observed growth into the inlet-syringe needle was also the reason for the shutdown of the syringe pump in experiment 2.

To make sure that the entire biomass that developed within the experimental timeframe gets transferred, the rest of the fluids within the inlet needles of experiment 4 was emptied into the falcon tubes to the respective samples. This pushed the mycelia within the needles out.

The samples of the first two syringe pump experiments were analysed using LOI, these results are presented in section 4.1.1.. The samples of the third and fourth syringe pump experiments were analysed using the fluorescence analysis method and SEM (see sections 3.3.2 and 3.3.3).

4.2.1 Fluorescent Analysis

After the processing of the samples (as described in 3.3.2.3), triplicates of each sample were analysed for the autofluorescence in the samples. Two areas of high intensity were observed in the experimental EEMs. One lies at the emission wavelength of 400-420 nm and the other at 425-450 nm. Both are bands across the entire excitation wavelength range with peaks at the excitation wavelengths of 360-364 nm. Figure 4.8 displays the raw EEMs of an inoculated sample of the third syringe pump experiment (big grain sizes) and the fourth syringe pump experiment (medium grain sizes) in which this pattern can be seen.

To estimate the fungal biomass the 10 % LB model was applied to the measurements. This model was chosen because it is based on fungi grown on the same medium that was used during the experiments. It is conspicuous that there is no significant difference between the inoculated samples and the blank samples (see Figure 4.9 and Table 4.8).

The estimated biomasses have a range of roughly 300 µg for both experiments with the mean of experiment 4 being about 100 µg lower than the mean of experiment 3, regardless of the samples being inoculated or not. While the inoculated samples with the big grains have estimated biomasses

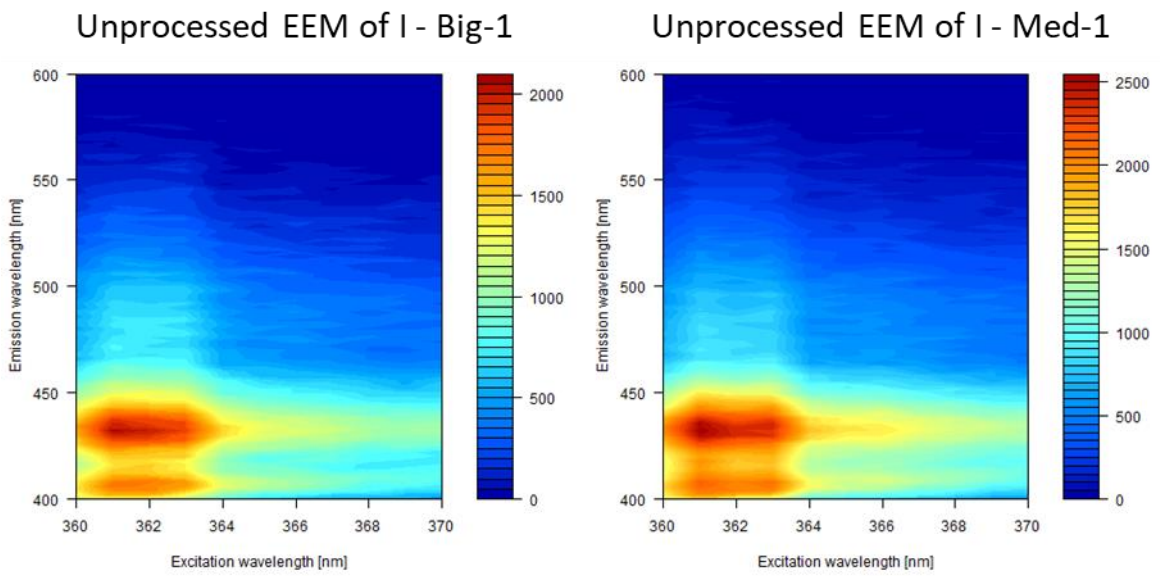

Figure 4.8: Unprocessed Excitation and Emission Matrices (EEM) of the fluorescence measurements of sample I – Big-1 and I – Med-1. Both of which are inoculated samples. Note that the colour scales have different ranges.

of 514.26 µg to 705.45 µg, the samples with the medium sized grains have an estimated biomass of 343.31 µg to 642.52 µg. The estimated biomasses of the blank samples are from 449.24 µg to 744.37 µg and 424.97 µg to 503.08 µg respectively. The overall largest estimated biomass was in

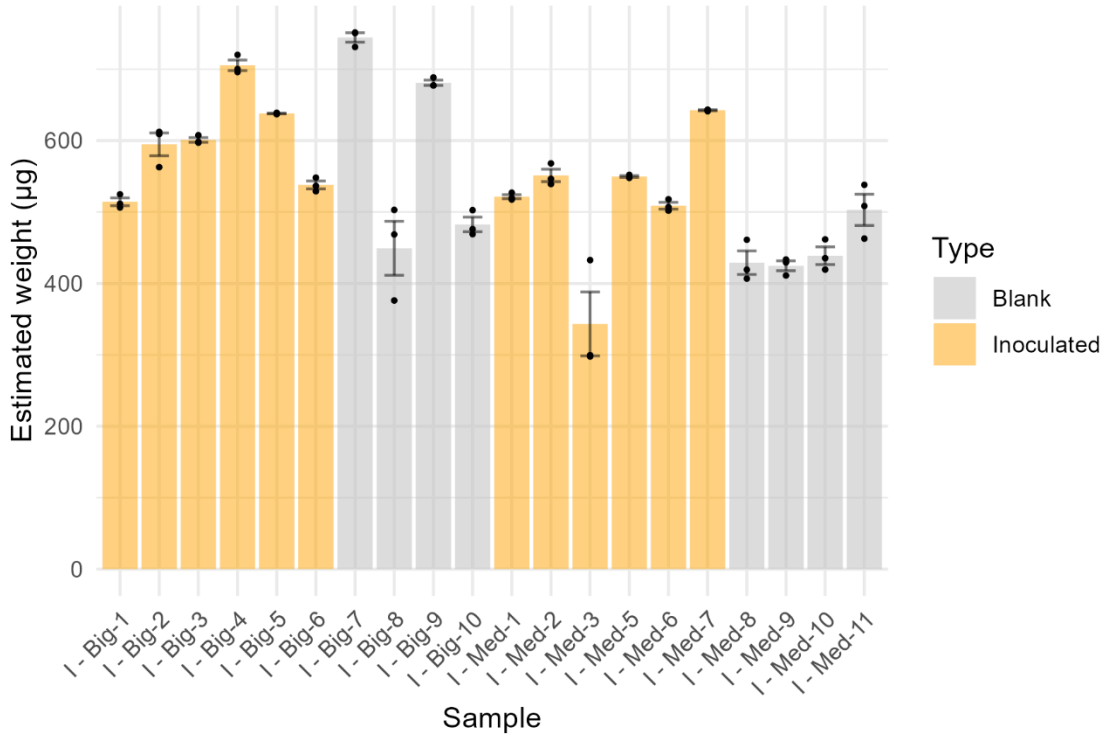

Figure 4.9: Bar plot of the mean estimated fungal biomasses of the syringe pump experiments in µg. The colours indicate if it was an inoculated sample (orange) or a blank sample (grey). The whiskers on each plot show the standard deviation of the respective sample. The black dots are each measurement individually.

B – Big-7, which is a blank sample, with 744.3 µg. The overall smallest estimated biomass was in sample I – Med-3, an inoculated sample, with 343.31 µg.

The standard deviation ranges of the biomass estimates for the triplicates are very similar for both experiments. For the samples with the large grain size, the range is from 0.81 µg to 53.58 µg, while for the medium grain size samples it ranges from 0.94 to 63.18 µg (see Table 4.8). The means of the biomass estimations of the triplicates and the standard deviations are visualized in a bar plot in Figure 4.9 as bars and whiskers respectively.

Table 4.8: Mean and standard deviation of the estimated biomasses of the triplicates based on the 10 % lennox broth model of the samples from the syringe pump experiments. The biomass is given in µg. The I in the sample ID stand for inoculated samples, the B for blank samples, Big for grain sizes (4-2 mm) and Med for grain sizes (1-2 mm).

Sample	**Mean of the estimated biomass in µg**	**Standard Deviation of the estimated biomass in µg**
I - Big-1	514.26	7.78
I - Big-2	594.76	22.58
I - Big-3	600.98	4.66
I - Big-4	705.45	10.52
I - Big-5	637.99	0.81
I - Big-6	537.93	7.84
B - Big-7	744.37	9.37
B - Big-8	449.24	53.58
B - Big-9	681.02	5.24
B - Big-10	482.57	14.47
I - Med-1	521.48	4.07
I - Med-2	551.21	12.31
I - Med-3	343.31	63.18
I - Med-5	549.82	1.76
I - Med-6	508.90	6.67
I - Med-7	642.52	0.94
B - Med-8	429.03	23.27
B - Med-9	424.67	9.72
B - Med-10	438.83	17.43
B - Med-11	503.08	30.96

4.2.2 SEM Imaging

One sample from syringe pump experiment 4 was prepared for SEM imaging. The syringe pump experiment 4 was conducted on medium sized grains (1-2 mm) and with 10% LB in seawater. The hyphae are flat and twisted and exhibit a rough texture with scattered granular structures. Branching and interpreted anastomosis, typical fungal features (see section 2.2.2), are highlighted with arrows in Figure 4.10 A.

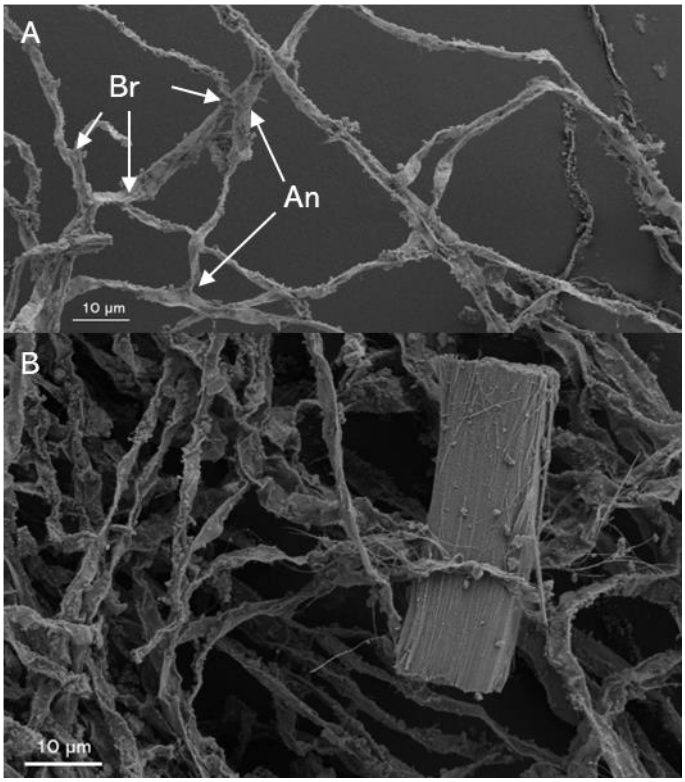

Figure 4.10: Scanning Electron Microscopy Images of fungal hyphae grown on 10 % lennox broth during the syringe pump experiment 4 on 1-2 mm big grains. A: Hyphae with typical fungal features like branching (Br) and likely anastomosis (An). B: Fungal mycelium in association with a fibrous mineral.

The fungi investigated with the SEM were mostly found as unattached pieces of mycelia. Sporadic fibrous minerals were found within the mycelia in association with the hyphae. One example of this is shown in Figure 4.10 B.

Because of the amount of material in the prepared sample, a subsample was taken for the SEM analysis. Only in one instance were hyphae attached to a grain found in this investigated subsample. These hyphae are shown in Figure 4.11. Figure 4.11 B displays a close-up of the white box in Figure 4.11 A, in which hyphae exhibit branching and anastomosis.

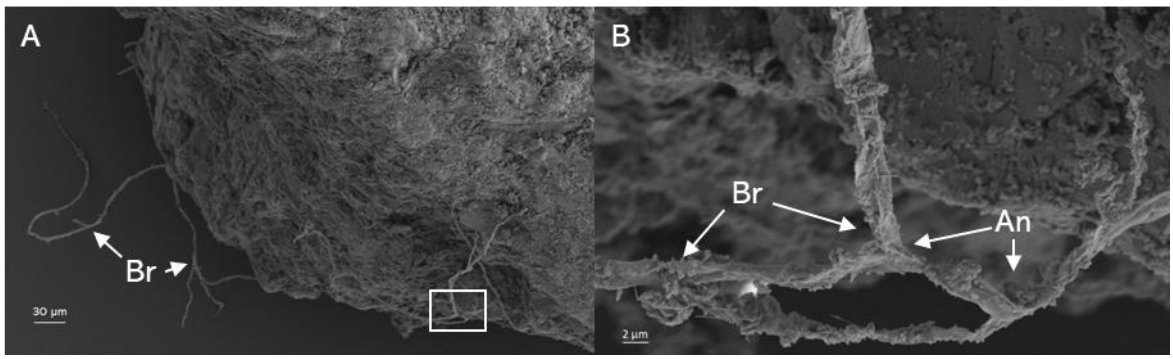

Figure 4.11: Scanning electron microscopy images showing fungal hyphae attached to a rock grain from the 4th syringe pump experiment. A: Overview of the hyphae and the rock grain. B: Close-up image of the area marked with a white box in A. Br: branching, An: anastomosis.

4.3 Permeability Experiments

Four permeability experiments were conducted of which 3 were inoculated and one was blank. One inoculated experiment was at 70 bar, which lasted two weeks and the other experiments were executed at 2 bar for three weeks each. Two of the 2 bar experiments were inoculated and the last one was blank.

4.3.1 Fluorescent Analysis

Five samples of the inoculated experiments were analysed with autofluorescence measurements. Of the experiment at 70 bar one sample (from the lower experimental Teflon sleeve) was analysed. For each of the two inoculated experiments at 2 bar the samples from both the lower and upper experimental Teflon sleeves (designated as 'lower' and 'upper' respectively) were analysed. The EEMs of these samples show a pronounced area of high intensity at emission wavelength of 400-450 nm and excitation wavelength of 360-364 nm (see Figure 4.12).

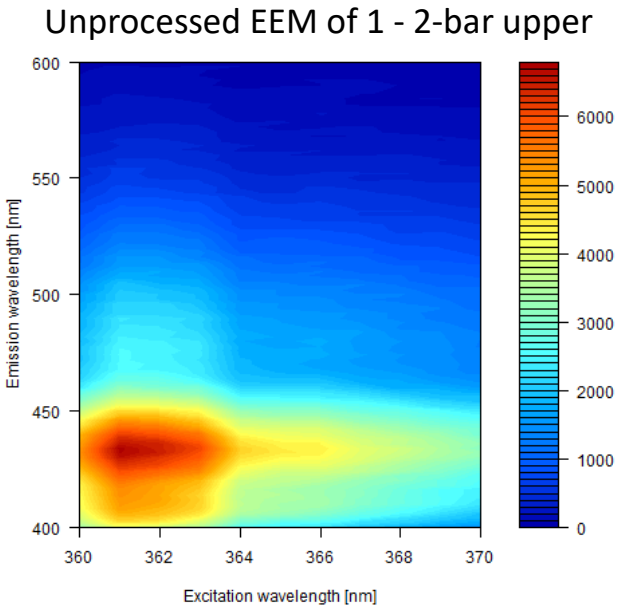

Figure 4.12: Unprocessed excitation and emission matrix (EEM) of the first 2 bar experiment of the upper experimental Teflon sleeve

Table 4.9: The mean of the estimated fungal biomass of the permeability experiment in µg and the standard deviation of the triplicates. The estimations are based on the 10 % lennox broth in artificial seawater model.

Sample	**Mean of the estimated biomass in µg**	**Standard Deviation of the estimated biomass in µg**
70-bar	774.57	15.65
1 - 2-bar upper	947.65	10.12
1 - 2-bar lower	963.53	8.43
2 -2-bar upper	888.56	18.06
2 - 2-bar lower	868.00	6.68

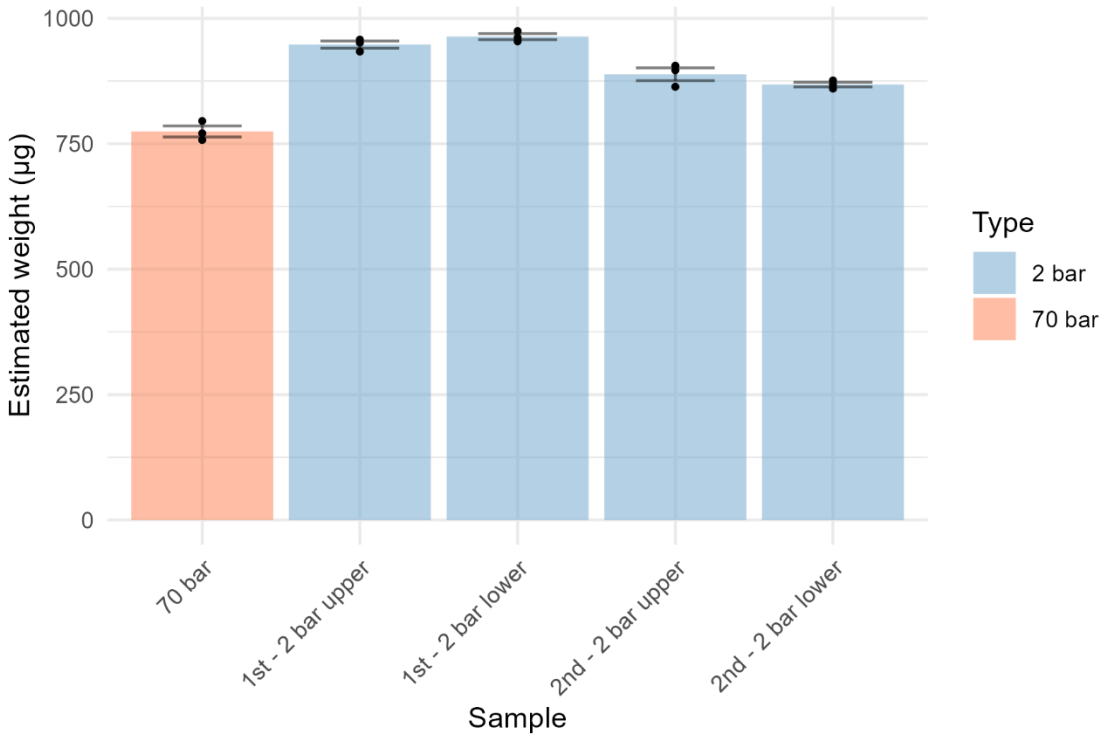

Figure 4.13: Bar plot of the means of the estimated fungal biomass of the permeability experiments. The means are based on the triplicate measurements. The whiskers show the standard deviation. The estimations are based on the 10 % lennox broth in artificial seawater model.

The fungal biomass estimations were obtained using the 10 % LB in ASW model, since this medium was used during the experiments. Of each sample triplicates were measured and the means and the standard deviations calculated. The biomass range for the experiments at 2 bar goes from 868 µg to 964 µg, which is significantly higher than the estimated biomass from the 70 bar experiment, which is 775 µg and with this outside of the standard deviations, which range from 6.7 µg to 18.1 µg (see Table 4.9 and Figure 4.13). The standard deviation is the highest for the experiment of the upper 2nd 2 bar experimental Teflon sleeve and the lowest for the lower 2nd 2 bar experimental Teflon sleeve.

4.3.2 Permeability Development

The permeability was calculated using Equation 2 (see section 3.1.2) for each point in time for all four permeability experiments. Occasionally the same pressure was measured at the inlet and the outlet point. Since this would lead to a division by 0 in the equation, these data points were removed. Subsequently, the permeability development was plotted with the time on the x-axis and the permeability in m² on the y-axis to visualize the permeability development.

The permeability in the first inoculated 2 bar experiment is very high and shows significant fluctuations between 1.2 x 10^{-13} m² and 6.2 x 10^{-14} m² during the first 16 days. These fluctuations cease with a steep drop of permeability to about 7 x 10^{-15} m². The permeability development is shown

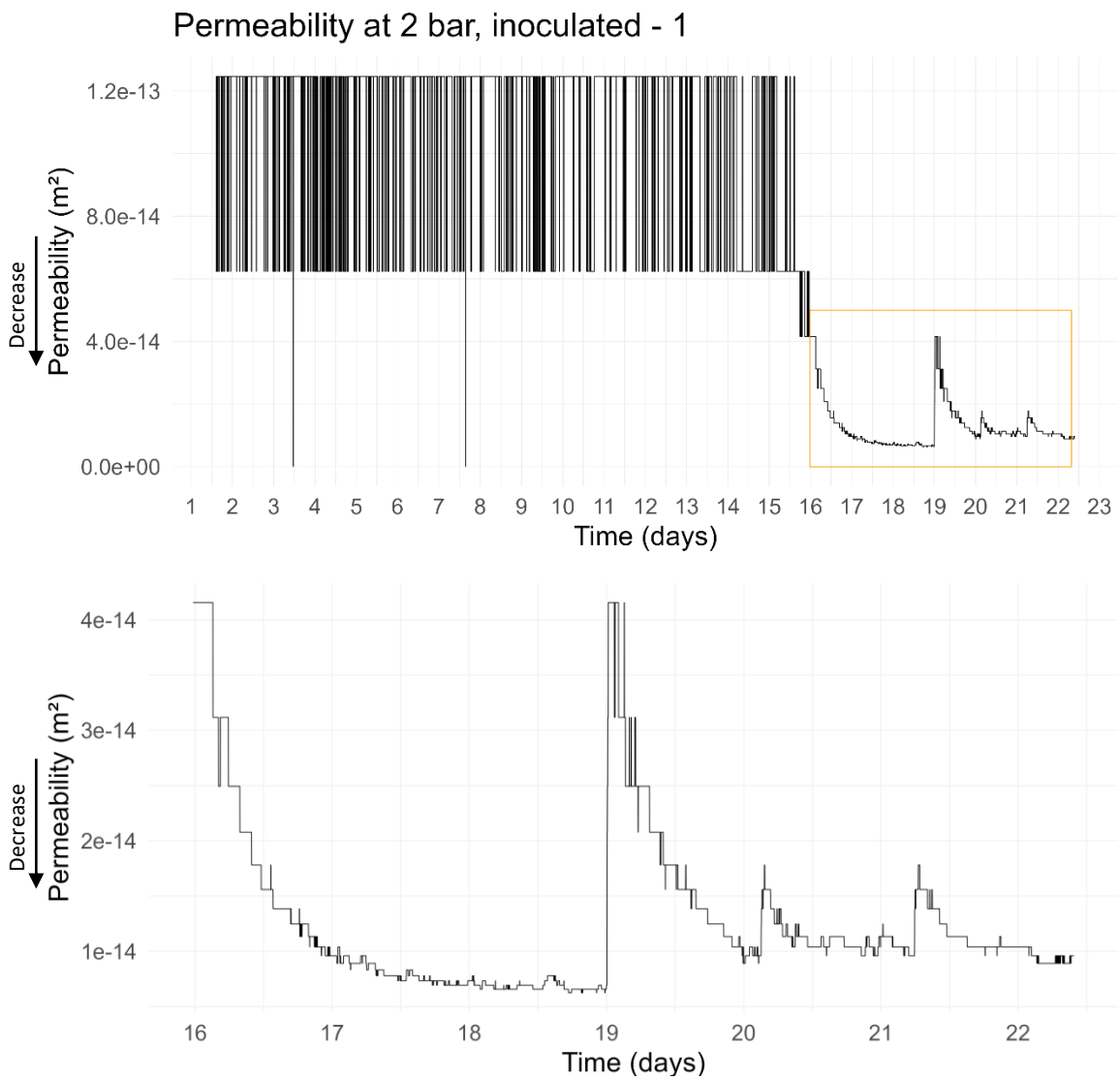

Figure 4.14: Permeability development over time of the 1st inoculated 2 bar permeability experiment. The lower plot shows the section within the orange box in the upper plot.

in Figure 4.14. The upper plot is the entire duration of the experiment starting from the stabilization at 2 bar after the pressure test. The lower plot scales up the section marked in an orange rectangle in the upper plot. It shows that there are still fluctuations in the permeability after the steep drop, however, these fluctuations are less pronounced and characterized by a steep increase in permeability and a more gradual decrease afterwards.

In the second inoculated permeability experiment are the same strong fluctuations of the permeability as in the first inoculated 2 bar experiment. The permeability fluctuates between 1.2×10^{-13} m² and 6.2×10^{-14} m² at the beginning. However, in this experiment these fluctuations last for 3 days before a steep drop in permeability to roughly 2.9×10^{-15} m² ends these pronounced fluctuations. The permeability development is visualized in Figure 4.15. The lower plot within Figure 4.15 shows the section marked in an orange box in the upper plot. In these last 18 days of the experiment, the pattern observed in the first 2 bar experiment is repeated with steep increases in

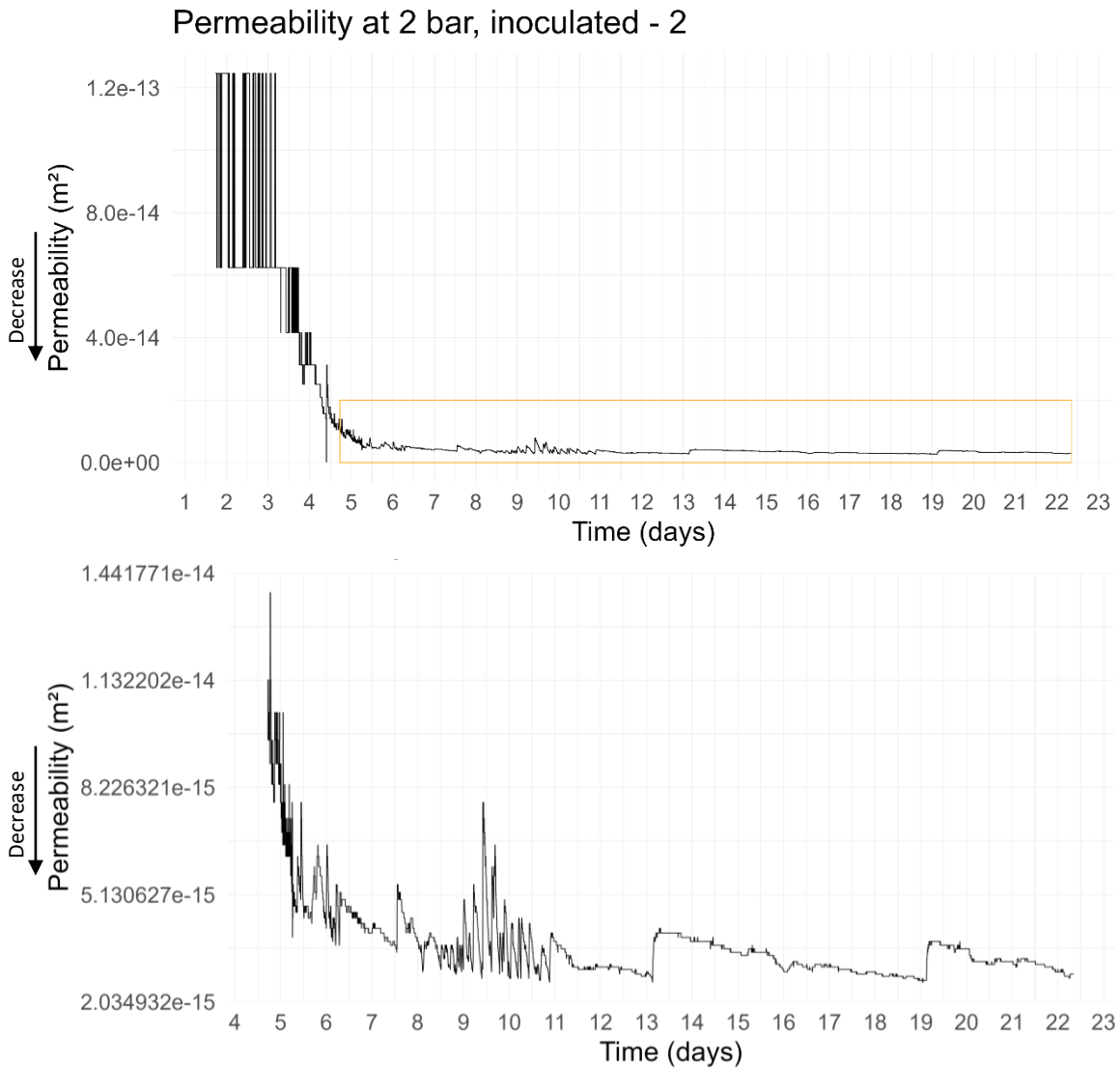

Figure 4.15: Permeability development over time of the 2nd inoculated 2 bar permeability experiment. The lower plot shows the section highlighted in an orange rectangle in the upper plot.

permeability followed by gradual decreases afterwards. But also more pronounced, steep fluctuations occur in this time frame, especially between the 8th and 11th day. These abrupt increases and decreases in permeability were not observed in the time of decreased permeability in the first inoculated 2 bar experiment.

The 70 bar experiment was the first permeability experiment conducted and was two weeks long instead of three weeks. Strong fluctuations of the permeability occurred over the entire course of this experiment. The permeability development is shown in Figure 4.16.

In the beginning it is evident that the permeability is not only fluctuating strongly but also it is negative, i. e. the pressure at the outlet is higher than at the inlet. The fluctuation occurs between -1.2 x 10^{-13} m² and -6.2 x 10^{-14} m². This changes on the 5th day when there is a sudden strong increase in permeability and it starts to fluctuate between 1.2 x 10^{-13} m² and 6.2 x 10^{-14} m². After two days of these fluctuations, the permeability begins to decrease with strong, steep increases in

between. The decreasing tendency seems to level out at roughly 1.3 x 10^{-14} m². After about 3 days of the decreasing trend, this pattern changes to even more pronounced fluctuations. These fluctuations span the range of the initial positive and negative fluctuations. One day before the experiment was terminated, the permeability oscillates between higher and lower values than before (-1.2 x 10^{-12} m² and 1.2 x 10^{-12} m²) for a short period of time.

One blank experiment was executed at 2 bar. The permeability is subject to strong fluctuations between 1.9 x 10^{-13} m² and 9.4 x 10^{-14} m². This pattern remains the same throughout the entire course of this experiment. The permeability development of that experiment can be seen in Figure 4.17.

It needs to be pointed out that the fluctuations at the beginning of all inoculated experiments are between 1.2 x 10^{-13} m² and 6.2 x 10^{-14} m². The fluctuations of the blank experiment differs with fluctuations between 1.9 x 10^{-13} m² and 9.4 x 10^{-14} m².

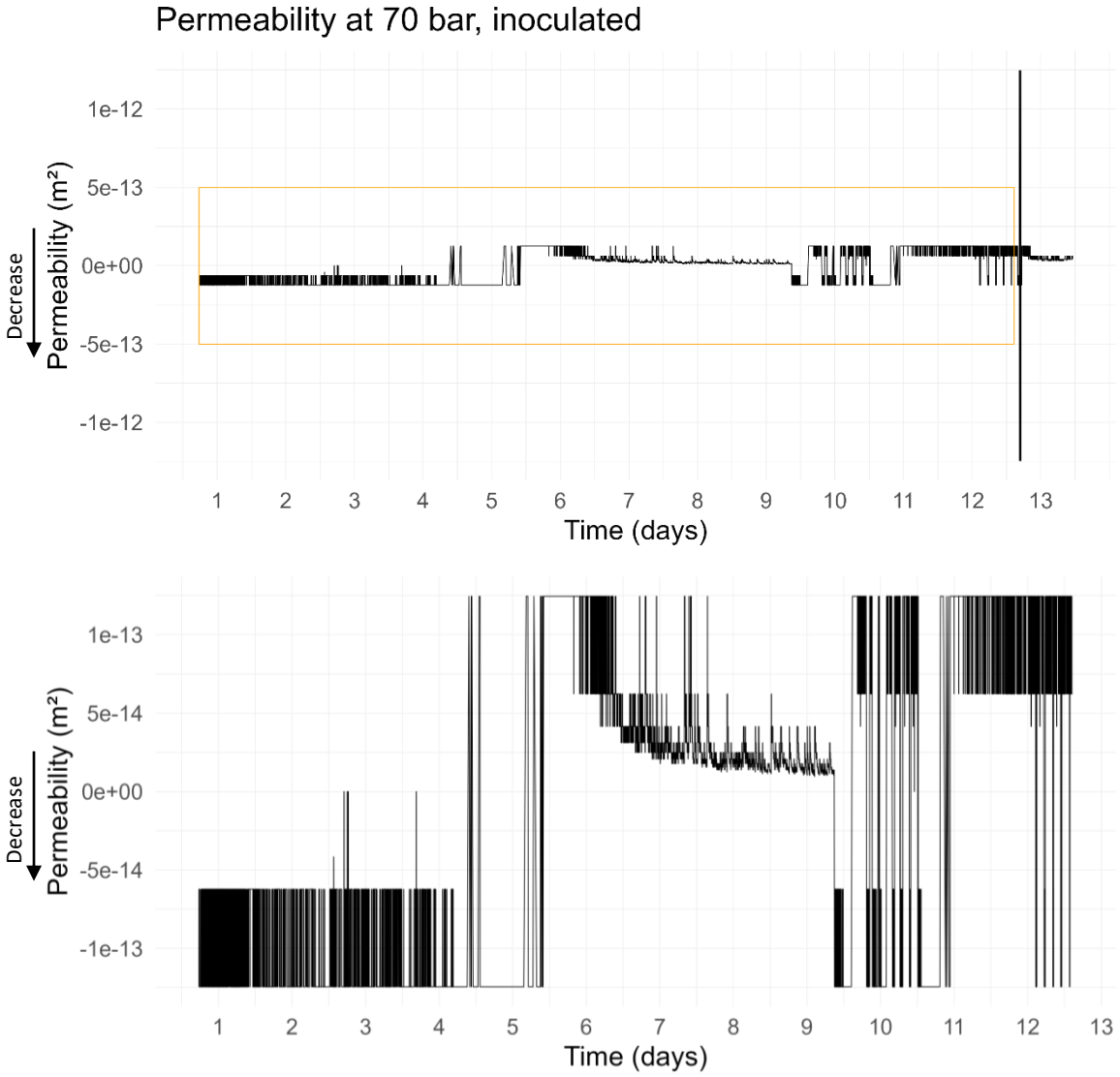

Figure 4.16: Permeability development over time of the 70 bar, inoculated permeability experiment, the lower plot shows the segment marked in an orange box in the upper plot.

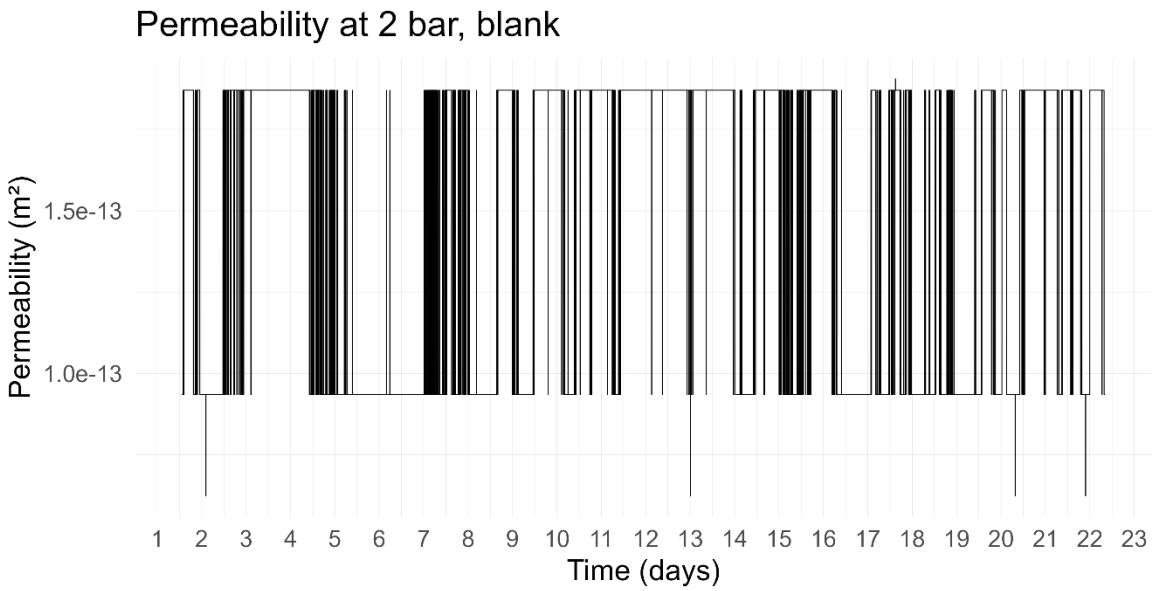

Figure 4.17: Permeability development over time for the blank experiment at 2 bar.

The pressure measurements uncertainty experiment was only successful at 2 bar with a flow rate of 0.1 ml/min. At 2 bar and with an empty reaction chamber the inlet pressure was almost constantly at 2 bar and the outlet pressure at 1.9 bar for 20 h, making the uncertainty 0.1 bar.

It was not possible to execute the uncertainty experiment for 70 bar at 0.1 ml/min because the pressure did not stabilize under these conditions.

4.3.3 SEM Imaging

SEM images were created for the inoculated permeability experiments for both 2 bar experiments and the 70 bar experiment. Similar to the hyphae that grew during the syringe pump experiments (see Figure 4.11) the hyphae observed in the samples of the permeability experiment are flat with a rough texture and occasional grains.

Using the SEM it was determined that the first and the second permeability experiments were contaminated with bacteria (see Figure 4.19 and Figure 4.18 A). This conclusion was drawn based on the presence of numerous orbicular and elliptical structured that were interpreted as bacteria because of their size and shape. Hypha were found as well, however, much rarer than the bacteria. The bacteria were often found in clusters as shown in Figure 4.19 B. Like in Figure 4.19 B these clusters would most commonly occur in protected cavities or indentations within the basalt grains. In some instances, the bacteria would form chains, which gave them a filamentous appearance (compare Figure 4.18 A).

Aside from bacteria, also fungal hyphae were found in the samples from the 2 bar experiments. The hypha had a collapsed appearance as it was observed in the syringe pump experiments as well (compare Figure 4.10, Figure 4.19 A and Figure 4.18 B). In the first permeability experiment a fungal

hypha was observed in close association with structures interpreted as bacteria based on their size and appearance (see Figure 4.19 A).

In the 70 bar experiment fungal hyphae forming a mycelium were observed. The mycelium was attached to the edge of a basalt grain and partly grew into an indentation within the grain (see Figure 4.20).

Bulbous structures were visible within the mycelium, connected to the hyphae. These structures can be classified into two distinct types: those with a smooth surface and those with a collapsed appearance (see Figure 4.21). After consultation with Magnus Ivarsson (Swedish Museum of Natural History) these structures are interpreted as fruiting bodies. The collapsed structures are fruiting bodies that have released the spores inside while the others have not yet released the spores and thus have not collapsed. These

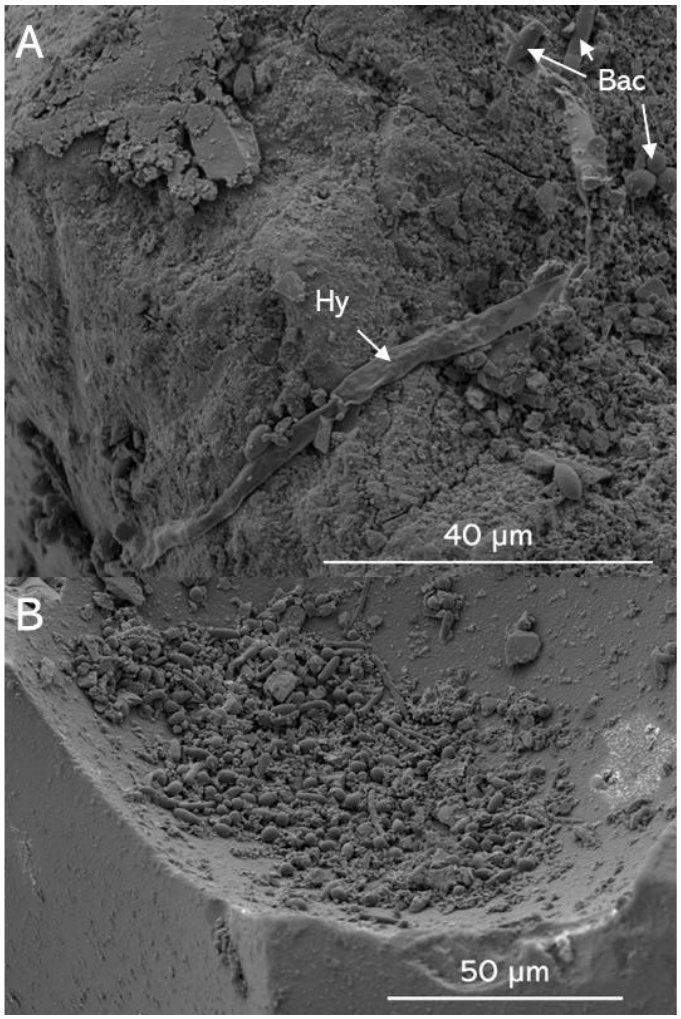

Figure 4.19: Scanning electron microscopy images of the first 2 bar permeability experiment. A Fungal hypha in association with bacteria. B: bacterial consortium on a basalt grain. Hy: Hypha, Bac: Bacteria

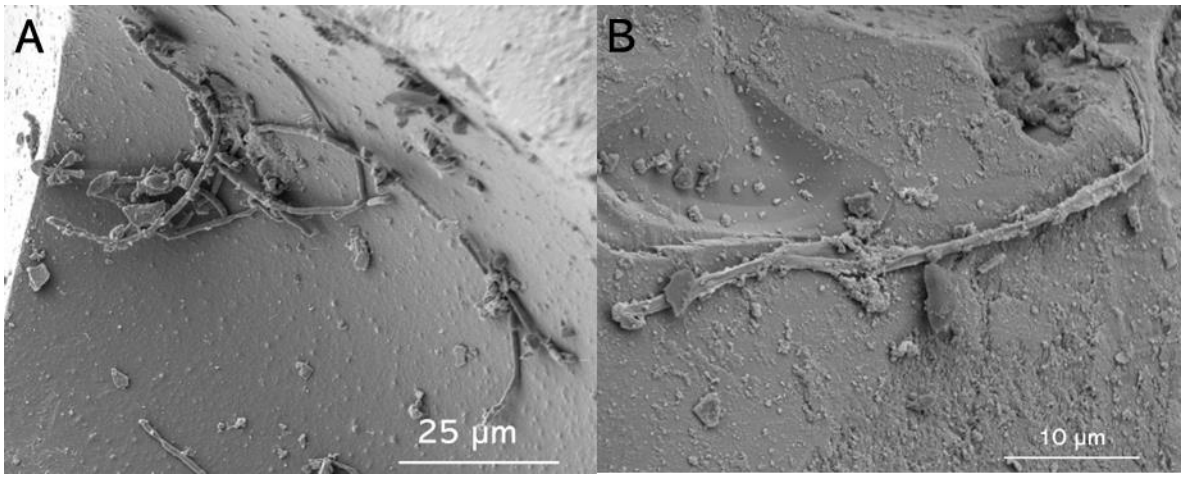

Figure 4.18: Scanning electron microscopy images of the second 2 bar permeability experiment. A: Filamentous bacteria, B: Fungal hypha.

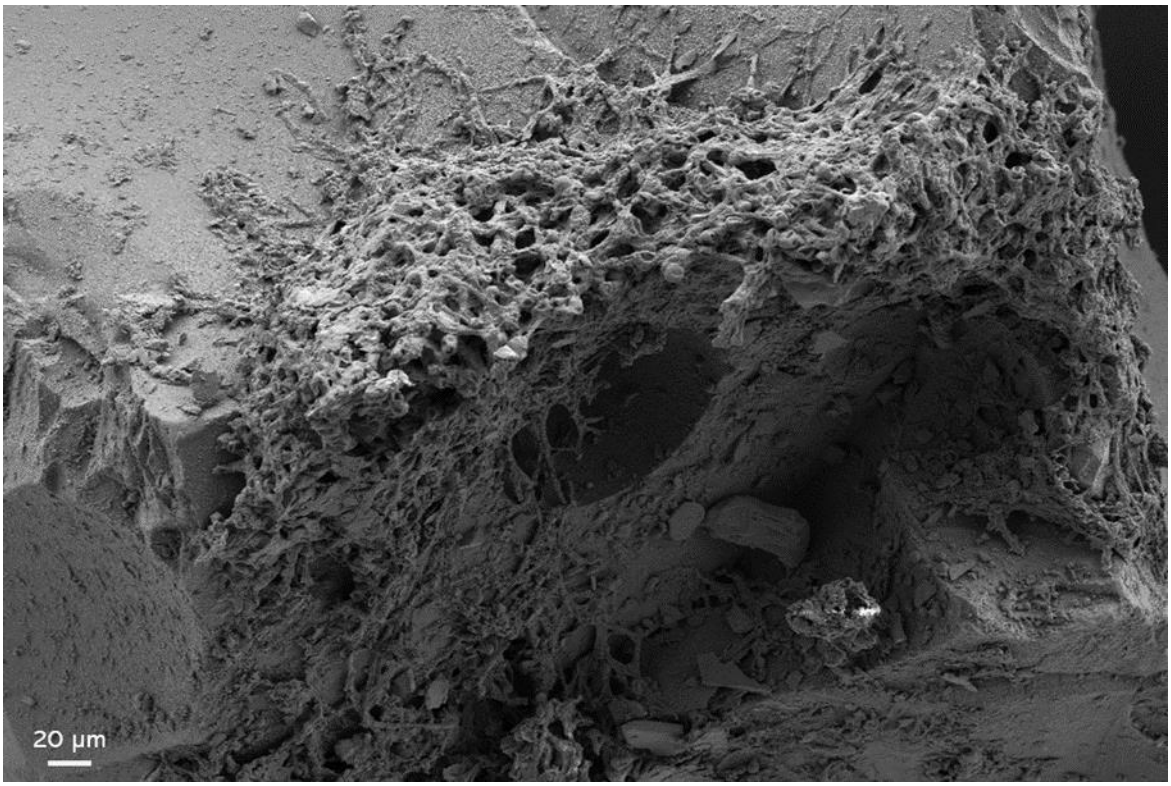

Figure 4.20: Scanning electron microscopy image of fungal mycelia grown during the inoculated 70 bar permeability experiment on a basalt grain.

structures appear mostly at the end or at junctions of hyphae (see Figure 4.20), which supports the interpretation as fruiting bodies. However, it cannot be ruled out that the structures with the smooth surface are yeast cells or bacteria. However, aside from this, no evidence for bacterial contamination was found during the SEM investigation of the samples from the 70 bar experiment.

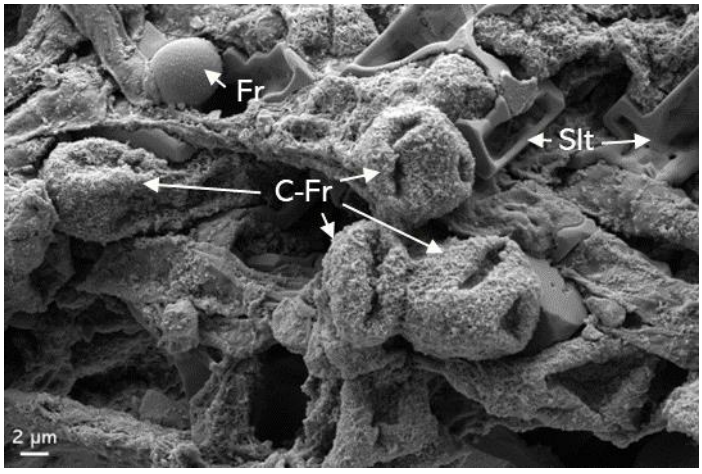

Figure 4.21: Scanning electron microscopy image of fungal mycelia grown during the inoculated 70 bar permeability experiments with bulbous structures interpreted as fruiting bodies. Fr: Fruiting body, C-Fr: collapsed fruiting body, Slt: Salt crystal.

5 Discussion

5.1 Biomass Analysis

One of the main objectives of this study was to find a method to estimate fungal biomass in experimental settings and compare the amount of biomass developed to the permeability decrease. To achieve this, two different methods were tested for the investigation of fungal growth in experimental settings. Both were tested on the syringe pump experiments and one was used to estimate the biomass of the permeability experiments. Both methods have advantages as well as disadvantages which will be discussed below.

5.1.1 Method Applicability

For pragmatical reasons low fungal biomasses (20-1050 µg) were used in this study. This decision was made because of the short duration of the experiments (2-3 weeks) due to the limited time that the flow-through autoclave was available for this study. It was expected that during this time only low amounts of biomass would be developed in the experiments, which is the reason why the biomass analysis methods were also tested and/or based on small amounts of biomass. This low amount of biomass most likely had an influence on the reliability of the results because of the uncertainty of the scale. This is shown, for example, by the validation experiment for the LOI method, in which fungal biomass was added to crucibles and weighed before and after drying. After drying, some of the crucibles were lighter or weighed the same as before, even though biomass had been added (compare section 4.1.1). The most likely reason is that the precision of the scale was not sufficient to detect the small change in weight that the low amount of biomass caused. An internal test has shown that the scale used for the LOI experiment has a deviation of 0.1 % for a sample with a weight of 2 g.

Subsequent to the weighing of the crucibles with the dried biomass samples, the fungi were burned without being covered by dunite grains. However, not the entire biomass weight was lost (see Figure 4.3). Since it is not very likely that the fungal biomass can withstand 550 °C for one hour, this can most likely also be ascribed to the weighing precision. This finding could potentially be transferred to the measurements of the fungal biomasses used for the PLS model building. Which could mean that the models are potentially inaccurate because they are based on inaccurate biomass measurements. However, it should be noted that the LOI samples and the samples used in the autofluorescence method were measured with two different scales. It cannot be excluded that the scales had different precisions and accuracies.

The LOI test experiment also demonstrated that the dunite grains that were used are not ideal for the LOI method. The LOI of the fungi covered with grains was significantly higher than the biomass amount of fungi that had been added to the grains (see Figure 4.3). This suggests that a

predominant amount of the LOI must be caused by the dunite grains themselves. It was shown before, that the Leka dunites have their own inherent LOI. of 6.90 – 11.80 weight percent (see Table 3.4 and IYER et al., 2008). These numbers were not known before the experiments.

The LOI results of the syringe pump experiments show the same trend. The second syringe pump experiment, whose grains were burned before the experiment, shows a much lower LOI than the samples from the first syringe pump experiment (see Figure 4.1). This leads to the conclusion that some of the dunites own LOI was lost during the pre-experimental burning.

Another important observation is that even though the dunite grains were burned before the experiment, there is no significant difference between the blank samples and the inoculated ones. A reason for this could be the duration of the burning. Following an internal protocol the samples were burned for one hour. Other studies (e. g. WRIGHT et al., 2008, HOOGSTEEN et al., 2015) have burned samples at the same temperature for 3-4 h. This could mean that the LOI was not completed at the end of the burning period. This could be true for the burning of the dunites before the experiment as well as after.

The incomplete LOI is further underlined by the strong dependency of the LOI on the position of the samples in the oven. When the LOI is plotted against the position of the samples relative to the side walls, the samples are arranged in the shape of a bow, i. e. the further the samples are away from the wall, the more LOI occurred (see Figure 4.2). This is observable independently of whether the dunites were burned before the experiment or not. If the LOI of the samples is plotted against the position of the samples relative to the door, the arrangement of the samples portrays no clear pattern. However, this could be an artifact of the sample number. The samples were placed at the back of the oven in two or three rows with 6 to 7 samples in each row. 2 to 3 rows are not enough to determine the structure of the LOI occurrence.

The presence of the bow pattern in the sample arrangement within the positional plot of the second syringe pump experiment is another reason to assume that the LOI was not completed, as these grains were burned before the experiment. This means that there was still sufficient material that could be burned off as the biomass alone cannot be responsible for this high amount of LOI (10.9-63.5 g/kg). Additionally, the blank samples are part of the bow as well even though they should not have any LOI at all.

This leads to the conclusion, that the LOI is an inappropriate approach to determine the biomass reliably using this amount of biomass and these dunites. In the future it could be tested to increase the burning duration before the experiments as well as after to ensure a completion of the LOI. If the dunite grains were sufficiently burned before the experiment and if the biomass is in an amount high enough to be weighed reliably this method can be applied to any kind of fungal sample regardless of species or clade. This would be a very important advantage compared to the fluorescence analysis.

For the fluorescence analysis the approach suggested by MANSOLDO et al. (2020) was followed. In their study they focused on the cell-membrane component ergosterol. The reason why ergosterol was chosen is because ergosterol is generally seen as a fungi-typical biomarker (WEETE et al., 2010). However, it has been determined that there is an ergosterol content range of 2.6 to 42 µg/ml of dry mass between fungal species (PASANEN et al., 1999). Additionally, ergosterol does not occur in all fungi (WEETE et al., 2010). It is especially common in later diverging fungi in which it usually is the dominant sterol. This represents a major limitation to the fluorescence model, which in turn can be created to determine the biomass accurately of only one specific species. In this study *P. rubens* was used, which is known to produce ergosterol (MONTGOMERY et al., 2000). However, the growth medium was found to have an influence on ergosterol content as well (CHARCOSSET & CHAUVE., 2001, NEWELL et al., 1987). That is why, PLS models for *P. rubens* grown on different media and different media percentages were grown to evaluate the influence of growth substrate to the model. The results are compared to the results from MANSOLDO et al. (2020).

The EEMs measured in this study have high intensity areas in the emission wavelength ranges of 400-450 nm, which is in contrast to the EEM of an ergosterol standard, that depicts one band of high intensity at emission wavelengths of 450-525 nm and the entire excitation wavelength range (see Figure 5.1, MANSOLDO et al., 2020).

A PCA conducted on the fluorescent measurements of different dilutions of the ergosterol standard shows three areas of high loadings in the PC1 at the excitation wavelengths of 360-362 nm, 365 nm and 370 nm and at the emission wavelength range of 450-525 nm (see Figure 5.1, MANSOLDO et al., 2020). Particularly low intensities are at excitation wavelengths 360-369 nm and emission wavelengths of 400-450 nm. These regions of high loadings are of importance for the ergosterol concentration and the negative peaks have an inversed relationship to the concentration compared to the positive peaks.

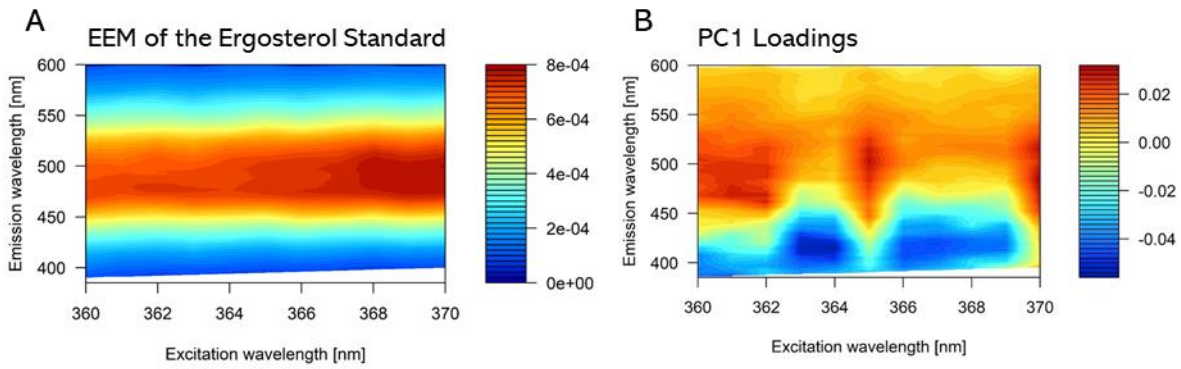

Figure 5.1: Fluorescent data of the ergosterol standard from MANSOLDO et al. (2020), A: The excitation and emission matrix (EEM) of the ergosterol standard, B: Loadings plot of the principle component 1 (PC1) of the principle component analysis of the ergosterol standard fluorescent measurements at different dilutions. Note that the colour scales have different ranges.

The area of the negative intensities of the PC1 of the ergosterol concentrations overlaps with the areas of high intensities of the PC1 of the fungal samples in this study (compare Figure 4.5 and Figure 5.1), even though the shapes of the areas differ. One reason for this inversed trend could be differences in the experimental or analytical procedures. For example, in this study increments of 2 nm were used for the fluorescence measurements, while in MANSOLDO et al. (2020) increments of 1 nm were used to measure the fluorescence of the ergosterol dilution series. This gives the EEMs of the ergosterol a higher resolution, which could have caused these differences. Another reason could be that the principal components capture different dominant sources of variation between the ergosterol standard and the fungal samples. Possible is, that the extract of the fungal samples contains no or not only ergosterol, i. e. it cannot be excluded that the extraction of the fungal samples with the polar solvent ethanol resulted in other components going into the solution as well. These components could be responsible for the PC1 loadings either due to the absence of ergosterol or the interference with the fluorescence of ergosterol.

This interference of the fluorescence pattern is possible because fungi contain other fluorophores aside from ergosterol. Some of them are flavins, NAD(P)H, melanin, amino acids and carotenoids (KNAUS et al., 2013 and references therein, CROCE, 2021 and references therein, FEDOSEEVA et a., 2022). However, they have different excitation and emission wavelength ranges. For example, flavins have excitation wavelength ranges of 360/445 nm and emission wavelength ranges of 480/540 nm and NAD(P)H has excitation wavelength ranges of 330-380 nm and emission wavelength ranges of 440-480 nm (CROCE, 2021 and references therein). Most of the ranges of other fungal fluorophores lie outside of what was measured in this study. FEDOSEEVA et al. (2022) found that most fungal autofluorescence is emitted by amino acids, melanin-like compounds, NAD(P)H and flavins. In future experiments it would be reasonable to increase the emission and excitation wavelength ranges to get a broader spectrum of fungal fluorophores. On the one hand it could increase the robustness of the model, on the other hand it could also lead to overfitting and multicollinearity resulting from a more complex model. Additionally, this would increase the measurement time as well. The measurements of the samples used to create one model was roughly 9.5 h (for 96 samples at a time). If more excitation and emission wavelengths would be measured this time would increase as well. Alternatively, an analysis of the extracted compounds could be conducted, e. g. using gas chromatography coupled with mass spectroscopy. Knowing the components within the extract would facilitate the identification of important fluorophores within *P. rubens* related to the fungal biomass.

To assess the performance of the model, six statistical metrics were calculated. Two of the statistical metrics used to evaluate the model were R^2CV and R^2P. R^2 is a measure of proportion of the variance in the dependent variable during cross-validation (R^2CV) or with new data (R^2P). The closer the number is to 1, the more precise is the model. RMSECV and RMSEP were used as well. These are

the squared roots of the mean differences between the predicted values of the dependent variable and the actual values of the cross-validation (CV) or the new data (P). This means that the lower this number is, the better is the model. The last statistical metrics are RPDCV and RPDP which are the ratios of the standard deviation of the response variable to the standard deviation of the residuals (difference between the predicted value and the actual value) in the cross-validation or the new data. The higher the value of these statistics, the better is the model.

One way to categorize the models is a model classification based on the RPDCV values (CIPULLO et al., 2019), in which different ranges correspond to levels of performance: excellent = > 2.5, very good = 2.5-2, good = 2.0–1.8, fair = 1.8-1.4, poor = 1.4-1.0, very poor = < 1.0. Following this, the models created in this study have a range from poor (100 % PG model) to excellent (e. g. 1 % PG model). For a comparison, the model created by MANSOLDO et al. (2020) is excellent according to this classification. Overall, are the statistical metrics of the model by MANSOLDO et al. (2020) better than those achieved for the models created in this study (compare Table 4.3). On reason for the better performance could be that MANSOLDO et al. (2020) used the fungus *Schizophyllum commune* to create the model. This fungal species might have a different fluorophore composition and thus possibly be better suited to carry out the fluorescence analysis. Another reason could be that in MANSOLDO et al. (2020) 0.1-1 g of fungal biomass were used to create the PLS model. It is possible that the low amount of fungal biomass used in this study resulted in low concentration of ergosterol or other fluorophores within the extract, which could have caused issues in the fluorescence measurements. Alternatively, the above-mentioned limitations in the scale precision could have restrained the accuracy of the model. Furthermore, it is possible that the differences in model optimization step led to these different results (compare section 3.3.2.2.5). While in this model a loop was created to find the best VIP cut-off value, in MANSOLDO et al. (2020) stepwise backward selection was used to find the variables used for the optimized model.

The optimization step in MANSOLDO et al. (2020) led to an overall improvement of the statistical metrics. However, if the statistics of the optimized models from this study are compared to the first models (Table 4.2) then it stands out that especially the metrics for the cross-validation are improved. This suggests that the optimization step did not lead to a general improvement of the model but rather to an overfitting of the model to the trainings data set. This observation is underlined by the test experiments for the 10 % LB and the 10 % LB in ASW models that led in both cases to poor results (see 4.1.2.2 and Table 4.6) as well as the estimation of the biomasses within ethanol measurements (see Table 4.7). It should be noted that in MANSOLDO et al. (2020) no such separate validation experiments were conducted.

One difference between the optimized models of this study and the one by MANSOLDO et al. (2020) is that the optimized model by MANSOLDO et al. (2020) is based on 54 variables, which is much less than what the optimized models in this study are built with (114-1080, Table 4.1). These 54 variables are clustered in five distinct groups, which are visible in Figure 5.2. One of these groups

is at emission wavelengths < 400 nm. This emission wavelength range was not measured in this study. However, compared to the VIP values of the 10 % LB in ASW model (Figure 4.6) and the used variables in the optimized models (Appendix 4) the trend of the emission wavelengths between 400 and 450 nm being of importance as well as emission wavelengths between 500 and 550 nm being of less pronounced importance is visible in Figure 5.2 as well.

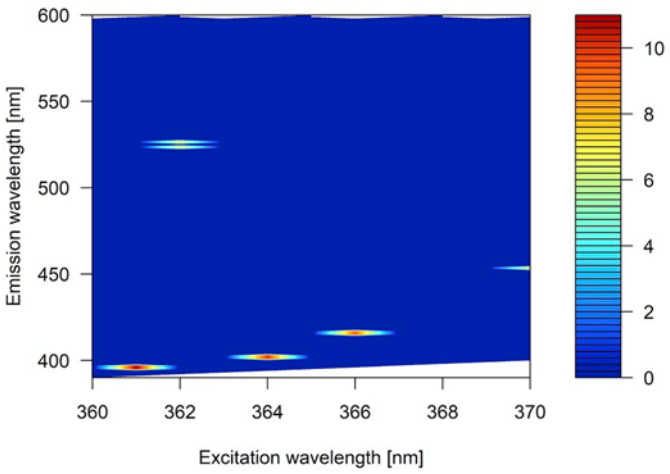

Figure 5.2: Contour plot of the variable importance in projection values of the optimized model of MANSOLDO et al. (2020).

However, in this study the optimized models are based on 114-1080 variables, which is a much higher amount than in MANSOLDO et al. (2020). If the VIP cut-off values and the number of variables used are compared between the optimized models of this study (see Table 4.1), then no pattern stands out. One reason for the great variation in the goodness of fit (Table 4.3) of the models between the culture media could be the culture media itself. It is possible that the media greatly influences the lipids, especially the amount of ergosterol that the fungi produce. Generally, PG seems to lead to a lower number of variables, which could mean that LB adds a certain amount of uncertainty and that more components within the medium results in a more complicated model.

Yet, this difference between the measurements is barely visible in the PC1 loadings (compare Figure 4.5). The plot loadings are all very similar, which suggests that the influence of the medium components and medium concentration is not significant. On the other hand, the score plot of a PCA conducted on all measurements undertaken for this study, shown in Figure 5.3, portrays a clear clustering of the different culture media of the model samples. This visualizes the relationship of the samples to each other. The clustering is especially evident for the 1 % medium solutions, that cluster tightly and are close next to each other. The measurements of the fungi grown on the 10 % medium solutions cluster close to each other as well with limited overlaps. However, in this case the clusters are more spread out. The samples for the 100 % PG model were measured on two separate days, which is visible in two distinct clusters. The PC1 portrays a strong influence of medium percentage With the only exceptions being the first measurement of the 100 % PG model and the samples that were extracted in association with grains. It is noteworthy that the blank measurements do not cluster but are spread across all samples.

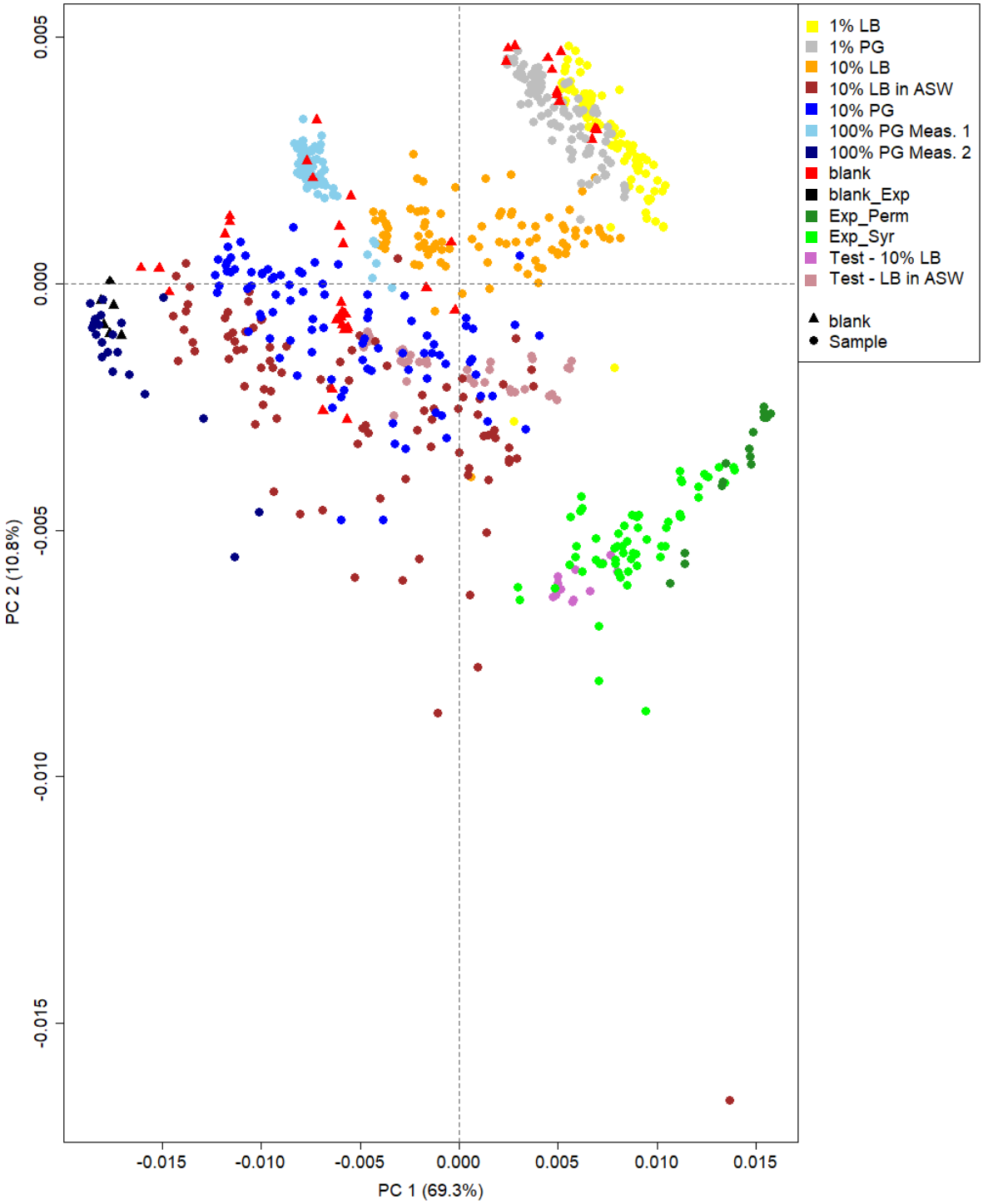

Figure 5.3: Principal components analysis score plot of all measurements conducted for this study. Samples are color-coded by use: culture medium (model building, PG = Potato glucose, LB = Lennox broth, ASW = Artificial seawater. Percentages of the media in seawater unless stated otherwise), Test (validation experiments), Exp_ (experiments), Perm (permeability experiments), Syr (syringe pump experiments), and blanks.

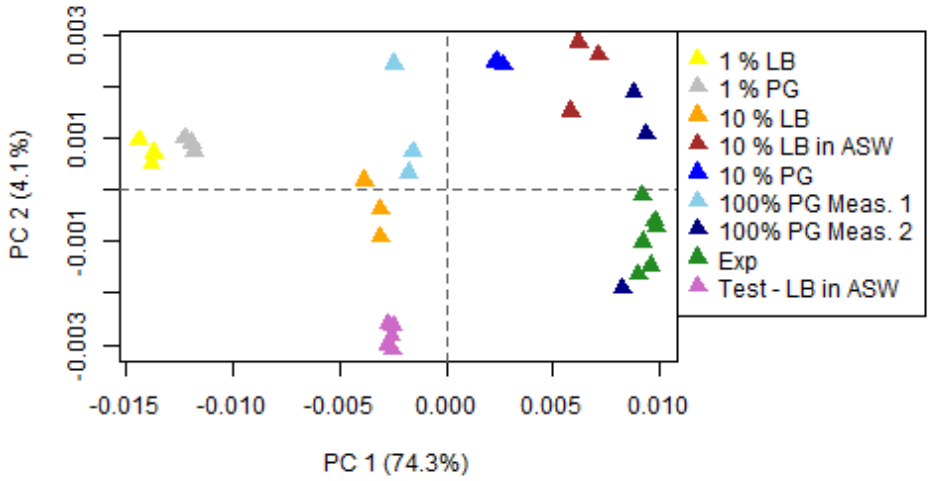

Figure 5.4: Principal component score plot of all pure ethanol measurements. The colours indicate to which purpose the ethanol measurements were conducted. The samples are colour coded: culture medium: model building (PG = Potato glucose, LB = Lennox broth, ASW = Artificial seawater. Percentages of the media in seawater unless stated otherwise), Test: validation experiment, Exp: experiments).

The samples that were extracted in association with basalt or dunite grains (the permeability and syringe pump experiments as well as the validation experiment for 10 % LB) all cluster together and are separate from the other samples. To ensure that this is not the result of a day variability the ethanol measurements conducted with these samples were marked separately as blank_Exp in black. These measurements cluster with the 100 % PG measurements of the second day, which suggests that this is not the result of a measurement run variability.

Nonetheless, precision seems to be a problem. To emphasize this, all ethanol measurements conducted throughout this study are shown in a score plot in Figure 5.4. The PCA was conducted on only the shown ethanol measurements, which were mean-centered to each other during the preprocessing. In this plot a measurement run-dependent clustering is visible as This shows that there are slight differences in the measurements depending on the run.

It is also noteworthy that in Figure 5.3 the samples of the validation experiment for the 10 % LB in ASW model cluster close to the samples measured for the model building of the 10 % LB in ASW model but the overlap is just minimal. This is another argument for between-run variability in the measurements as these fungi were grown, extracted and measured under the same conditions.

In the validation experiment results (Figure 4.7, Table 4.4, Table 4.5, Table 4.6 and Table 4.7) it is evident that the models are not reliable with new data. Especially the validation experiment for the 10 % LB model, that included the dunite grains, resulted in biomasses very different to the actual biomasses. However, it should be kept in mind that the low number of samples in that experiment might have influenced these poor results. Another problem with that validation experiment was that much more biomass was used for the validation experiment than for the model building.

In summary, the fluorescence method proofs to have major limitations in accuracy and precision. The results of the models should be interpreted with caution as over- and underestimation of biomass could be the case, as it was in the validation experiments. Generally, a sense of relative biomasses of the same measurement batch can be obtained and in the future higher biomass amounts should be used to create the models to test the applicability of them further.

5.1.2 Biomass Estimations of the Experimental Samples

The biomasses of the experiments were estimated by the fluorescence analysis method and using the 10 % LB model for the syringe pump experiments 3 and 4 and 10 % LB in ASW for the permeability experiments. The estimations resulting from this analysis are discussed below. For the syringe pump experiments only the results of the fluorescence analysis will be considered (experiments 3 and 4) and collectively referred to as syringe pump experiments. The syringe pump experiment 1 and 2 are disregarded.

Overall resulted the biomass estimations in the permeability experiments in higher amounts of fungal biomass (775-963 µg) than in the syringe pump experiments (450-750 µg) (see Table 4.8 and Table 4.9). One reason for this could be the higher flow rate in the permeability experiments (0.1 ml/min) compared to the syringe pump experiments (29.788 µl/h = 0.0005 ml/min). The higher flow rate during the permeability experiments led to a quicker delivery of nutrients, which could have resulted in a faster accumulation of biomass. Possible is also that the diluent of the medium is responsible for the different biomass amounts. Even though in both experiments 10 % LB was used, it was mixed with seawater in the syringe pump experiments but with ASW in the permeability experiments. Other variables that differed between the two experiments are the grain size (see Table 3.1 and section 3.2.3.2), the grain composition (see Table 3.4) and the volume of the experimental setting (7 ml in the vials of the syringe pump experiments and about 7.8 ml in the experimental Teflon sleeves of the permeability experiments). And while the influence of the grain sizes has been tested in the syringe pump experiments (see further down), the influence of the other variables were not separately examined.

Another reason for the differences in the biomass amounts between the two experiments could also be the models that were used to estimate the biomasses. As established above, the biomass estimations of the models portray flaws. One argument for the models to be the cause of the differences in biomass amounts is the lack in distinction between the estimated fungal biomasses of the blank samples and the respective inoculated samples in the syringe pump experiments (compare Figure 4.9). This would indicate that the blank samples were contaminated. However, during the transfer of the samples into the falcon tubes no fungal hyphae were observed. Additionally, in the samples from experiment 4 (medium grain sizes), a chunk of fungal mycelium was removed from

the needle of the inlet-syringe of every inoculated sample. This growth was not observed in the blank samples. That leads to the conclusion that it is unlikely that the blank experiments were contaminated.

The inaccuracies of the models could have additionally been promoted by the amount of biomass accumulated during the experiments. The estimated fungal biomasses for the syringe pump experiments are between 450 and 750 µg, while the highest biomass amount used to build the 10 % LB model was 640 µg (compare Table 3.5 and Table 4.8). The highest amount of biomass to build the 10 % LB in ASW model was 780 µg and resulted and estimated fungal biomasses between 775 and 963 µg in the permeability experiments (compare Table 3.5 and Table 4.9). This might have been a restriction to the accuracy and precision of the models in this biomass range considering that the estimated biomasses are higher than the biomasses the models were trained with.

In addition, two different models were used to estimate the fungal biomasses of the two different experiments. The two models show different levels of performance (see Table 4.3) with the model based on 10 % LB in ASW having an overall slightly better performance. This could also have been relevant for the differences in the biomass amounts between the two experiments. The range of standard deviation is much larger for the syringe pump experiments (0.81-63.18) than for the permeability experiments (6.68-18.06), which could be a result from different precisions of the models or it is a result of the differences in sample numbers (see Table 4.8 and Table 4.9). Overall, the standard deviations lie between 0.5 and 4 %, with a few outliers lower than 0.5 % and other up to 20 % which gives the models an overall good precision in estimation.

The presence of the basalt/dunite grains within the samples during the extraction process might have had an influence on the performance of the models as well. This was already mentioned in relation to the validation experiment of the 10 % LB model further up. The unprocessed EEMs of the samples from the experiments portray roughly the same points of high intensity as the pure fungal samples (compare Figure 4.8, Figure 4.12 and Figure 4.4) but in a different shape. While the fungal samples show a long, slim band, the high intensity areas in the experiment samples are a rectangle on the lower end of the excitation range with a peak at excitation wavelength of 361 nm and emission wavelength of 440 nm. This difference in intensity structure is in agreement to the clustering of these samples away from the model samples seen in the PC1 score plot (Figure 5.3). This shows that the grains have a noticeable influence on the fluorescence. The clustering of the experimental samples is close to each other and overlaps to a certain degree (shown in Figure 5.3), which means that the influence that the grains pose to the fluorescence measurements is independent of the composition of the material. Even though basalts and dunites can contain fluorescent minerals like fluorite (SIDIKE et al., 2003), calcite (YOSHIDA et al., 2010) or zircon (AOKI, 1984), it is unlikely that these minerals cause the difference in the EEM. This is because the solution is filtered after the extraction, which means that even though fine particles of these minerals could have been abraded during the sonication, they would likely have been larger than 0.2 µm and filtered out. Additionally, the

chemical compositions are different between the basalt and dunite (compare Table 3.4), which makes it unlikely that they have influenced the fluorescence in such a similar way.

The influence of the grains could also be explained by the fungus changing its cell-membrane structure and composition when grown in association with them, possibly to make the membrane more rigid. However, this explanation is implausible as well, since the samples of the validation experiment of the 10 % LB model are clustering close to the experimental samples in the PC1 score plot as well (in Figure 5.3). However, the fungi used in the validation experiment were grown the same way as the fungi analysed for the model building and the dunite grains were added just before the extraction. Thus, the grains could not have had an influence on the membrane structure and composition during the growth of the fungi.

It is probable that the presence of grains impacted the extraction yield instead of the membrane composition itself, due to the added physical force that the moving grains present to the fungal cells. If this is the case, this could also have influenced the biomass estimations. This could also be an explanation for the difference in accuracy between the validation experiments (see Table 4.6). The fungi for the 10 % LB validation experiment were extracted in the presence of dunite grains,and led to overall less accurate results than the validation experiment of the 10 % LB in ASW model, in which the fungi were extracted without the dunite grains.

It is also possible that the grain size influenced the biomass amounts within the experiments. In syringe pump experiment 3 and 4 two different grain size ranges were used (see Table 3.1). In these experiments it seems that there is less biomass amount in the samples with medium sized grains (1-2 mm). The mean of the biomass estimations of the medium sized grains (inoculated + blank samples) is 491 µg and for the big grain sizes (2-4 mm) 595 µg. A surprising result considering the significant amount of biomass that grew into the syringes of the samples with the medium grain size. This upstream orientation of the growth has been reported in the literature before and seems to be a common phenomenon in filamentous fungi (OH et al., 1997). In the samples with the big grain sizes the increased size of the grains probably caused larger pore spaces as well. This means the fungi could have had more space withing the vials to spread out, which could be the reason why pronounced growth of mycelium into the syringes was not observed in these samples. However, the differences between the samples from the big grain sizes to the small grain sizes could also just be an artifact resulting from the small number of samples, as the differences are just minor.

Generally, in future experiments the influence of the presence of rock grains should be considered and model building should be conducted with fungi extracted in the presence of the same material that is also present during the experiments to improve the estimation results.

The duration of the experiments is a probable cause for the higher amount of biomass in the permeability experiments as well, since the syringe pump experiments lasted for 2 weeks each while the permeability experiments lasted for three weeks. The only exception is the 70 bar experiment,

which lasted two weeks as well and which resulted in a mean estimation of 774.57 µg, which is still slightly higher than the estimations of the syringe pump experiments.

This difference in the duration could be the reason for the lower amount of biomass in the 70 bar experiment compared to the 2 bar experiments (see Table 4.9).

Next to the lower duration of the experiment, it could also be that the pressure itself constrained the biomass development in the 70 bar experiment. Pressure as a limiting factor requires further investigations as it is yet poorly understood and underexplored (SCHRENK et al., 2010). The pressure in the oceans increase at a rate of approximately 10 MPa/km and 30 MPa/km for lithostatic pressure, necessitating a rigid cell wall to outstand this impacting force (SCHRENK et al., 2010). However, diverse culturing experiments show that the pressure seems to be just a small obstacle (RAGHUKUMAR & RAGHUKUMAR, 1998, RAGHUKUMAR et al., 2004, DAMARE et al., 2006, SINGH et al., 2010). The fungi on which this was tested were isolates from deep sea sediments from depths between 860 <5000m below sea level as well as terrestrial fungi. And even though the terrestrial fungi were initially stressed, they adapted to the new circumstances (DAMARE et al., 2006). This suggests that the biomass development could have initially been limited due to the increased stress of the fungi resulting in a lower biomass in the 70 bar experiment compared to the 2 bar experiments. This increased stress and force that acts on the fungi could also have resulted in a different cell-membrane composition and caused the fungi grown at 70 bar to have more or less ergosterol and other components. This could have influenced the biomass estimations as well.

Another reason for the higher biomass of the 2 bar experiments could be the bacterial communities that were observed during the SEM investigation (see Figure 4.19 and Figure 4.18). Even though hyphae were observed in these samples as well, the majority of found organisms were bacteria. This leads to the conclusion, that components of the bacteria were obtained during the extraction as well, which could have altered the biomass estimations by the model. It is important to note that also some bacteria and protozoa can synthesize ergosterol (MANSOLDO et al., 2020).

More fungal material was found in the 70 bar experiment sample during the SEM analysis, which could be a result of coincidence, as only small amounts of sample were investigated, or it could mean that more fungal biomass developed during the 70 bar experiments, contradicting the biomass estimations. The bacteria might have outcompeted the fungi in the 2 bar experiments while their growth was restrained by the pressure in the 70 bar experiment.

In summary, the difference between the biomass estimations of the permeability and the syringe pump experiments could be explained by many different variables. The interpretation of these estimates should be done with care since the model accuracies pose major limitations to the estimations and need more fine adjustments especially in terms of the influence of the presence of grains on the extraction and fluorescence measurements and the subsequent biomass estimations.

Moreover, model building should be done with the addition of rock grains during the extraction procedure to explore the applicability of the models to these experiments further. Generally, it is advised against using these models for environmental samples with many unknown variables as they prove to not be robust against unexplored interferences.

5.2 Fungal Impact on Permeability

At the beginning of each permeability experiment the permeability shows strong fluctuations. For the experiments at 2 bar these fluctuations are between 1.2×10^{-13} m² and 6.2×10^{-14} m² for the inoculated experiments and between 1.9×10^{-13} m² and 9.4×10^{-14} m² for the blank experiment (see Figure 4.14, Figure 4.15, Figure 4.16 and Figure 4.17). The difference between the inlet and the outlet pressure during these strong fluctuations is within the uncertainty range of the measurements at 2 bar at 0.1 ml/min (data not shown), which leads to the conclusion that the basalt grains do not provide enough resistance to build up a pressure gradient, resulting in these fluctuations. The fluctuation range of the blank experiment differs from the inoculated ones. The reason for this is most likely the higher flow rate used in this experiment, as the flow rate has an influence on the permeability (Equation 2). In the blank experiment it was not possible to stabilize the pressure at 2 bar using a flow rate of 0.1 ml/min. That is why a flow rate of 0.15 ml/min was used in the blank experiment. And while the fluctuations are visible for the entire duration of the blank experiment, for the inoculated experiments these fluctuations cease as a pressure gradient is build up suggesting biomass growth.

For the 2 bar experiments an asymptotic decrease in permeability is visible (Figure 4.14 and Figure 4.15). This initial strong decrease followed by stabilization with a small tendency to decrease further was observed in previous bioclogging experiments with both bacteria and fungi as well as mixed communities, e. g. SEKI et al., 1998, SEKI et al., 2002, ZHONG et al., 2013, ZHONG & WU, 2013.

However, this stabilized, slight decrease in permeability is interrupted by sudden increases in permeability followed by a gradual decrease again (compare Figure 4.14 and Figure 4.15). DUPIN & MCCARTY (2000) observed a similar pattern and explained it by the flushing out of biomass due to increased shear forces. The increased shear forces are a result of the increased flow velocities brought about by a decrease in porosity due to biomass development (THULLNER, 2010). These sudden increases in permeability during the 2 bar experiments could accordingly be explained by a sudden removal of biomass.

The beginning of the 70 bar experiments, shows strong fluctuations as well, however, these have negative values (Figure 4.16). This means that the flow direction was from the lower pressure to the higher pressure, i. e. the inlet pressure was lower than the outlet pressure. This is an unlikely trend and could be explained by measurement uncertainties and that the fluid flow was not hindered by the

basalt grains within the Teflon sleeves sufficiently to create a recordable pressure gradient. The uncertainty of the permeability measurement at that pressure and flow rate was tried to be determined, however, after the first 70 bar experiment keeping the pressure that high with a low flow rate of 0.1 ml/min was unsuccessful (further discussion see later).

These negative permeability values change suddenly with one positive peak after four days and then for a longer period after five days. This could be due to a shift in the permeability brought about by biomass growth. Alternatively, this could also be due to the uncertainty of the pressure measurements.

After six days a clear downward trend in permeability is visible. However, this downward trend is accompanied by significant perturbations distinguishable as peaks of higher permeability. This variability in the data could be ascribed to either the aforementioned measurement uncertainties but possibly also to biomass detachment. This would mean that the biomass detachment is much more frequent and pronounced than in the 2 bar experiments. Considering that the pressure is much higher the shear forces would be too, hence it is very likely that the biomass is more prone to being flushed out. This would also explain why the permeability decrease in the 2 bar experiments is much stronger than the permeability decrease in the 70 bar experiment (see section 4.3.2). If this is applied to the oceanic crust this would mean that the higher the pressure, so the deeper below the surface, the smaller the influence of the microorganisms on the permeability.

However, it should be noted that the uncertainty of the pressure measurements could be higher at higher pressures, which could mean that these peaks during the permeability decrease are a result of the measurement uncertainties rather than from the detachment of biomass. Overall, the established pressure gradient and the pressure change was not sufficient enough to draw conclusions.

After four days of this decreasing trend new strong fluctuations are visible. In this case the fluctuations last until the experiment was terminated and have strong changes between positive and negative permeabilities. This is correlated with multiple pressure drops that occurred at the same time until the end of the experiment (see Figure 5.5). It would be reasonable to assume that these drops in pressure could evidence an issue of the backpressure regulator, as it is this device that controls the pressure within the system. However, it was observed that these pressure drops occurred mainly when the pistons of the pump changed to the one on the right. The Vindum pump is a dual-piston pump. That means that one piston pumps the fluid into the system while the other fills itself with fluid. This ensures a continuous flow. The pressure drops occurred when the left piston stopped to pump and the right piston started to.

The Vindum pump records the pressure within the pump, i. e. the pressure with which the fluids are pumped into the system. The pressure development within the pump of the second inoculated 2 bar experiment displayed a recurring pattern of minor pressure changes followed by strong fluctuations. This is shown as a plot in Figure 5.6. The period of small fluctuations is simultaneous to the pumping of the left piston and the strong fluctuations are caused when the right piston pumped

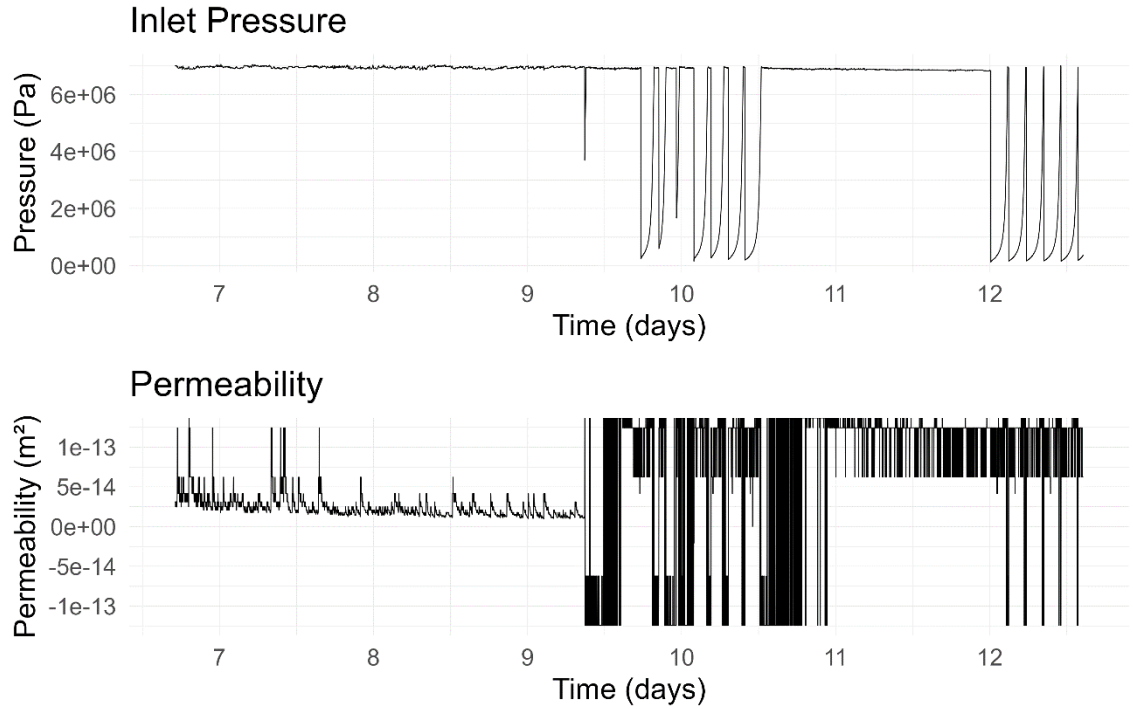

Figure 5.5: Comparison of the inlet pressure fluctuations and the permeability fluctuations during the 70 bar experiment. Note that the strong fluctuations in permeability start simultaneously to the pressure drops.

fluids into the system. This indicates that the pump or at least the right piston is damaged in some form. This is underlined by white precipitations that appeared over the course of the experiments on top of both pistons. The precipitations are in a higher amount on the right piston. This would indicate a leak inside the pump if the precipitations proof to be salts. This could be an explanation why it was not possible to have high pressures with low flow rates.

However, the pump was not the only weak spot that caused problems for the execution of the experiments. The bleeding valve, which is used to expel gas from the system, started to leak over the course of the experiments, which impeded the build-up and stabilization of pressure at low flow rates. This was the probable cause that the uncertainty experiment could not be executed at 70 bar for 0.1 ml/min as the pressure could not be kept at low flow rates.

However, when the pressure was increased and stabilized, an immediate steep pressure drop occurred after reducing the flow rate. The leakage caused by the bleeding valve was not pronounced enough to cause such a significant loss in pressure. No explanation could be found for this phenomenon at this point. Additionally, sometimes it was also a problem to stabilize the system at 2 bar. The leak of the bleeding valve only occurred at higher pressures and no other leaks (except for the possible leak inside the pump) were found. This could mean that the backpressure regulator is prone to malfunction as well. One possible reason for this was determined to be the partial obstruction of the filter in front of the backpressure regulator by small particles. This could have caused an

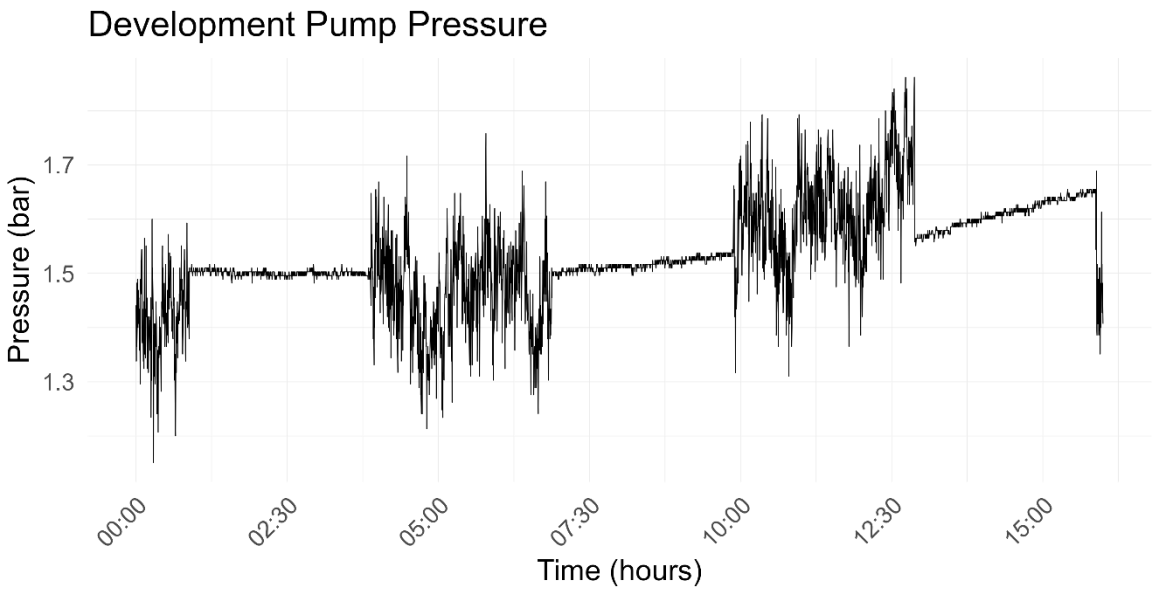

Figure 5.6: Development of the pressure inside the pump from the second 2 bar inoculated experiment. The development is from the beginning of the second inoculated permeability experiment. The strong fluctuations in the pressure, that can be seen, occur while the right piston is pumping, the periods of little fluctuations are simultaneous to the left piston pumping.

increase in fluid velocity and thus in local pressure to which the backpressure reacted. Therefore, it is suggested to make it to a routine to clean that filter before every experiment.

Another issue faced during the experiments is contamination. Bacterial contamination was observed during the SEM in both inoculated 2 bar experiments as shown in Figure 4.19 and Figure 4.18. The fluid reservoirs for all experiments were autoclaved and covered with autoclaved aluminium foil during the experiment and the inlet and outlet tubes were sterilized. Between each experiment the system was flushed with a 0.5 % sodium hypochlorite solution for at least 2 hours. Despite these precautions the experiments were contaminated. In the future a better solution to ensure the integrity of the system needs to be found.

This issue is highlighted by the second inoculated permeability experiment, that was set up as a blank experiment and yet, after two days a cloudiness in the fluid reservoir was observed. The contaminations of the second 2 bar permeability experiment is the reason why the final blank experiment was undertaken with ASW without medium. This was done to prevent or at least reduce the microbial growth.

It cannot be excluded that bacteria were introduced into the system during the 70 bar experiment as well. However, no bacteria were observed during the SEM investigation of the sample from that experiment. It is possible that the increased pressure represents a challenge for certain organisms and reduced or overall prevented bacterial growth.

Provided that the 70 bar experiment was not contaminated., the bacterial contamination in the 2 bar experiments could be the reason why the decrease in permeability was higher in the 2 bar experiments than the decrease in the 70 bar experiment. During the SEM a larger quantity of

organisms, the majority of which were bacteria, were found in the 2 bar experiments. In both the 2 bar but also the 70 bar experiments no big quantities of fungi could be found. One explanation could be that the bacteria attach themselves more effectively to the grains than the fungi. DUPIN & MCCARTY (2000) have found that organisms that attach to surfaces more strongly have a more significant effect on the permeability. This could mean that the bacteria had a significant influence on the permeability development of the 2 bar experiments while the results of the 70 bar experiment potentially represent the influence of the fungi on the permeability more accurately.

Following this line of reasoning, it could be inferred that the 2 bar experiments represent the actual influence of microbes on the permeability in the oceanic crust more accurately as a mixed microbial community, as seen in the 2 bar permeability experiment, is to be expected in the deep biosphere habitat. Yet, it should be kept in mind that the identity of the bacteria within the permeability experiments are unknown, which is why it cannot be estimated how reliably they represent the influence of in-situ bacteria.

However, the difference in the permeability developments between the 70 bar and the 2 bar experiments could also be due to the above-mentioned uncertainty of pressure measurements.

The relationship between biomass development and permeability decrease can only be speculated as the analysis of it is limited by the small number of experiments conducted, the inaccuracies of the biomass estimation models and the difficulties during the permeability experiments. The 70 bar experiment had the lowest estimated biomass amount and the lowest permeability decrease as well. In spite of that, the first 2 bar permeability experiment has a higher estimated biomass than the second 2 bar permeability experiment (see Table 4.9) and yet there is a slightly more pronounced loss in permeability in the second 2 bar permeability experiment (compare Figure 4.14 and Figure 4.15). As mentioned above, this could be a result of the biomass estimation uncertainties. Another possibility is that the flow paths, flow velocity, pore spaces as well as pore space distribution plays an important role in the influence of biomass development on permeability decrease as well. This could mean that these variables were slightly different between the first and the second inoculated 2 bar experiments. More experiments need to be conducted to establish a pattern and understand this behaviour. Additionally, in the future porosity experiments are recommended to take this characteristic under consideration as well.

Overall, it was established that the custom-build Parr flow-through autoclave can be used for experiments aimed to determine the influence of fungi and other organisms on the permeability of porous materials if the integrity and functionality of the system are ensured. In the future it is suggested to execute experiments with additional 1 µm filters to hamper the introduction of bacteria to the system but also to simulate a narrowing of a fracture system or the reduction of the porosity. Over the course of the experiments the fluids in the fluid reservoir got cloudy, which means that some amount of organic matter was also flushed out of the reaction chamber, the 1 µm filter could also prevent this removal of organic matter to a certain degree. This will encourage a stronger and/or

faster decrease in permeability and can support the identification of the relationship between biomass and permeability decrease in future experiments. It also is recommended to increase the experiment duration to get a better understanding of a long-term development of the permeability. It would also be appropriate to use smaller grain sizes to reduce the initial permeability. This would reduce the risk of the strong fluctuations at the beginning of the experiments. Additionally, this would represent the actual circumstances inside the crust more accurately, as the average permeability within the crust is lower than the initial permeability in these experiments (compare section 2.1.1 and 4.3.2).

Another suggestion for experiments is to simulate a fracture system within the oceanic crust by glueing a core of basalt into a Teflon sleeve with inert and pressure resistant glue (e. g. epoxy resin). This sleeve with the crust sample inside can then be cut in half and inserted into the pressure chamber. Alternatively, the core could be cut in half before glueing it into the Teflon sleeve. This would reduce the initial permeability significantly and would most likely result in a faster reduction of permeability by bioclogging.

6 Conclusions

The goal of this study was to find methods for the investigation of fungal growth and its influence on the permeability of the oceanic crust. To accomplish this, two different biomass estimation methods were explored, one of which is a general method and the other species specific. Additionally, a custom-build Parr flow-through autoclave was tested as an investigation tool for the influence of fungal growth on permeability.

While the biomass estimation methods showed little reliability in their estimations, the flow-through autoclave proved to be a useful instrument for measuring the change in permeability over time. The results of the inoculated 2 bar experiments show a clear decrease in permeability, strongly indicating the influence of microbial growth on the permeability. However, due to the contamination with bacteria in the 2 bar experiments it is difficult to assess how much of the reduction is due to fungal growth and how much due to bacteria. Irrespective of which of the organisms contributed most to the decrease, the results are relevant because in a natural system a mixed fungal and bacterial community is to be expected. However, that fungi have an influence on permeability by themselves is shown in the experiment at 70 bar, proving that also under pressure microorganism can have an influence on permeability.

Using the flow-through autoclave opens a wide spectrum of studies pertaining the influence of microorganisms on the permeability of crustal and sedimentary habitats. Not only can the influence of fungi be investigated but also the influence of bacteria, archaea and mixed communities. In this way a comprehensive insight into bioclogging within the crust can be obtained. By using different pressures, a gradient of microbial influence depending on depth can be established. With a sufficient amount of data, the influence of microorganisms on the permeability of the crust could be added to fluid circulation models. It would also help to estimate the influence of biomass growth on pressure, flow rate and flow velocity. Not only that, using X-ray microtomography the flow-through autoclave can also be used to understand the community structure and growth architecture of the microorganisms in the deep biosphere better.

With more data it will also be proven to be easier to estimate the connection between biomass amount and permeability decrease as the data generated in this study is not sufficient to do this satisfactorily. Generally, it seems that other variables influence the magnitude of permeability decrease as well, which are speculated to be flow paths, flow velocity, pore spaces as well as pore space distribution. However, this conclusion should be considered with caution, as the biomass estimation methods did not provide reliable results.

The most substantial obstacle for the biomass estimations were the low amounts of biomass used in this study. The LOI method is an established method for the estimation of organic matter in samples and MANSOLDO et al. (2020) established an autofluorescence PLS model with high

reliability. That is why it cannot be excluded that with larger biomasses these methods are feasible. The development of fungal biomass in the experiments conducted in this study was low, as it would be expected in the deep biosphere, where it would most likely be even slower. Accordingly, other methods for the estimation of fungal biomass that are more robust towards low amounts, should be explored.

This thesis set the foundation of a broad spectrum of future studies to investigate the influence of microbial growth on the permeability in the crustal but also sedimentary habitat. This is an important puzzle piece to understand the deep biosphere and its influence on geobiochemical cycles and their connection to the surface realms better.

Literature

ABDI, H. (2003). Partial least square regression (PLS regression). Encyclopedia for research methods for the social sciences, 6(4), 792-795.

ADEYEMI, A. O., & GADD, G. M. (2005). Fungal degradation of calcium-, lead-and silicon-bearing minerals. Biometals, 18, 269-281.

AIYAMA, R., TRIVITTAYASIL, V., & TSUTA, M. (2018). Discrimination of aflatoxin contamination level in nutmeg by fluorescence fingerprint measurement. Food control, 85, 113-118.

AMIRI, F., MOUSAVI, S. M., & YAGHMAEI, S. (2011). Enhancement of bioleaching of a spent Ni/Mo hydroprocessing catalyst by Penicillium simplicissimum. Separation and purification technology, 80(3), 566-576.

AOKI, K. (1984). Measurement of fluorescence spectra as a new technique for study of sedimentary zircons. The Journal of the Geological Society of Japan, 90(9), 659-662.

BAAS BECKING, L.G.M. (1934) Geobiologie of inleiding tot de milieukunde. The Hague, the Netherlands: W.P. Van Stockum & Zoon (in Dutch).

BACH, W., BEIER, C., PECKMANN, J., BAUER, J., BIRGEL, D., & CARAITE, I. (2019). RV Maria S Merian Report Vesteris Seamount.

BECKER, K., & DAVIS, E. E. (2003). New evidence for age variation and scale effects of permeabilities of young oceanic crust from borehole thermal and pressure measurements. Earth and Planetary Science Letters, 210(3-4), 499-508.

BENGTSON, S., IVARSSON, M., ASTOLFO, A., BELIVANOVA, V., BROMAN, C., MARONE, F., & STAMPANONI, M. (2014). Deep-biosphere consortium of fungi and prokaryotes in Eocene subseafloor basalts. Geobiology, 12(6), 489-496.

BENGTSON, S., RASMUSSEN, B., IVARSSON, M., MUHLING, J., BROMAN, C., MARONE, F., ... & BEKKER, A. (2017). Fungus-like mycelial fossils in 2.4-billion-year-old vesicular basalt. Nature Ecology & Evolution, 1(6), 0141.

BERTANI, G. (1951). Studies on lysogenesis I: the mode of phage liberation by lysogenic Escherichia coli. Journal of bacteriology, 62(3), 293-300.

BINDSCHEDLER, S., CAILLEAU, G., & VERRECCHIA, E. (2016). Role of fungi in the biomineralization of calcite. Minerals, 6(2), 41.

BLACK, W. D. (2020). A comparison of several media types and basic techniques used to assess outdoor airborne fungi in Melbourne, Australia. PLoS One, 15(12), e0238901.

BRAUN, S., MHATRE, S. S., JAUSSI, M., RØY, H., KJELDSEN, K. U., PEARCE, C., SEIDENKRANTZ, M.-S., JØRGENSEN, B. B. & LOMSTEIN, B. A. (2017). Microbial turnover times in the deep seabed studied by amino acid racemization modelling. Scientific reports, 7(1), 5680.

BURFORD, E. P., KIERANS, M., & GADD, G. M. (2003). Geomycology: fungi in mineral substrata. Mycologist, 17(3), 98-107.

CAMPOS, C., MORENO RUIZ, L. A., FRAGOSO-SORIANO, R., SATO-BERRÚ, R. Y., HERNÁNDEZ-PÉREZ, E., & FERNÁNDEZ, F. J. (2022). Surface-enhanced Raman spectroscopy and ultrastructural analysis of penicillin-producing Penicillium rubens strains. Journal of Microscopy, 286(1), 22-30.

CHARCOSSET, J. Y., & CHAUVET, E. (2001). Effect of culture conditions on ergosterol as an indicator of biomass in the aquatic hyphomycetes. Applied and environmental microbiology, 67(5), 2051-2055.

CHONG, I. G., & JUN, C. H. (2005). Performance of some variable selection methods when multicollinearity is present. Chemometrics and intelligent laboratory systems, 78(1-2), 103-112.

CIPULLO, S., NAWAR, S., MOUAZEN, A. M., CAMPO-MORENO, P., & COULON, F. (2019). Predicting bioavailability change of complex chemical mixtures in contaminated soils using visible and near-infrared spectroscopy and random forest regression. Scientific reports, 9(1), 4492.

COCKELL, C. S., SANTOMARTINO, R., Finster, K., WAAJEN, A. C., EADES, L. J., MOELLER, R., ... & DEMETS, R. (2020). Space station biomining experiment demonstrates rare earth element extraction in microgravity and Mars gravity. Nature communications, 11(1), 5523.

COWEN, J. P., GIOVANNONI, S. J., KENIG, F., JOHNSON, H. P., BUTTERFIELD, D., RAPPÉ, M. S., ... & LAM, P. (2003). Fluids from aging ocean crust that support microbial life. Science, 299(5603), 120-123.

CRAMERI, F., CONRAD, C. P., MONTÉSI, L., & LITHGOW-BERTELLONI, C. R. (2019). The dynamic life of an oceanic plate. Tectonophysics, 760, 107-135.

CROCE, A. C. (2021). Light and autofluorescence, multitasking features in living organisms. Photochem, 1(2), 67-124.

DAMARE, S., RAGHUKUMAR, C., & RAGHUKUMAR, S. (2006). Fungi in deep-sea sediments of the Central Indian Basin. Deep Sea Research Part I: Oceanographic Research Papers, 53(1), 14-27.

DARCY, H. (1856). The public fountains of the city of Dijon. Victor Dalmont, Paris, France.

DEISING, H. B., WERNER, S., & WERNITZ, M. (2000). The role of fungal appressoriain plant infection. Microbes and infection, 2(13), 1631-1641.

DRAKE, H., IVARSSON, M., HEIM, C., SNOEYENBOS-WEST, O., BENGTSON, S., BELIVANOVA, V., & WHITEHOUSE, M. (2021). Fossilized anaerobic and possibly methanogenesis-fueling fungi identified deep within the Siljan impact structure, Sweden. Communications Earth & Environment, 2(1), 34.

DUNNING, G. R., & PEDERSEN, R. B. (1988). U/Pb ages of ophiolites and arc-related plutons of the Norwegian Caledonides: implications for the development of Iapetus. Contributions to Mineralogy and Petrology, 98, 13-23.

DUPIN, H. J., & MCCARTY, P. L. (2000). Impact of colony morphologies and disinfection on biological clogging in porous media. Environmental science & technology, 34(8), 1513-1520.

EHRLICH, H. L. (2006). Geomicrobiology: relative roles of bacteria and fungi as geomicrobial agents. Fungi in biogeochemical cycles, 1-27.

ELMASRY, G., NAGAI, H., MORIA, K., NAKAZAWA, N., TSUTA, M., SUGIYAMA, J., ... & NAKAUCHI, S. (2015). Freshness estimation of intact frozen fish using fluorescence spectroscopy and chemometrics of excitation–emission matrix. Talanta, 143, 145-156.

EMERSON, D., & FLOYD, M. M. (2005). Enrichment and isolation of iron-oxidizing bacteria at neutral pH. Methods in enzymology, 397, 112-123.

ETIENNE, S., & DUPONT, J. (2002). Fungal weathering of basaltic rocks in a cold oceanic environment (Iceland): comparison between experimental and field observations. Earth Surface Processes and Landforms: The Journal of the British Geomorphological Research Group, 27(7), 737-748.

FEDOSEEVA, E. V., DANILOVA, O. A., IANUTSEVICH, E. A., TEREKHOVA, V. A., & TERESHINA, V. M. (2021). Micromycete lipids and stress. Microbiology, 90, 37-55.

FEDOSEEVA, E., PATSAEVA, S., STOM, D., & TEREKHOVA, V. (2022). Excitation-dependent fluorescence helps to indicate fungal contamination of aquatic environments and to differentiate filamentous fungi. In Photonics (Vol. 9, No. 10, p. 692). MDPI.

FEOFILOVA, E. P. (2010). The fungal cell wall: modern concepts of its composition and biological function. Microbiology, 79, 711-720.

FINLAY, R. D., ROSLING, A., & GADD, G. M. (2006). Integrated nutrient cycles in boreal forest ecosystems-the role of mycorrhizal fungi. Fungi in biogeochemical cycles, 24, 28.

FISHER, A. T. (1998). Permeability within basaltic oceanic crust. Reviews of Geophysics, 36(2), 143-182.

FISHER, A. T. (2005). Marine hydrogeology: recent accomplishments and future opportunities. Hydrogeology Journal, 13, 69-97.

FISHER, A. T., & BECKER, K. (2000). Channelized fluid flow in oceanic crust reconciles heat-flow and permeability data. Nature, 403(6765), 71-74.

FLEMING, A. (1929). On the antibacterial action of cultures of a penicillium, with special reference to their use in the isolation of B. influenzae. British journal of experimental pathology, 10(3), 226.

FOMINA, M., BURFORD, E. P., HILLIER, S., KIERANS, M., & GADD, G. M. (2010). Rock-building fungi. Geomicrobiology Journal, 27(6-7), 624-629.

FRANZ, G., KHOMENKO, V., LYCKBERG, P., CHOURNOUSENKO, V., STRUCK, U., GERNERT, U., & NISSEN, J. (2023). The Volyn biota (Ukraine)–indications of 1.5 Gyr old eukaryotes in 3D preservation, a spotlight on the "boring billion". Biogeosciences, 20(10), 1901-1924.

FUJITA, K., TSUTA, M., KOKAWA, M., & SUGIYAMA, J. (2010). Detection of deoxynivalenol using fluorescence excitation–emission matrix. Food and Bioprocess Technology, 3, 922-927.

FURNES, H., PEDERSEN, R. B., & STILLMAN, C. J. (1988). The Leka Opholite Complex, central Norwegian Caledonides: field characteristics and geotectonic significance. Journal of the Geological Society, 145(3), 401-412.

GADD, G. M. (1999). Fungal production of citric and oxalic acid: importance in metal speciation, physiology and biogeochemical processes. Advances in microbial physiology, 41, 47-92.

GADD, G. M. (2017). Fungi, rocks, and minerals. Elements: An International Magazine of Mineralogy, Geochemistry, and Petrology, 13(3), 171-176.

GEE, M. A. M., THIRLWALL, M. F., TAYLOR, R. N., LOWRY, D., & MURTON, B. J. (1998). Crustal processes: major controls on Reykjanes Peninsula lava chemistry, SW Iceland. Journal of Petrology, 39(5), 819-839.

GELADI, P., & KOWALSKI, B. R. (1986). Partial least-squares regression: a tutorial. Analytica chimica acta, 185, 1-17.

GERM (2000). The Geochemical Earth Reference Model, http://EarthRef.org/agenda.htm.

GLEESON, D. B., CLIPSON, N., MELVILLE, K., GADD, G. M., & MCDERMOTT, F. P. (2005). Characterization of fungal community structure on a weathered pegmatitic granite. Microbial Ecology, 50, 360-368.

GOLD, T. (1992). The deep, hot biosphere. Proceedings of the National Academy of Sciences, 89(13), 6045-6049.

GOSTINČAR, C., ZALAR, P., & GUNDE-CIMERMAN, N. (2022). No need for speed: Slow development of fungi in extreme environments. Fungal Biology Reviews, 39, 1-14.

GROSCH, E. G., & HAZEN, R. M. (2015). Microbes, mineral evolution, and the rise of microcontinents—origin and coevolution of life with early earth. Astrobiology, 15(10), 922-939.

GUDBRANDSSON, S., WOLFF-BOENISCH, D., GISLASON, S. R., & OELKERS, E. H. (2011). An experimental study of crystalline basalt dissolution from $2 \leqslant pH \leqslant 11$ and temperatures from 5 to 75 C. Geochimica et Cosmochimica Acta, 75(19), 5496-5509.

HELENO, S. A., DIZ, P., PRIETO, M. A., BARROS, L., RODRIGUES, A., BARREIRO, M. F., & FERREIRA, I. C. (2016). Optimization of ultrasound-assisted extraction to obtain mycosterols from Agaricus bisporus L. by response surface methodology and comparison with conventional Soxhlet extraction. Food chemistry, 197, 1054-1063.

HOMMEL, J., COLTMAN, E., & CLASS, H. (2018). Porosity–permeability relations for evolving pore space: a review with a focus on (bio-) geochemically altered porous media. Transport in Porous Media, 124(2), 589-629.

HOOGSTEEN, M. J., LANTINGA, E. A., BAKKER, E. J., GROOT, J. C., & TITTONELL, P. A. (2015). Estimating soil organic carbon through loss on ignition: effects of ignition conditions and structural water loss. European Journal of soil science, 66(2), 320-328.

HUBER, M. L., PERKINS, R. A., LAESECKE, A., FRIEND, D. G., SENGERS, J. V., ASSAEL, M. J., METAXA, I. N.; VOGEL, E., MAREŠ, R. & MIYAGAWA, K. (2009). New international formulation for the viscosity of H2O. Journal of Physical and Chemical Reference Data, 38(2), 101-125.

IACOBUCCI, D., SCHNEIDER, M. J., POPOVICH, D. L., & BAKAMITSOS, G. A. (2016). Mean centering helps alleviate “micro” but not “macro” multicollinearity. Behavior research methods, 48, 1308-1317.

IVARSSON, M., BENGTSON, S., & NEUBECK, A. (2016a). The igneous oceanic crust–Earth's largest fungal habitat?. Fungal Ecology, 20, 249-255.

IVARSSON, M., BENGTSON, S., BELIVANOVA, V., STAMPANONI, M., MARONE, F., & TEHLER, A. (2012). Fossilized fungi in subseafloor Eocene basalts. Geology, 40(2), 163-166.

IVARSSON, M., BENGTSON, S., DRAKE, H., & FRANCIS, W. (2018). Fungi in deep subsurface environments. Advances in applied microbiology, 102, 83-116.

IVARSSON, M., BENGTSON, S., SKOGBY, H., LAZOR, P., BROMAN, C., BELIVANOVA, V., & MARONE, F. (2015a). A fungal-prokaryotic consortium at the basalt-zeolite interface in subseafloor igneous crust. PLoS One, 10(10), e0140106.

IVARSSON, M., DRAKE, H., BENGTSON, S., & RASMUSSEN, B. (2020a). A cryptic alternative for the evolution of hyphae. Bioessays, 42(6), 1900183.

IVARSSON, M., DRAKE, H., NEUBECK, A., SALLSTEDT, T., BENGTSON, S., ROBERTS, N. M. W., & RASMUSSEN, B. (2020b). The fossil record of igneous rock. Earth-Science Reviews, 210, 103342

IVARSSON, M., HOLM, N. G., & NEUBECK, A. (2016b). The deep biosphere of the subseafloor igneous crust. Trace metal biogeochemistry and ecology of deep-sea hydrothermal vent systems, 143-166.

IVARSSON, M., PECKMANN, J., TEHLER, A., BROMAN, C., BACH, W., BEHRENS, K., ... & NORBÄCK IVARSSON, L. (2015b). Zygomycetes in vesicular basanites from Vesteris Seamount, Greenland Basin–a new type of cryptoendolithic fungi. PLoS One, 10(7), e0133368.

IVARSSON, M., SCHNÜRER, A., BENGTSON, S., & NEUBECK, A. (2016c). Anaerobic fungi: a potential source of biological H2 in the oceanic crust. Frontiers in microbiology, 7, 674.

IYER, K., AUSTRHEIM, H., JOHN, T., & JAMTVEIT, B. (2008). Serpentinization of the oceanic lithosphere and some geochemical consequences: constraints from the Leka Ophiolite Complex, Norway. Chemical Geology, 249(1-2), 66-90.

JØRGENSEN, B. B., & BOETIUS, A. (2007). Feast and famine—microbial life in the deep-sea bed. Nature Reviews Microbiology, 5(10), 770-781.

JØRGENSEN, S. L., & ZHAO, R. (2016). Microbial inventory of deeply buried oceanic crust from a young ridge flank. Frontiers in Microbiology, 7, 185135.

KAROUI, R., & BLECKER, C. (2011). Fluorescence spectroscopy measurement for quality assessment of food systems—a review. Food and Bioprocess technology, 4, 364-386.

KIRTZEL, J., UEBERSCHAAR, N., DECKERT-GAUDIG, T., KRAUSE, K., DECKERT, V., GADD, G. M., & KOTHE, E. (2020). Organic acids, siderophores, enzymes and mechanical pressure for black slate bioweathering with the basidiomycete Schizophyllum commune. Environmental microbiology, 22(4), 1535-1546.

KNAUS, H., BLAB, G. A., VAN VELUW, G. J., GERRITSEN, H. C., & WÖSTEN, H. A. (2013). Label-free fluorescence microscopy in fungi. Fungal biology reviews, 27(2), 60-66.

KOKAWA, M., NISHI, K., ASHIDA, H., TRIVITTAYASIL, V., SUGIYAMA, J., & TSUTA, M. (2017). Predicting the heating temperature of soymilk products using fluorescence fingerprints. Food and Bioprocess Technology, 10, 462-468.

KOWALCZUK, P., STOŃ-EGIERT, J., COOPER, W. J., WHITEHEAD, R. F., & DURAKO, M. J. (2005). Characterization of chromophoric dissolved organic matter (CDOM) in the Baltic Sea by excitation emission matrix fluorescence spectroscopy. Marine Chemistry, 96(3-4), 273-292.

KRUBER, C., THORSETH, I. H., & PEDERSEN, R. B. (2008). Seafloor alteration of basaltic glass: Textures, geochemistry, and endolithic microorganisms. Geochemistry, Geophysics, Geosystems, 9(12).

LANDEWEERT, R., HOFFLAND, E., FINLAY, R. D., KUYPER, T. W., & VAN BREEMEN, N. (2001). Linking plants to rocks: ectomycorrhizal fungi mobilize nutrients from minerals. Trends in ecology & evolution, 16(5), 248-254.

LENNOX, E. S. (1955). Transduction of linked genetic characters of the host by bacteriophage P1. Virology, 1(2), 190-206.

LILAND K, MEVIK B, WEHRENS R (2023). _pls: Partial Least Squares and Principal Component Regression_. R package version 2.8-3, <https://CRAN.R-project.org/package=pls>.

LINDAHL, B., STENLID, J. A. N., OLSSON, S., & FINLAY, R. (1999). Translocation of 32P between interacting mycelia of a wood-decomposing fungus and ectomycorrhizal fungi in microcosm systems. The New Phytologist, 144(1), 183-193.

LUEDELING, E., CASPERSEN, L., FERNANDEZ, E. (2023). _chillR: Statistical Methods for Phenology Analysis in Temperate Fruit Trees_. R package version 0.74, <https://CRAN.R-project.org/package=chillR>.

LV, Q. Z., YAN, L., & JIANG, Y. Y. (2016). The synthesis, regulation, and functions of sterols in Candida albicans: Well-known but still lots to learn. Virulence, 7(6), 649-659.

LYSNES, K., TORSVIK, T., THORSETH, I. H., & PEDERSEN, R. B. (2004). Microbial populations in ocean floor basalt: results from ODP Leg 187. In Proceedings of the Ocean Drilling Program, Scientific Results (Vol. 187, pp. 1-27). College Station, TX: Ocean Drilling Program.

MACLENNAN, J. (2008). Lead isotope variability in olivine-hosted melt inclusions from Iceland. Geochimica et Cosmochimica Acta, 72(16), 4159-4176.

MANSOLDO, F. R. P., FIRPO, R., DA SILVA CARDOSO, V., QUEIROZ, G. N., CEDROLA, S. M. L., DE GODOY, M. G., & VERMELHO, A. B. (2020). New method for rapid identification and quantification of fungal biomass using ergosterol autofluorescence. Talanta, 219, 121238.

MARTINO, E., & PEROTTO, S. (2010). Mineral transformations by mycorrhizal fungi. Geomicrobiology Journal, 27(6-7), 609-623.

MBARECHE, H., VEILLETTE, M., TEERTSTRA, W., KEGEL, W., BILODEAU, G. J., WÖSTEN, H. A., & DUCHAINE, C. (2019). Recovery of fungal cells from air samples: a tale of loss and gain. Applied and Environmental Microbiology, 85(9), e02941-18.

MCMAHON, S., & PARNELL, J. (2018). The deep history of Earth's biomass. Journal of the Geological Society, 175(5), 716-720.

MEYER, J. L., JAEKEL, U., TULLY, B. J., GLAZER, B. T., WHEAT, C. G., LIN, H. T., ... & HUBER, J. A. (2016). A distinct and active bacterial community in cold oxygenated fluids circulating beneath the western flank of the Mid-Atlantic ridge. Scientific reports, 6(1), 22541

MONEY, N. P. (2004). The fungal dining habit: a biomechanical perspective. Mycologist, 18(2), 71-76.

MONTGOMERY, H. J., MONREAL, C. M., YOUNG, J. C., & SEIFERT, K. A. (2000). Determinination of soil fungal biomass from soil ergosterol analyses. Soil Biology and Biochemistry, 32(8-9), 1207-1217.

NATIONAL INSTITUTE OF STANDARDS AND TECHNOLOGY. (2023). Isothermal Properties of Water. Department of Commerce, Washington, D.C.. https://webbook.nist.gov/cgi/fluid.cgi?T=20&PLow=1&PHigh=70&PInc=1&Digits=5&ID=C7732185&Action=Load&Type=IsoTherm&TUnit=C&PUnit=bar&DUnit=mol%2Fl&HUnit=kJ%2Fmol&WUnit=m%2Fs&VisUnit=Pa*s&STUnit=N%2Fm&RefState=DEF, year of access: 2024

NEWELL, S. Y., MILLER, J. D., & FALLON, R. D. (1987). Ergosterol content of salt-marsh fungi: effect of growth conditions and mycelial age. Mycologia, 79(5), 688-695.

NIKSIC, M., HADZIC, I., & GLISIC, M. (2004). Is Phallus impudicus a mycological giant?. Mycologist, 18(1), 21-22.

OELKERS, E. H., & GISLASON, S. R. (2001). The mechanism, rates and consequences of basaltic glass dissolution: I. An experimental study of the dissolution rates of basaltic glass as a function of aqueous Al, Si and oxalic acid concentration at 25 C and pH= 3 and 11. Geochimica et cosmochimica acta, 65(21), 3671-3681.

OH, K. B., NISHIYAMA, T., SAKAI, E., MATSUOKA, H., & KURATA, H. (1997). Flow sensing in mycelial fungi. Journal of biotechnology, 58(3), 197-204.

ORCUTT, B. N., BACH, W., BECKER, K., FISHER, A. T., HENTSCHER, M., TONER, B. M., ... & EDWARDS, K. J. (2011a). Colonization of subsurface microbial observatories deployed in young ocean crust. The ISME journal, 5(4), 692-703.

ORCUTT, B. N., SYLVAN, J. B., KNAB, N. J., & EDWARDS, K. J. (2011b). Microbial ecology of the dark ocean above, at, and below the seafloor. Microbiology and molecular biology reviews, 75(2), 361-422.

ORSI, W., BIDDLE, J. F., & EDGCOMB, V. (2013). Deep sequencing of subseafloor eukaryotic rRNA reveals active fungi across marine subsurface provinces. PLOS one, 8(2), e56335.

PASANEN, A. L., YLI-PIETILÄ, K., PASANEN, P., KALLIOKOSKI, P., & TARHANEN, J. (1999). Ergosterol content in various fungal species and biocontaminated building materials. Applied and Environmental Microbiology, 65(1), 138-142.

PATHAK, A., NOWELL, R. W., WILSON, C. G., RYAN, M. J., & BARRACLOUGH, T. G. (2020). Comparative genomics of Alexander Fleming's original Penicillium isolate (IMI 15378) reveals sequence divergence of penicillin synthesis genes. Scientific Reports, 10(1), 15705.

PECKMANN, J., BACH, W., BEHRENS, K., & REITNER, J. (2008). Putative cryptoendolithic life in Devonian pillow basalt, Rheinisches Schiefergebirge, Germany. Geobiology, 6(2), 125-135.

PEDERSEN, K. (1993). The deep subterranean biosphere. Earth-science reviews, 34(4), 243-260.

PRASONGSUK, S., LOTRAKUL, P., ALI, I., BANKEEREE, W., & PUNNAPAYAK, H. (2018). The current status of Aureobasidium pullulans in biotechnology. Folia microbiologica, 63, 129-140.

R CORE TEAM (2022). R: A language and environment for statistical computing. R Foundation for Statistical Computing, Vienna, Austria. URL https://www.R-project.org/.

RAGHUKUMAR, C., & RAGHUKUMAR, S. (1998). Barotolerance of fungi isolated from deep-sea sediments of the Indian Ocean. Aquatic Microbial Ecology, 15(2), 153-163.

RAGHUKUMAR, C., RAGHUKUMAR, S., SHEELU, G., GUPTA, S. M., NATH, B. N., & RAO, B. R. (2004). Buried in time: culturable fungi in a deep-sea sediment core from the Chagos Trench, Indian Ocean. Deep Sea Research Part I: Oceanographic Research Papers, 51(11), 1759-1768.

RAPPLEYE, C. A., & GOLDMAN, W. E. (2006). Defining virulence genes in the dimorphic fungi. Annu. Rev. Microbiol., 60, 281-303.

REITNER, J., SCHUMANN, G., & PEDERSEN, K. (2006). Fungi in subterranean environments. Fungi in biogeochemical cycles, 24, 377.

RICHARDS, T. A., LEONARD, G., & WIDEMAN, J. G. (2017). What defines the "kingdom" fungi?. Microbiology spectrum, 5(3), 5-3.

RITZ, K. (2006). Fungal roles in transport processes in soils. Fungi in Biogeochemical Cycles. Cambridge University Press, Cambridge, 51-73.

SANTELLI, C. M., ORCUTT, B. N., BANNING, E., BACH, W., MOYER, C. L., SOGIN, M. L., STAUDIGEL, H. & EDWARDS, K. J. (2008). Abundance and diversity of microbial life in ocean crust. Nature, 453(7195), 653-656.

SASAKI, K., MATSUDA, M., HIRAJIMA, T., TAKANO, K., & KONNO, H. (2006). Immobilization of Mn (II) ions by a Mn-oxidizing fungus Paraconiothyrium sp.-like strain at neutral pHs. Materials transactions, 47(10), 2457-2461.

SCHMID-BEURMANN, H. A., KAHL, W. A., BACH, W., IVARSSON, M., BÖTTCHER, M. E., & PECKMANN, J. (2023). Dispersal of endolithic microorganisms in vesicular volcanic rock: Distribution, settlement and pathways revealed by 3D X-ray microscopy. Terra Nova.

SCHRENK, M. O., HUBER, J. A., & EDWARDS, K. J. (2010). Microbial provinces in the subseafloor. Annual review of marine science, 2, 279-304.

SCHUMANN, G., MANZ, W., REITNER, J., & LUSTRINO, M. (2004). Ancient fungal life in North Pacific Eocene oceanic crust. Geomicrobiology Journal, 21(4), 241-246.

SEKI, K., MIYAZAKI, T., NAKANO, M., (1998). Effects of microorganisms on hydraulic conductivity decrease in infiltration. European Journal of Soil Science, 49(2), 231-236.

SEKI, K., SUKO, T., & MIYAZAKI, T. (2002). Bioclogging of glass beads by bacteria and fungi. Trans. World Cong. Soil Sci, 1244-1.

SHIBATA, M., FUJITA, K., SUGIYAMA, J., TSUTA, M., KOKAWA, M., MORI, Y., & SAKABE, H. (2011). Predicting the buckwheat flour ratio for commercial dried buckwheat noodles based on the fluorescence fingerprint. Bioscience, biotechnology, and biochemistry, 75(7), 1312-1316.

SIDIKE, A., KUSACHI, I., & YAMASHITA, N. (2003). Natural fluorite emitting yellow fluorescence under UV light. Physics and chemistry of minerals, 30, 478-485.

SINGH, P., RAGHUKUMAR, C., VERMA, P., & SHOUCHE, Y. (2010). Phylogenetic diversity of culturable fungi from the deep-sea sediments of the Central Indian Basin and their growth characteristics. Fungal Diversity, 40, 89-102.

SMITS, M. (2006). Mineral tunnelling by fungi. Fungi in biogeochemical cycles, 24, 311.

SOHLBERG, E., BOMBERG, M., MIETTINEN, H., NYYSSÖNEN, M., SALAVIRTA, H., VIKMAN, M., & ITÄVAARA, M. (2015). Revealing the unexplored fungal communities in deep groundwater of crystalline bedrock fracture zones in Olkiluoto, Finland. Frontiers in microbiology, 573.

SPATAFORA, J. W., AIME, M. C., GRIGORIEV, I. V., MARTIN, F., STAJICH, J. E., & BLACKWELL, M. (2017). The fungal tree of life: from molecular systematics to genome-scale phylogenies. The fungal kingdom, 1-34.

STAUDIGEL, H., FURNES, H., MCLOUGHLIN, N., BANERJEE, N. R., CONNELL, L. B., & TEMPLETON, A. (2008). 3.5 billion years of glass bioalteration: Volcanic rocks as a basis for microbial life?. Earth-Science Reviews, 89(3-4), 156-176.

SUYAMUD, B., FERRIER, J., CSETENYI, L., INTHORN, D., & GADD, G. M. (2020). Biotransformation of struvite by Aspergillus niger: phosphate release and magnesium biomineralization as glushinskite. Environmental microbiology, 22(4), 1588-1602.

TANG, Y., ZEINER, C. A., SANTELLI, C. M., & HANSEL, C. M. (2013). Fungal oxidative dissolution of the Mn (II)-bearing mineral rhodochrosite and the role of metabolites in manganese oxide formation. Environmental microbiology, 15(4), 1063-1077.

TEMPLETON, A. S., & CARO, T. A. (2023). The Rock-Hosted Biosphere. Annual Review of Earth and Planetary Sciences, 51, 493-519.

TESKE, A., & SØRENSEN, K. B. (2008). Uncultured archaea in deep marine subsurface sediments: have we caught them all?. The ISME journal, 2(1), 3-18.

THORSETH, I. H., FURNES, H., & HELDAL, M. (1992). The importance of microbiological activity in the alteration of natural basaltic glass. Geochimica et Cosmochimica Acta, 56(2), 845-850.

THORSETH, I. H., TORSVIK, T., FURNES, H., & MUEHLENBACHS, K. (1995). Microbes play an important role in the alteration of oceanic crust. Chemical Geology, 126(2), 137-146.

THULLNER, M. (2010). Comparison of bioclogging effects in saturated porous media within one-and two-dimensional flow systems. Ecological Engineering, 36(2), 176-196.

TORSVIK, T., FURNES, H., MUEHLENBACHS, K., THORSETH, I. H., & TUMYR, O. (1998). Evidence for microbial activity at the glass-alteration interface in oceanic basalts. Earth and Planetary Science Letters, 162(1-4), 165-176.

TRIVITTAYASIL, V. (2016). EEM: read and preprocess fluorescence excitation-emission matrix (EEM) data, R package version 1.1.1.9000, https://github.com/chengvt/EEM.

TRIVITTAYASIL, V., KAMEYA, H., SHOJI, T., TSUTA, M., KOKAWA, M., & SUGIYAMA, J. (2017). Simultaneous estimation of scavenging capacities of peach extract for multiple reactive oxygen species by fluorescence fingerprint method. Food chemistry, 232, 523-530.

TULLY, B. J., WHEAT, C. G., GLAZER, B. T., & HUBER, J. A. (2018). A dynamic microbial community with high functional redundancy inhabits the cold, oxic subseafloor aquifer. The ISME journal, 12(1), 1-16.

VARGAS-GASTÉLUM, L., & RIQUELME, M. (2020). The mycobiota of the deep sea: What omics can offer. Life, 10(11), 292.

VARGAS-GASTÉLUM, L., CHONG-ROBLES, J., LAGO-LESTÓN, A., DARCY, J. L., AMEND, A. S., & RIQUELME, M. (2019). Targeted ITS1 sequencing unravels the mycodiversity of deep-sea sediments from the Gulf of Mexico. Environmental microbiology, 21(11), 4046-4061.

WEETE, J. D., ABRIL, M., & BLACKWELL, M. (2010). Phylogenetic distribution of fungal sterols. PloS one, 5(5), e10899.

WHELAN, J. K., OREMLAND, R., TARAFA, M., SMITH, R., HOWARTH, R., LEE, C., (1986). Evidence for sulfate-reducing and methaneproducing micro-organisms in sediments from Site 618, Site 619, and Site 622. Initial Reports of the Deep Sea Drilling Project, 96, 767–775.

WHITMAN, W. B., COLEMAN, D. C., & WIEBE, W. J. (1998). Prokaryotes: the unseen majority. Proceedings of the National Academy of Sciences, 95(12), 6578-6583.

WICKHAM, H. (2016). ggplot2: Elegant Graphics for Data Analysis. Springer-Verlag New York. R package version 3.4.4. < https://ggplot2.tidyverse.org>.

WIRTH, F., & GOLDANI, L. Z. (2012). Epidemiology of Rhodotorula: an emerging pathogen. Interdisciplinary perspectives on infectious diseases, 2012.

WRIGHT, A. L., WANG, Y., & REDDY, K. R. (2008). Loss-on-ignition method to assess soil organic carbon in calcareous everglades wetlands. Communications in soil science and plant analysis, 39(19-20), 3074-3083.

YOSHIDA, N., HIGASHIMURA, E., & SAEKI, Y. (2010). Catalytic biomineralization of fluorescent calcite by the thermophilic bacterium Geobacillus thermoglucosidasius. Applied and environmental microbiology, 76(21), 7322-7327.

ZHONG, X., & WU, Y. (2013). Bioclogging in porous media under continuous-flow condition. Environmental earth sciences, 68, 2417-2425.

ZHONG, X., WU, Y., & XU, Z. (2013). Bioclogging in porous media under discontinuous flow condition. Water, Air, & Soil Pollution, 224, 1-12.

Appendix

Appendix 1 R code chunk for processing of the EEM data frame

```
##Processing the data
#remove EM and EX ranges that negatively effect data analysis
eem_model_data_cut <- delScattering2(eem_model_data, NA)
#unfold
unfolded_model_data_cut <- unfold(eem_model_data_cut)
#normalize the data
model_data_norm <- normalize(unfolded_model_data_cut)
#mean-center the data
model_col_means <- colMeans(model_data_norm)
mean_center <- function(x, means_data) {
  x - rep(means_data, rep.int(nrow(x), ncol(x)))
}

model_data_final <- mean_center(model_data_norm, model_col_means)
```

Appendix 2 R code chunk to create the validation and calibration data frames to subsequently perform PLS

```
##Validation and Calibration df
# Set the seed for reproducibility
set.seed(123)

# Get the total number of observations
n <- nrow(biomass)

# Generate a random sequence of indices
```

```
indices <- sample(1:n)

# Determine the size of the calibration set to 80% of the data
cal_size <- round(0.8 * n)

# Create the calibration set
biomass.calpsl <- biomass[indices[1:cal_size], ]
EEM.calpsl <- model_data_final[indices[1:cal_size], ]

# Create the validation set
biomass.valpsl <- biomass[indices[(cal_size+1):n], ]
EEM.valpsl <- model_data_final[indices[(cal_size+1):n], ]

#put it together to a dataframe

calpls <- data.frame(df = I(EEM.calpsl), biomass.calpsl)
valpls <- data.frame(df = I(EEM.valpsl), biomass.valpsl)
```

```
##Perform PLS
model <- pls::plsr(weight ~ df, data = calpls, ncomp = 4, validation = "
CV",
                   method = "oscorespls")
validationplot(model, val.type = "MSEP", intercept = TRUE, legend = TRUE
)
```

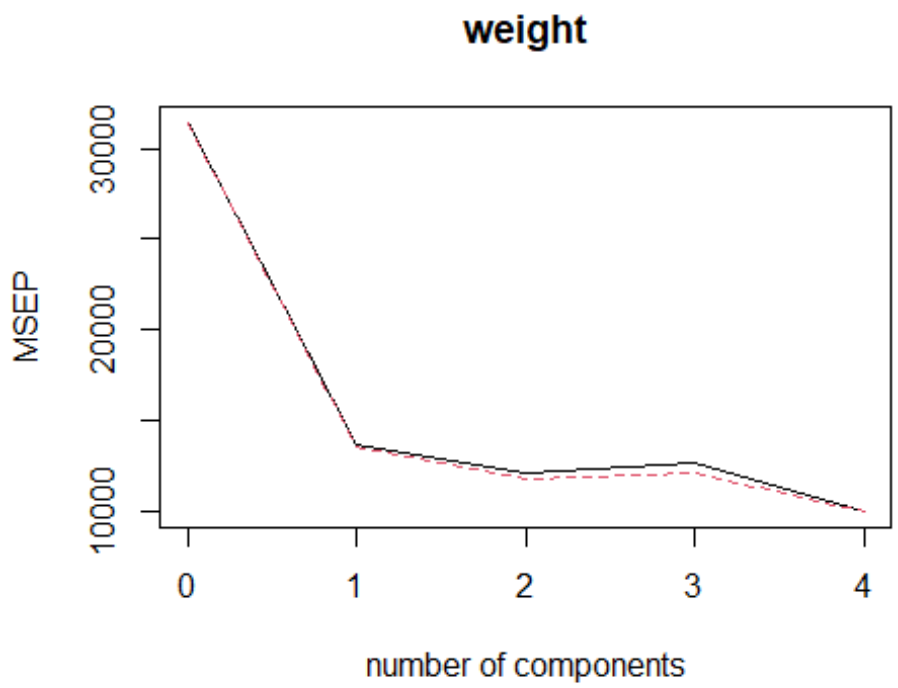


```
ncomp <- 2
model <- pls::plsr(weight ~ df, data = calpls, ncomp = ncomp, method = "
oscorespls")
```

Appendix 3 R code chunk to choose the variables with the VIP cutoff value to create the optimal model

```
#get the VIP values
vip_val <- VIP(model)

#reshape data into the long format
vip_data_transposed <- t(vip_val)
# Create a long format dataframe
vip_data_long <- as.data.frame(vip_data_transposed)
vip_data_long$Variable <- rownames(vip_data_long)
vip_data_long <- tidyr::gather(vip_data_long, key = "Component", value =
"VIP", -Variable)
```

```
## Finding the best cut-off value
#empty data frame for the results of the loop
stat_df <- data.frame()

#creating a vector with the vip values to be tested as cut-off values
lowest_value <- min(vip_data_long$VIP)
highest_value<- max(vip_data_long$VIP-0.01)
cutoff_values <- seq(lowest_value, highest_value, by = 0.01)

# Define the number of folds for cross-validation
num_folds <- 10

#make a loop to test all cutoff values and calculate the statistics for
the models

for (cutoff in cutoff_values) {

   #identify variables with VIP values higher than cutoff
  selected_vip <- vip_data_long[vip_data_long$VIP > cutoff, ]
  selected_variables <- selected_vip$Variable

  # If no variables selected, skip this iteration
  if (length(selected_variables) == 0)
    next

  # Create a new dataframe with selected variables
  EEM_select_cal <- EEM.calpsl[ , selected_variables]
  EEM_select_val <- EEM.valpsl[ , selected_variables]

  cal_select <- data.frame(df = I(EEM_select_cal), biomass.calpsl)
  val_select <- data.frame(df = I(EEM_select_val), biomass.valpsl)

  #define the maximum amount of components to use in the first model
  #make a vector with the amount of the selected variables and the amoun
t of observations -1
  #(max amount of components is amount of variables, folds of cross vali
dation or the amount of observation -1)
  comp_choose <- c(length(selected_variables), (length(biomass.calpsl$we
```

```
ight)-1), num_folds)
  ncomp_try <- min(comp_choose)

  # If there is no model possible, skip the iteration
  if (ncomp_try == 0)
    next

  # Determine optimal number of components for PLS model
  model_ncomp <- pls::plsr(weight ~ df, data = cal_select, ncomp = ncomp
_try, validation = "CV",
                           folds = num_folds, method = "oscorespls")
  ncomp_opt <- selectNcomp(model_ncomp, 'onesigma', plot = FALSE)

  # If there is no model possible, skip the iteration
  if (ncomp_opt == 0)
    next

  # Fit PLS model with selected variables and optimal number of componen
ts
  opt_model <- pls::plsr(weight ~ df, data = cal_select, ncomp = ncomp_o
pt, validation = "CV",
                       method = "oscorespls")


  # Calculate statistics
  R2CV <- pls::R2(opt_model, valtype = "CV")$val[,,ncomp_opt + 1]
  RMSECV <- sqrt(pls::RMSEP(opt_model, valtype = "CV")$val[,,ncomp_opt +
1])
  residuals_cv <- residuals(opt_model, type = "calibration")
  response <- biomass.calpsl$weight
  RPDCV <- sd(response) / sd(residuals_cv)
  R2P <- pls::R2(opt_model, newdata = val_select, valtype = "test")$val[
,,ncomp_opt + 1]
  RMSEP <- sqrt(pls::RMSEP(opt_model, newdata = val_select)$val[,,ncomp_
opt + 1])
  residuals_test <- residuals(opt_model, newdata = val_select, type = "r
esponse")
  response_test <- biomass.valpsl$weight
  RPDp <- sd(response_test) / sd(residuals_test)

  # Store results in data frame
  result <- data.frame(
    VIP_Cutoff = cutoff,
    n_comp = ncomp_opt,
    R2CV = R2CV,
    RMSECV = RMSECV,
    RPDCV = RPDCV,
    R2P = R2P,
    RMSEP = RMSEP,
    RPDp = RPDp
  )

    stat_df <- rbind(stat_df, result)
}
```

```
## Filter for the optimal cut-off value
#first delete all rows starting with the row name 'adj'
stat_df <- stat_df[!startsWith(rownames(stat_df), 'adj'),]

#find the row that is overall the best

# Select columns for weight calculation (only statistics columns)
stats_columns <- stat_df[, c("R2CV", "RMSECV", "RPDCV", "R2P", "RMSEP",
"RPDp")]

# Define weights for each statistic
weights <- c(1, -1, 1, 1, -1, 1)

#normalize the data
normalize_stat <- function(x) {
  (x-min(x))/(max(x) - min(x))
}
normalized_stat_df <- as.data.frame(lapply(stats_columns, normalize_stat
))

# Calculate weighted sum for each row
weighted_sum <- rowSums(normalized_stat_df * weights)

#add weighted sums to the original df
stat_df$WeightedSum <- weighted_sum

# Find row with the highest weighted sum
best_overall_row <- stat_df[which.max(weighted_sum), ]


#find the best rows for each individual statistic

# Find row with the highest R2CV
best_R2CV_row <- stat_df[which.max(stat_df$R2CV), ]

# Find row with the lowest RMSECV
best_RMSECV_row <- stat_df[which.min(stat_df$RMSECV), ]

# Find row with the highest RPDCV
best_RPDCV_row <- stat_df[which.max(stat_df$RPDCV), ]

# Find row with the highest R2P
best_R2P_row <- stat_df[which.max(stat_df$R2P), ]

# Find row with the lowest RMSEP
best_RMSEP_row <- stat_df[which.min(stat_df$RMSEP), ]

# Find row with the highest RPDp
best_RPDp_row <- stat_df[which.max(stat_df$RPDp), ]
```

```
# Combine all best rows into a new data frame
best_stats_df <- rbind(best_R2CV_row, best_RMSECV_row, best_RPDCV_row,
                       best_R2P_row, best_RMSEP_row, best_RPDp_row, best
_overall_row)
best_stats_df$Statistic_evaluated <- c("R2CV", "RMSECV", "RPDCV", "R2P",
"RMSEP", "RPDp", "all")


vip_cutoff_value <- best_stats_df[7, 'VIP_Cutoff']
ncomp_opt <- best_stats_df[7, 'n_comp']

# Select variables with VIP > cutoff value
if ('Comp 1' %in% rownames(vip_val)) {
  # Use logical indexing to get column names where the condition is met
in a specific row
  selected_variables <- colnames(vip_val)[vip_val['Comp 1', ] > vip_cuto
ff_value ]

  # Check if any columns meet the condition
  if (length(selected_variables) > 0) {
    # Print the result
    print(selected_variables)
  } else {
    cat("No columns meet the condition for row", target_row, "\n")
  }
} else {
  cat("Row", 'Comp 1', "does not exist in the matrix\n")
}
```

Appendix 4 Heat map of the variables used in the biomass estimation models based on the growth media. The colours indicate in how many models the respective excitation and emission wavelength pairs were used. Wavelengths are given in nm.

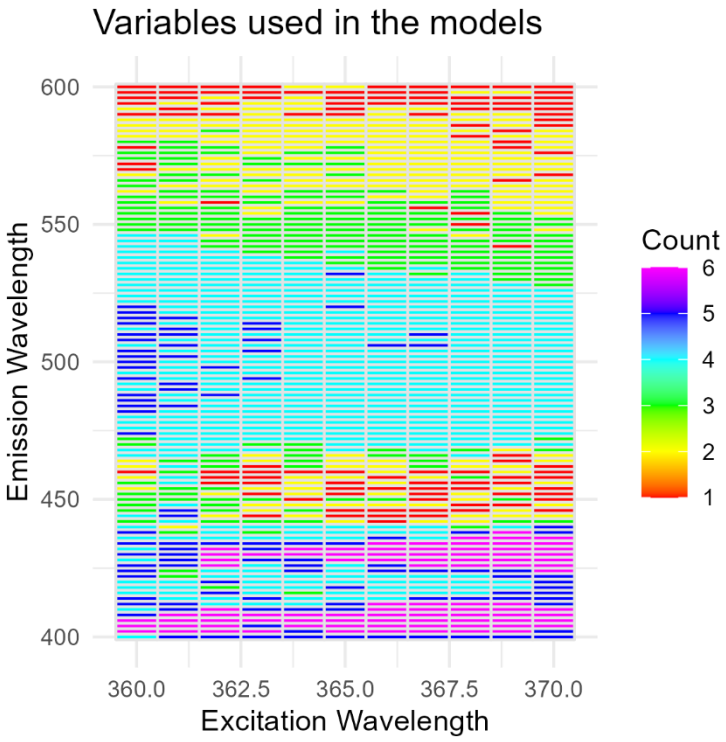

Appendix 5 Plots of calibration and validation data sets showing the measured fungal biomass against the estimated biomass in µg using the model and the optimized model for the 10 % lennox broth in artificial seawater.

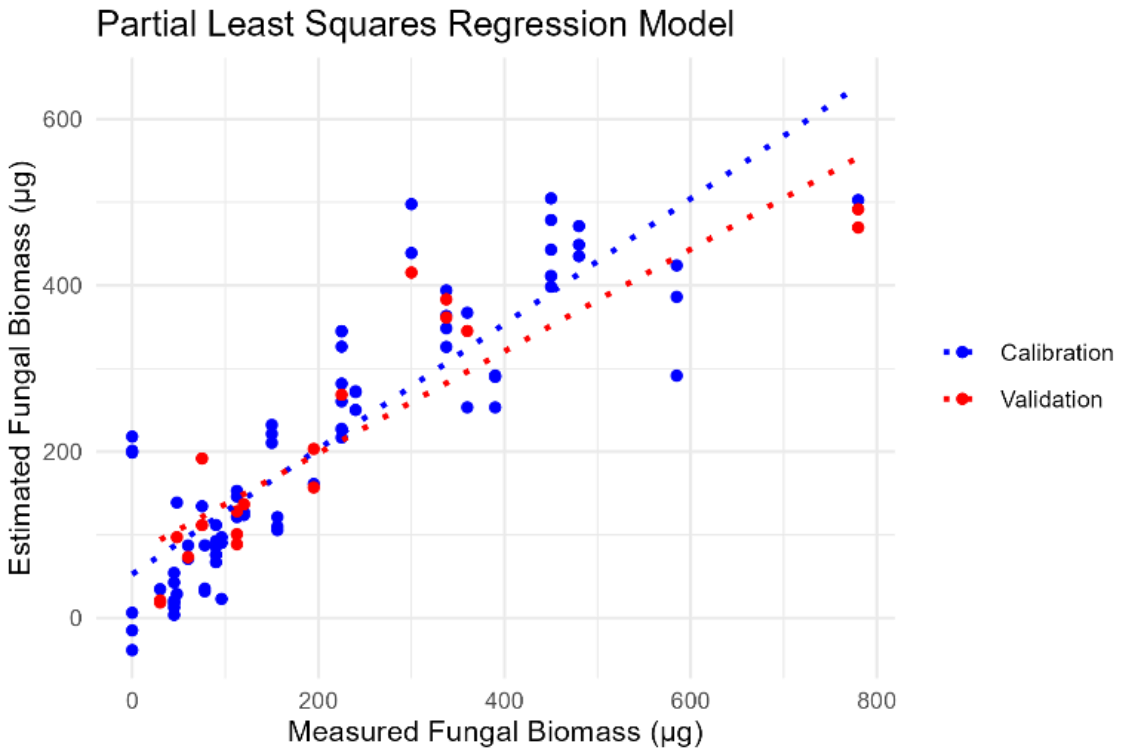

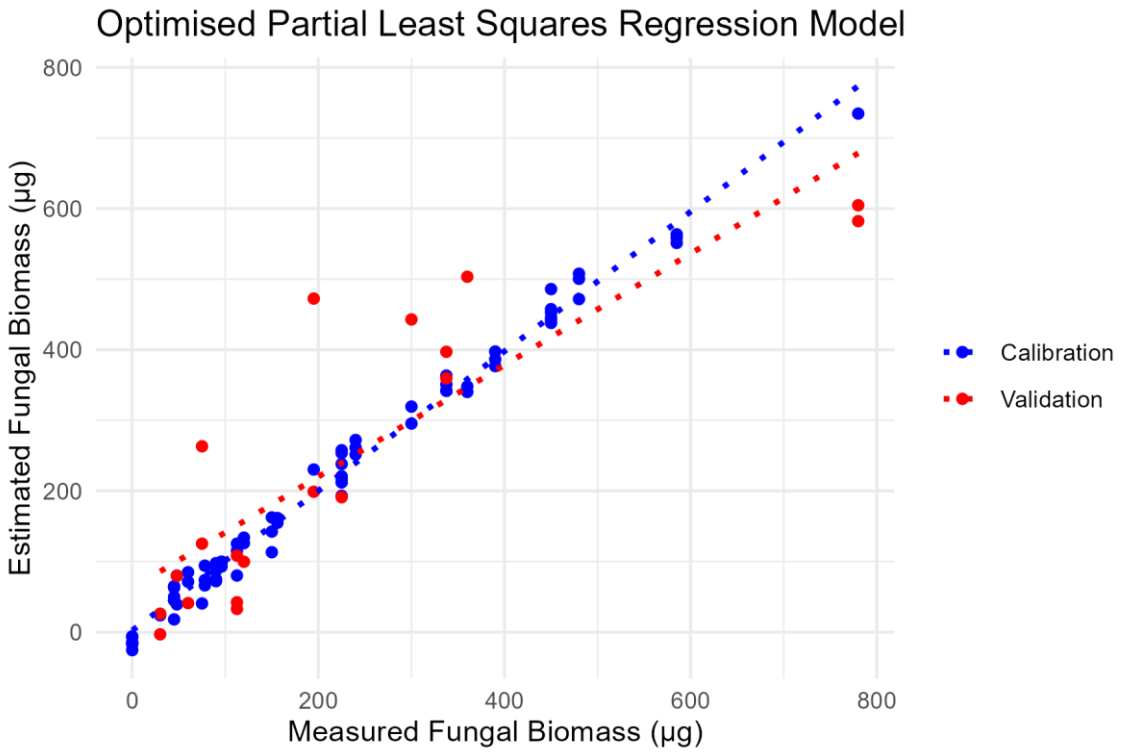

Appendix 6 Table of most measured blanks and their estimated biomasses using the model based on 10 % LB in ASW and 10 % LB. Sample ID: BS -> blank sample (extraction procedure conducted), Eth -> pure ethanol, LB/PG -> Growth media of the model measurement, 1/10 -> growth media percent of the measurement, H/G + number -> well in which it was measured. The last six measurements were pure ethanol and measured together with the experiment samples.

Sample ID	10% LB in ASW Weight (µg)	10 % LB Weight (µg)
BS_LB10..H07	292.7760101	159.1593412
BS_LB10..H08	316.003825	104.3389906
BS_LB10..H09	369.3130541	163.5684139
Eth_LB10..H10	210.6809589	-72.83698043
Eth_LB10..H11	213.8303511	-78.59881916
Eth_LB10..H12	201.3276787	-55.46269121
BS_LB1..H07	570.2394004	470.5214771
BS_LB1..H08	584.215959	467.1570189
BS_LB1..H09	582.2721571	461.6403187
Eth_LB1..H10	511.3972967	396.9106005
Eth_LB1..H11	451.2721677	377.6469331
Eth_LB1..H12	460.0507399	368.3707759
BS_LBinASW..H07	-17.15558875	-83.57869868
BS_LBinASW..H08	-14.48509955	-54.03847361
BS_LBinASW..H09	-25.49240411	-104.5536776
Eth_LBinASW..H10	-5.98577061	-476.8952529
Eth_LBinASW..H11	-15.36859487	-436.4018466
Eth_LBinASW..H12	-6.905644168	-422.9886354
BS_PG10..H07	85.8992142	-59.30941103
BS_PG10..H08	156.2900324	-61.85278842
BS_PG10..H09	185.1029544	-71.5220251
Eth_PG10..H10	53.07862948	-302.5537443
Eth_PG10..H11	-12.79968688	-293.0178386
Eth_PG10..H12	-37.66156311	-294.0373168
BS_PG1..H07	453.3636024	387.2223938
BS_PG1..H08	437.7597788	387.8927966
BS_PG1..H09	460.555443	392.3820076
Eth_PG1..H10	379.6497133	297.9999413
Eth_PG1..H11	417.9590239	278.3750246
Eth_PG1..H12	391.8753115	282.5785752

Eth_PG_100_1..H01	230.3396361	-140.1292781
Eth_PG_100_1..H02	192.2940717	-126.9404491
Eth_PG_100_1..H03	103.8789893	-115.7577815
Eth_PG_100_2..G10	74.03214296	-535.8759281
Eth_PG_100_2..G11	72.62855863	-559.3389438
Eth_PG_100_2..G12	123.0014485	-481.402633
Eth_H04	185.4142413	-557.4456349
Eth_H05	154.6652112	-521.4072762
Eth_H06	167.6170642	-544.2794286
Eth_H07	116.2539301	-546.0570963
Eth_H08	78.30509694	-540.6769714
Eth_H09	89.27690566	-565.1373972